Remodeling Characteristics and *in vivo* Healing of Low Viscosity Polyurethane Biocomposites for Bone Regeneration

By

Anne Douglas Talley

Dissertation
Submitted to the Faculty of the
Graduate School of Vanderbilt University
in partial fulfillment of the requirements
for the degree of

DOCTOR OF PHILOSOPHY
in

Chemical Engineering
May, 2016
Nashville, Tennessee

Approved:

Scott A. Guelcher, Ph.D.

Matthew J. Lang, Ph.D.

M. Douglas LeVan, Ph.D.

Julie A. Sterling, Ph.D.

To all of my family and friends who supported me on this journey.

To my husband Trent, I would not have gotten to this point without you.

To my son Elliot, your smile lights up our lives.

ACKNOWLEDGEMENTS

The research presented herein is the culmination of approximately 5 years of work that would not have been possible within the help and support I have received from a variety of sources. My advisor, Scott Guelcher, played a pivotal role in my time in graduate school, and I am eternally grateful for his expertise, guidance, and excitement about our projects. Additionally, I am thankful for the support from my committee members Matthew Lang, M. Douglas LeVan, and Julie Sterling. Their unique viewpoints helped to focus my research goals and provided interesting perspectives that we had not previously considered. I am grateful for the funding sources that supported my time in the lab, including the Armed Forces Institute of Regenerative Medicine (I and II), the National Science Foundation, the National Institutes of Health, and the Department of Education Graduate Assistance in Areas of National Need (GAANN) fellowship program.

I would like to thank all of the members of the Guelcher lab, past and present, who helped me learn important techniques, find solutions to problems, and provided guidance during good times and bad. Margarita Prieto-Ballangee was pivotal in my introduction to the lab, and without her my first few years would not have been productive. A special thanks to our fantastic lab manager, Kasia Zienkiewicz whose knowledge about chemistry is unparalleled and without whom the lab would not run nearly as smoothly. Drew Harmata, Ruijing Guo, Jon Page, Elizabeth Adolph, Ushashi Dadwal, Sichang Lu, Maddi McEnery, Joe Vanderburg, and Tommy Spoonmore all made my time in the lab much more enjoyable. I would also like to acknowledge the help of undergraduate students Nicholas Gould, Kyle Musto, and Mollie Maples and high school student Lillian Ekem whose contributions to the research projects were invaluable. Additionally, the office would not have been nearly as fun or enjoyable without the presence of the Young lab members, particularly Lara Jazmin and Ali McAtee.

Thank you to the chemical engineering staff Mary Gilleran, Rae Uson, Mark Holmes, and Julie James for all of the help during my tenure. I am grateful to Alyssa Merkel and the other members of the Sterling lab for helping me learn microbiology techniques when my skills were entirely novice. Sasi Uppuganti provided significant support and expertise in the biomechanics lab at Vanderbilt. I would like to thank Dan Perrien (Vanderbilt University Institute of Imaging Science), Carol Ann Bonner (Cell Imaging Shared Resource), and Jeff Nyman (Vanderbilt Biomechanics Lab) for providing training and instrumentation. Thank you to our collaborators outside of Vanderbilt, particularly Dr. Pam Brown-Bear and Dr. Josh Wenke at the Armed Forces Institute of Regenerative Medicine whose insights were invaluable in planning and running experiments.

Finally, I would not be here my family and friends. I would like to express gratitude to my husband Trent, who supported me throughout my graduate school career and uprooted his life to follow me to Nashville so that I could fulfill my own goals. I could not ask for a more wonderful partner or friend. I am forever thankful for our son Elliot and the support from Vanderbilt during my maternity leave. I am immensely grateful for all of our Nashville friends we met along the journey. It was a pleasure finding a group of friends with whom we could play nerdy board games and watch sporting events.

TABLE OF CONTENTS

APPENDIX

LIST OF TABLES

Table Page

LIST OF FIGURES

CHAPTER 1

INTRODUCTION

Tissue engineering encompasses the study of the life sciences and engineering to discover fundamental differences between healthy and diseased tissue and develop new methods and materials to treat diseased and deficient tissues/organ systems (1). Tissue engineers aim to induce fully functional skin, bone, cartilage, capillary, and periodontal tissues in patients with clinical needs due to trauma, cancer, disease, or congenital defects (2). In bone tissue engineering, researchers use novel biomaterials, often in combination with cells or signaling growth factors, to restore, maintain, or enhance natural bone (3).

It is estimated that more than 1.5 million bone grafting procedures are performed in the United States each year (4). Bone grafting can be used to treat patients suffering from injuries, tumors, infection, and degenerative disease (5). The applications for bone grafts are expansive, with the majority of procedures related to spinal fusions (6, 7), orthopaedic defects (8, 9), and craniomaxillofacial defects (10). According to the World Health Organization, direct and indirect costs associated with musculoskeletal conditions in the United States reached $215 billion in 1995 (11). As the population ages the number of bone graft operations is anticipated to rise, with an expected doubling of patients over 50 experiencing bone disease by 2020 (12, 13). There is considerable interest in using tissue engineering approaches to develop new, more economical biomaterials for bone grafting and to help standardize the success of such procedures.

A number of treatment options are available in bone grafting with autograft bone, taken from a separate site in the same patient, considered the clinical gold standard. However, autograft use is constrained by limited availability in the iliac crest and the potential for chronic pain and donor site morbidity (14). There are a variety of biodegradable, synthetic alternatives to autograft that include polymers, ceramics, bioactive glasses, and composites (15). The aim of this dissertation is to develop and characterize low viscosity (LV) polyurethane (PUR) biocomposites for bone regeneration and to test growth factor release and remodeling characteristics of the LV grafts *in vitro* and *in vivo*.

Chapter II examines the previous literature in the field of tissue engineering and bone regeneration. The work discussed herein applies materials science and biological fundamentals to help solve clinically relevant medical conditions. A thorough review of the currently accepted practices and understanding in the field of biomaterials and tissue regeneration is necessary prior to discussion of specific research topics.

Researchers in the field of tissue engineering are currently developing new bone grafts that match the chemical, mechanical, and physical properties of natural bone (13). Ceramics are often used in bone regeneration due to their osteogenic nature, however they can be brittle and fail quickly under tension limiting their direct use (16). Composites of polymers and ceramics are frequently studied as these combine the ductile nature but poor strength of polymers with the osteogenic but low fracture toughness of ceramics (17). **Chapter III** discusses the testing of a LV/ceramic biocomposite in a sheep femoral plug model against a clinically available ceramic control.

RhBMP-2 is an osteoinductive growth factor widely used in clinical bone repair (18). RhBMP-2 is FDA approved for some craniomaxillofacial and spinal bone treatments when delivered via an acellular collagen sponge (ACS). RhBMP-2 must be locally delivered at the desired site, and the specific release kinetics affect cellular ingrowth and bone healing (19). To ascertain the effect of growth factor delivery from delivery systems of interest, it is necessary to thoroughly characterize the rhBMP-2 release kinetics from biocomposite delivery systems of interest (20). **Chapter IV** describes the release kinetics of rhBMP-2 delivered from an LV graft tested both *in vivo* and *in vitro*.

There are a variety of animal models used to test bone grafts. The canine saddle defect model is commonly used to test bone grafts intended for craniomaxillofacial applications, as the anatomy of the canine mandible is similar to that of humans and healing progression is comparable (21). Defect space maintenance poses a problem in the mandible due to the forces applied by soft tissue. To maintain the space through healing, most grafts require the use of guided bone regeneration (GBR).These techniques use a polymer or metal external fixation device to preserve the defect volume (22). However, GBR has been associated with complications including seroma, infection, or wound failure (23, 24). **Chapter V** investigates the use of a compression resistant LV graft, which eliminates the need for external fixation, augmented with rhBMP-2 in a canine saddle defect model.

While autograft and allograft remodel in a similar manner to natural bone, the degradation properties of many ceramics and bioactive glasses is not fully understood. A number of intrinsic and extrinsic factors contribute to remodeling making it more difficult to study *in vitro*, including graft porosity, chemical composition, implantation site, and biological signaling molecules (25, 26). A number of groups have studied osteoclast resorption using growth factors to drive differentiation since the 1990s when the Suda research group determined that receptor activator of nuclear factor κβ ligand (RANKL) is responsible for producing active osteoclasts (27). These methods, however, rely on expensive growth factors and the harvest of primary cells. Additionally, there is no accepted method for the quantification of osteoclast pitting on surfaces. **Chapter VI** describes the development of an *in vitro* assay based on established cell lines to quantify osteoclast resorption of synthetic matrices using optical profilometry.

Spinal fusion procedures are widely performed in the United States to treat patients suffering from degenerative conditions. Previous research has suggested that hospital stays and muscle destruction associated with posteolateral fusions could potentially be decreased with the use of minimally invasive surgical (MIS) techniques; however, no clinical studies have compared the outcomes of conventional and MIS approaches (28). Additionally, posterolateral spinal fusions are challenged by limited bony surfaces and compressive forces of the posterior musculature (29). **Chapter VII** describes an injectable, compression-resistant LV graft that promotes union in a single level posterolateral rabbit spinal fusion model. The LV graft is a potential candidate for use with MIS techniques for posterolateral fusion.

In conclusion, **Chapter VIII** summarizes the findings presented in this work and lists recommendations for future studies. Broadly, the work presented here informs the reader about the current treatment options in bone grafting and presents studies demonstrating the potential of polyurethane biocomposites in a clinical setting.

<u>References</u>

1. Hubbell, J.A. Biomaterials in Tissue Engineering. Nat Biotech **13**, 565, 1995.
2. Ikada, Y. Challenges in tissue engineering. Journal of the Royal Society Interface **3**, 589, 2006.
3. Salgado, A.J., Coutinho, O.P., andReis, R.L. Bone Tissue Engineering: State of the Art and Future Trends. Macromolecular Bioscience **4**, 743, 2004.
4. Bishop, G.B., andEinhorn, T.A. Current and future clinical applications of bone morphogenetic proteins in orthopaedic trauma surgery. International Orthopaedics **31**, 721, 2007.
5. O'Keefe, R.J., andMao, J. Bone tissue engineering and regeneration: from discovery to the clinic—an overview. Tissue Engineering Part B: Reviews **17**, 389, 2011.
6. Rajaee, S.S., Bae, H.W., Kanim, L.E.A., andDelamarter, R.B. Spinal Fusion in the United States: Analysis of Trends From 1998 to 2008. Spine **37**, 67, 2012.
7. Wojewnik, B., andBoden, S.D. Current Concepts in Bone Grafting for Spine Fusion. Contemporary Spine Surgery **15**, 1, 2014.
8. Pape, H.C., Evans, A., andKobbe, P. Autologous bone graft: properties and techniques. Journal of orthopaedic trauma **24**, S36, 2010.
9. Calori, G.M., Mazza, E., Colombo, M., andRipamonti, C. The use of bone-graft substitutes in large bone defects: any specific needs? Injury **42 Suppl 2**, S56, 2011.
10. Bhumiratana, S., andVunjak-Novakovic, G. Concise review: personalized human bone grafts for reconstructing head and face. Stem cells translational medicine **1**, 64, 2012.
11. Lauzon, M.A., Bergeron, E., Marcos, B., andFaucheux, N. Bone repair: new developments in growth factor delivery systems and their mathematical modeling. J Control Release **162**, 502, 2012.
12. Brydone, A.S., Meek, D., andMaclaine, S. Bone grafting, orthopaedic biomaterials, and the clinical need for bone engineering. Proceedings of the Institution of Mechanical Engineers, Part H: Journal of Engineering in Medicine **224**, 1329, 2010.
13. Navarro, M., Michiardi, A., Castaño, O., andPlanell, J.A. Biomaterials in orthopaedics. Journal of The Royal Society Interface **5**, 1137, 2008.
14. Khan, Y., Yaszemski, M.J., Mikos, A.G., andLaurencin, C.T. Tissue Engineering of Bone: Material and Matrix Considerations. The Journal of Bone & Joint Surgery **90**, 36, 2008.
15. Giannoudis, P.V., Dinopoulos, H., andTsiridis, E. Bone substitutes: An update. Injury **36**, S20, 2005.
16. Finkemeier, C.G. Bone-grafting and bone-graft substitutes. The Journal of Bone & Joint Surgery **84**, 454, 2002.
17. Neuendorf, R.E., Saiz, E., Tomsia, A.P., andRitchie, R.O. Adhesion between biodegradable polymers and hydroxyapatite: Relevance to synthetic bone-like materials and tissue engineering scaffolds. Acta Biomaterialia **4**, 1288, 2008.
18. Lo, K.W.-H., Ulery, B.D., Ashe, K.M., andLaurencin, C.T. Studies of bone morphogenetic protein-based surgical repair. Advanced drug delivery reviews **64**, 1277, 2012.
19. Haidar, Z., Hamdy, R., andTabrizian, M. Delivery of recombinant bone morphogenetic proteins for bone regeneration and repair. Part A: Current challenges in BMP delivery. Biotechnology Letters **31**, 1817, 2009.
20. Boerckel, J.D., Kolambkar, Y.M., Dupont, K.M., Uhrig, B.A., Phelps, E.A., Stevens, H.Y., Garcia, A.J., andGuldberg, R.E. Effects of protein dose and delivery system on BMP-mediated bone regeneration. Biomaterials **32**, 5241, 2011.

21. Jovanovic, S.A., Hunt, D.R., Bernard, G.W., Spiekermann, H., Wozney, J.M., andWikesjo, U.M. Bone reconstruction following implantation of rhBMP-2 and guided bone regeneration in canine alveolar ridge defects. Clin Oral Implants Res **18**, 224, 2007.
22. Schwarz, F., Mihatovic, I., Golubovic, V., Hegewald, A., andBecker, J. Influence of two barrier membranes on staged guided bone regeneration and osseointegration of titanium implants in dogs: part 1. Augmentation using bone graft substitutes and autogenous bone. Clin Oral Implants Res **23**, 83, 2012.
23. Schliephake, H., Drewes, M., Mihatovic, I., Schwarz, F., Becker, J., andIglhaut, G. Use of a self-curing resorbable polymer in vertical ridge augmentations - a pilot study in dogs. Clin Oral Implants Res **25**, 435, 2014.
24. dal Polo, M.R., Poli, P.P., Rancitelli, D., Beretta, M., andMaiorana, C. Alveolar ridge reconstruction with titanium meshes: A systematic review of the literature. Medicina oral, patologia oral y cirugia bucal **19**, e639, 2014.
25. Barrère, F., van Blitterswijk, C.A., andde Groot, K. Bone regeneration: molecular and cellular interactions with calcium phosphate ceramics. International Journal of Nanomedicine **1**, 317, 2006.
26. Larsson, S., andHannink, G. Injectable bone-graft substitutes: Current products, their characteristics and indications, and new developments. Injury **42, Supplement 2**, S30, 2011.
27. Udagawa, N., Takahashi, N., Jimi, E., Matsuzaki, K., Tsurukai, T., Itoh, K., Nakagawa, N., Yasuda, H., Goto, M., Tsuda, E., Higashio, K., Gillespie, M.T., Martin, T.J., andSuda, T. Osteoblasts/stromal cells stimulate osteoclast activation through expression of osteoclast differentiation factor/RANKL but not macrophage colony-stimulating factor. Bone **25**, 517, 1999.
28. Skovrlj, B., Gilligan, J., Cutler, H.S., andQureshi, S.A. Minimally invasive procedures on the lumbar spine. World Journal of Clinical Cases : WJCC **3**, 1, 2015.
29. Glassman, S.D., Dimar, J.R., Carreon, L.Y., Campbell, M.J., Puno, R.M., andJohnson, J.R. Initial fusion rates with recombinant human bone morphogenetic protein-2/compression resistant matrix and a hydroxyapatite and tricalcium phosphate/collagen carrier in posterolateral spinal fusion. Spine **30**, 1694, 2005.

CHAPTER II

BACKGROUND

Bone tissue engineering

Tissue engineering focuses on restoring, maintaining, or enhancing tissues and organs. One of the original landmark developments in the field occurred in 1907 with the first established cell culture line, from frog ectodermal cells, grown *in vitro* by Ross Harrison at Johns Hopkins Medical School (1). More recently, in 2002 89 firms in 15 countries were engaged in tissue engineering research spending $487 million per year (2). While tissue engineering includes research on a variety of tissue types, bone engineering in particular involves the use of a biomaterial scaffold that supports new bone growth often with the addition of osteoblastic cells that deposit new tissue and/or signaling molecules that promote cell recruitment and differentiation (3).

Under normal conditions bone undergoes a dynamic process of remodeling where bone is constantly resorbed by osteoclasts while osteoblasts deposit new tissue. Small defects and fractures are also repaired through this process. Spontaneous repair is not possible; however, in cases of large critical-size defects or underlying pathological state (disease, infection, etc) (4). Bone defects can be challenging for orthopaedic and craniomaxillofacial surgeons, particularly in circumstances of fracture non-union or post injury complications (5). The clinical gold standard for many bone defects is autograft, harvested from a secondary site in the patient, which has the ideal graft properties of osteogenicity (contains cells), osteoinductivity (contains signaling molecules that drive cellular differentiation), and osteoconductivity (supports cell attachment and growth) (6). However, there is a limited supply of autograft available in the iliac crest and harvest can lead to donor site morbidity and chronic pain (7). A number of tissue engineering strategies have been applied to bone regeneration research to develop alternative treatment options to autologous bone for bone defects created through injury or disease. The variety of potential biomaterials in tissue engineering allows researchers to tailor their approach to the specific clinical need, whether that be mechanical integrity, a delivery system for proteins or small molecule drugs, or minimally invasive surgical delivery (8). It is desirable that these biomaterials are easy to handle and deliver and are biocompatible.

Autograft alternatives

Allograft bone, from cadaver tissue, has the same mineral composition as natural bone and can serve as an osteoconductive matrix for new bone formation in defects. However, incompatible transplanted tissue can elicit an immune response in the patient. Allograft also carries a small but finite risk of disease transmission with grafting, although measures are taken to sterilize tissue. Additionally, availability can be limited depending on cadaver tissue bank supply (9). Moreover, the combination of allograft and growth factors has been shown to lead to transient resorption and poor healing (10, 11). Currently studied allograft alternatives include polymers, ceramics, and bioactive glasses (12).

Natural polymers such as collagen, chitin, alginate, and gelatin are widely used in the field of tissue engineering with the advantages of being biodegradable and having a low likelihood of toxicity (13). Protein based polymers can mimic many of the physical properties of the extracellular matrix allowing cells to migrate and organize similarly to responses in host tissue (14). However, natural polymers can be limited in use in bone engineering due to batch to batch variability in processing (15) and low mechanical integrity (16). Additionally, the *in vivo* degradation of natural polymers can depend significantly on the types and concentrations of enzymes present at the defect site creating difficulty in measuring or predicting polymer degradation (17).

The key advantages of synthetic polymers are the tunable mechanical properties and degradation kinetics based on tailorable chemical composition (18). Commonly studied polymers for bone regeneration fall into two main categories: biodegradable and nonbiodegradable. Nondegradable polymers are frequently used in bone research due to desirable mechanical properties. The most popular nonbiodegrable bone grafts are acrylic based bone cements. Poly (methylmethacrylate) (PMMA) is widely used in vertebroplasty to treat compressive fractures or fragile vertebrae. PMMA cements have high initial modulus and yield strength and are appropriate choices for load bearing defect sites (19). However these cements do not degrade over time, have high exothermic reaction conditions that can harm host tissue, and can loosen if not properly fixed (20).

Popular biodegradable polymers for biomedical applications include poly(esters), poly(propylene) fumarate, polyphosphazenes, and polyurethanes (21). All of these have scaffolds degrade to noncytotoxic products and support cellular attachment. Poly(esters) of poly(lactic acid) (PLA) and poly(glycolic acid) (PGA), as well as co-polymers of the two, were developed as some of the first degradable materials for tissue engineering applications and are well defined in terms of design and *in vivo* performance (22); however, PLA and PGA use in bone regeneration has been limited by low mechanical strength, small pore size, and hydrophobicity (23). Polyurethanes (PUR) have been used as scaffolds for tissue engineering since the 1960s (24). These biocompatible materials have non-toxic degradation products that are readily eliminated by the body. They have tunable degradation and mechanical properties and can be used for a variety of applications, including skin and bone regeneration (25). In addition, PUR foams can be injected and harden *in vivo* to fill a variety of defect sizes and shapes. The main components of the PUR are (1) isocyanate or isocyanate-terminated prepolymer and (2) a polyol component with hydroxyl- or amino-functionalization that reacts with isocynate (NCO) groups (21). The combination of the two species initiates a gelling reaction that forms a polymer network with urethane linkages. Water, present either in the reaction components or at the injection site, can also react with the NCO groups to produce carbon dioxide in a blowing reaction. The catalyst choice will specify the blowing and gelling reaction rates, so this can be tailored based on the desired properties of the final scaffold (26). Catalysts with preferentially higher blowing reaction rates will produce highly porous, interconnected scaffolds.

Another category of bone substitute materials are biocompatible ceramics including tricalcium phosphate (TCP) and hydroxyapatite (HA), which is the major inorganic component of bone. These ceramics are osteoconductive materials that stimulate bone healing and are widely used in bone regeneration. Ceramics have favorable compression strength, resistance to wear, and frictional properties (27). Ceramics exist in a variety of forms, including powders, granules, cements, and coatings (4). The pitfalls of ceramics include brittleness, difficulty in shaping, and slow degradation (of HA), leaving them unsuitable to provide structural support in many bone graft applications (28). To create better mechanical properties while preserving the osteoconductive nature of ceramics, it is possible to combine synthetic polymers with ceramics for bone graft applications (29).

Bioactive glasses, first invented by Larry Hench in 1969, are degradable glasses comprised of Na_2O-CaO-SiO_2-P_2O_5 that have been used in place of ceramics for bone regeneration (30). Bioglass 45S5, the original formula of the composition 46.1 mol% SiO_2, 23.4 mol% Na_2O, 26.9 mol% CaO, and 2.6mol% P_2O_5 has been used to repair more than a million cases of jaw and orthopaedic defects in patients (31). Bioactive glasses have numerous properties that contribute to their success as bone grafts, namely that they aid in osteoblastic differentiation, attachment, and proliferation and support osteogenesis and protein activity (32). The high elastic modulus and fracture toughness of these glasses makes them appropriate choices for both trabecular and cortical bone grafts (12). Degradation and bioactivity can be tailored based on changing chemical composition and substituting other biologically beneficial chemicals such as strontium (33) and ZnO (34). Like ceramics, bioactive glasses are brittle and hybrids have been developed to introduce toughness while still retaining the desirable bioactive properties of the glass (35).

Combining inorganic phases, like ceramics and bioactive glasses, with polymers improves the mechanical properties of scaffolds and widely expands the potential applications of these biomaterials. Combining biodegradable polymers with inorganics offers better control over pore structure, easier delivery and moldability, and helps reduce the effect of the poor mechanical properties of brittle solid fillers (28). Bioactive glass/polymer scaffolds have also been shown to support osteoblast attachment and proliferation *in vitro* and are good candidates for bone regeneration (36). Ceramic/polymer composites have been developed with increased mechanical stability and improved material-tissue interaction with promising *in vivo* test results (37). Some previous methods for preparing ceramic/polymer composites use organic solvents, such as solvent casting and phase separation, the residues of which have the potential to harm host tissue (38, 39). More recently developed PUR biocomposites have overcome some of these limitations as they can be prepared by mixing the reactive liquid components of the PUR together with the solid filler directly, and the composite sets over a tailorable working time with a scaffold that has tunable mechanical and physical properties (40). Polyurethane biocomposites have been successfully used to treat a variety of *in vivo* models with allograft, ceramic, and bioactive glass particles (41, 42).

Bone Morphogenetic Proteins (BMPs) are a class of growth factors derived from bone that are implicated in embryogenesis, skeletal formation, hematopoiesis, and neurogenesis (43). The activity of BMPs was initially discovered in the 1960s, but these proteins were not isolated until the 1980s (44). BMPs are classified as a part of the Tumor Growth Factor-β superfamily (TGF-β), and BMP-2 is the only one of the group that has been demonstrated to induce the entire process of *de novo* bone formation (45). Recombinant human BMP-2 (rhBMP-2) aids in cell-cell and cell-environment signaling and is FDA approved for use in bone repair in orthopaedic applications for open tibia fractures and anterior lumbar interbody spinal fusion and craniomaxillofacial applications for maxillary sinus augmentation and alveolar ridge augmentation (46). Some complications have arisen with rhBMP-2 delivery, primarily with off-label use in the cervical spine. High doses of rhBMP-2 have been implicated in longer hospital stays, ectopic bone formation, swelling (which can lead to airway blockage), and neurological compression (47).

To reduce the risk of complications associated with rhBMP-2, it is possible to reduce (1) the total delivered dose or (2) the bolus release of growth factor. RhBMP-2 quickly disperses from the defect site and is cleared from the body when delivered by an inefficient carrier. When delivered in a buffer solution, 95% of BMP-2 is rapidly cleared from the delivery site, while this drops to 45-85% when the protein is combined with gelatin or collagen (48). The kinetics of protein delivery, which influence cellular differentiation and healing, are dependent on the scaffold chemistry, porosity, polymer network, and other characteristics of the delivery system (49, 50). It is of great importance to study the rhBMP-2 release for all potential delivery vehicles due to the complicated nature of predicting release kinetics with the number of confounding factors. The commercially available acellular collagen sponge (ACS) carrier provides a bolus release of rhBMP-2 within approximately a week (51), while a PLGA microparticle/calcium phosphate delivery system retains over half of the rhBMP-2 after 4 weeks (52). By using biomaterials to sequester the growth factor at the application site, the efficacy of the growth factor is retained. Additionally, the therapeutic protein dose can be reduced to limit the side effects associated with high doses of rhBMP-2 (53).

Biomaterial delivery

The success or failure of biomaterial delivery can depend on the requirements of the anatomical site and the method by which the material is administered to the defect. The delivery technique largely depends on the physical characteristics of the composite. Some polymer scaffolds are injectable through narrow syringes, which may not be feasible with granular ceramics. In minimally invasive procedures, such as spinal vertebroplasty, a reactive paste is delivered through a thin needle that flows to fill the defect site and hardens to maintain the space (54). Ceramics are often delivered as granules within a defect site (55, 56), combined with a rhBMP-2 delivery system as an osteoconductive matrix (57), or used as an autograft extender to decrease the necessary volume of harvested autograft (58, 59). Bioactive glass particles have also been tested as bone grafts alone (60) or as autograft extenders (61).

Composite materials of ceramics and polymers have different delivery requirements than the individual components. Filter-pressing (liquid phase separation) can occur due to extrusion pressure through a syringe with a polymer containing suspended granules of a solid phase when the liquid phase flows more quickly than the solid phase. This leads to local changes in mixture composition, making it necessary to test the injectability of any biomaterials of interest (62). Filter-pressing can be minimized with a system containing a high initial viscosity. Injectability is maintained with the requirement of a low yield stress to start the flow through the syringe (41).

However, the definition of injectability is often poorly defined and varies among studies. Clinically, injectability can depend on applied force (whether injection is by hand or with an injection gun), ratio of particle and liquid phases, particle size, and solution viscosity (63).

Biomaterial characterization

There are a variety of available methods to characterize the physical and chemical properties of biomaterial scaffolds used in bone tissue engineering. These techniques can provide initial information regarding the mechanical integrity, porosity and pore structure, and reaction conditions for a specific material of interest.

An ideal bone graft will have similar mechanical properties to the host bone it is expected to replace and, if biodegradable, will maintain mechanical integrity throughout the remodeling process (64). Compression properties are frequently reported for biomaterials as compression is easily tested and demonstrates the similarity to host bone. Human bone mechanical properties can vary widely depending on the anatomical site and age and health of patient, with compressive strengths of 5-40 MPa and 100-230 MPa for human trabecular and cortical bone respectively. (40) Mechanical testing is often based on ASTM standards which aim to create reproducibility in testing methods. Compressive modulus can be tested by applying a fixed load on a cylindrical sample (with a height twice that of the diameter) at a constant strain rate until sample failure (65). Samples can be preloaded with a small amount of stress to account for variability and imperfections within samples. From the resulting stress-strain curve, the elastic modulus is defined as the slope of the initial linear portion.

Fatigue testing should be conducted on materials aimed for weight bearing applications as these will experience cyclic loading profiles in the body (66). In fatigue testing, samples are subjected to cyclic loads at constant stress or strain at a physiologically relevant frequency (67). Testing occurs until either a given number of cycles are reached or sample failure occurs. Resulting S:N curves (stress or strain vs cycles to failure) can be constructed from the collected data. Stress vs strain curves at various cycles over fatigue life can also be plotted to show the creep fatigue over time. Bone is highly elastic in nature and thus can withstand a high number of cycles until failure, over 2200 cycles was reported for human cortical bone tested in compression fatigue at 98MPa (66). Fatigue failure and fatigue crack propagation are two of the main concerns with bone cement failure, and common bone cements like PMMA do not fare well under fatigue testing due to low ductility. These cements cannot withstand high deformation before fracturing, making them less suitable candidates as bone grafts in load bearing sites (68).

To promote osteogenesis, scaffold structure and morphology should mimic that of the host bone. Trabecular bone is comprised of HA crystals in an organic matrix with 50-90% porosity (69). A biomaterial for bone regeneration should be macroporous (pores > 80-100 µm) to facilitate cellular infiltration (4). Theoretical porosity can be determined gravimetrically if the density of the biomaterial (or the components of a composite) is known. By taking the weight and volume of a uniformly shaped scaffold and calculating both the actual and theoretical density, the gravimetric porosity is determined as the difference between the two. In addition, scanning electron microscopy (SEM) image analysis can provide quantitative and qualitative details regarding pore shape, pore size, and total porosity.

Biomaterials destined for patient applications should have viscosities and working times that are clinically relevant. Viscosity of a graft is important for materials that will be delivered through a syringe into the defect site. Additionally, the working time of a graft is important for reactive mixtures that must be delivered within a specific time frame. Viscosity of polymer composites is most often measured by rheometry. For reactive mixtures, initial viscosity is measured without the additional of catalyst (70) or at a predetermined time after catalyst addition (71). Due to the viscoelastic nature of many polymer composites, samples are run using oscillation frequency applied over a frequency range with constrained strain (72). The fixed strain is initially determined by amplitude sweep to detect the linear viscoelastic region. From the dynamic viscosity data, a Cox-Merz transformation can be applied to obtain steady state viscosity as a function of shear rate (73). Cure profiles of reactive composites can also be measured by rheometry using an oscillatory time sweep at a fixed frequency and strain amplitude (74). The cross-over point of the resulting storage modulus (G') and loss modulus (G'') denotes the working time of the composite. Ideally, the working time is long enough to give surgeons a chance to mix and prepare the materials while still setting within a reasonable time after injection.

Bone remodeling

Bone constantly goes through a dynamic remodeling process whereby osteoclasts break down old bone and osteoblasts rebuild it. Osteoclasts are formed from the fusion of cells of the monocyte-macrophage lineage. Resorption of bone proceeds through the formation of resorption lacunae on the surface of bone and the acidification of the vacuoles by proton pumps (75, 76). There are a significant number of variables that contribute to resorption including protein adhesion, integrin binding, and growth factor expression levels (77-79). All of these variables regulate the extent to which natural bone or synthetic matrices are resorbed in the body. There is also growing evidence that osteoclast-derived factors may influence differentiation or activity of osteoblasts and in so doing stimulate bone formation (80).

Graft remodeling

Biomaterial compatibility is understood to solely depend on the graft remaining in a state of complete chemical and biological inertness, with no recognition or reaction from the immune system (81). While initial graft biocompatibility is necessary to prevent acute immune system response and promote graft integration, it is equally important that the decomposition products are non-toxic and easily cleared by the body (82). Grafts with high degradation rates or degradation byproduct toxicity are more likely to induce immune cell response.

For biodegradable polymers, compatibility and graft success depends, in part, on the kinetics of degradation and the degradation products. Synthetic polymers are often preferred based on the uniform and tailorable degradation kinetics which may be dependent on either hydrolytic or enzymatic degradation (21). Polymers that degrade hydrolytically contain chemical groups in the polymer backbone that are susceptible to cleavage in the presence of water molecules. In the specific case of polyurethanes, hydrolytic degradation is associated with cleavage at ester linkages producing α-hydroxy acids and carboxylic acid. These degradation products are acidic, creating an autocatalytic degradation feedback loop where the highly acidic local environment further promotes polymer degradation (83). Polyurethanes can also undergo oxidative degradation, which has been shown to significantly increase *in vivo* degradation, in the presence of reactive oxygen species (ROS) secrete by cells (84). *In vitro* replication of *in vivo* oxidative degradation has been proposed through the use of oxidative media containing $CoCl_2$ in H_2O_2 in which reactive hydroxyl radicals form (85).

It is generally thought that calcium phosphate degradation is a process based on both chemical dissolution under physiological conditions and cell mediated degradation; however, the relative rates of these two processes is not well understood (86). Solubility of calcium phosphates depends on both chemical composition and physical properties including crystal size, impurities, surface area, and porosity (4). Since osteoclast resorption is partly based on vacuole acidity, the rate at which ceramics resorb is dependent on both osteoclast activity and calcium phosphate dissolution under highly acidic conditions. However, highly soluble ceramics release many ions into the cellular environment which can impede osteoclast activity through a negative feedback loop (87). While osteoclasts contribute to the dissolution of ceramics through acidic resorption lacunae, they are simultaneously able to phagocytose ceramic crystals (88). The number of factors that play a role in ceramic resorption and dissolution complicates the *in vitro* study of these processes. There has been a significant amount of research previously on the *in vitro* resorption potential of ceramics, including TCP and HA, with a variety of conclusions. One method to simulate osteoclast resorption *in vitro* is to test material dissolution at pH=4.5, mimicking the acidic conditions in a resorption lacunae (89). This bulk measurement, however, does not account for cell-material interaction or presence of signaling molecules, and many research groups have moved to using *in vitro* cell culture assays. One study using primary osteoclasts harvested from mice found that resorptions pits on TCP were larger and more defined than on HA, where osteoclasts were evident but resorption activity was not (90). Another group showed that active osteoclast resorption rather than passive dissolution was the predominant factor in calcium phosphate degradation, as measured through Ca^{2+} release on samples cultured with or without active osteoclasts (91). With previous osteoclast studies, there are a variety of cell culture techniques and analysis methods.

Once implanted in a bony site, bioactive glasses quickly bond with host bone through the formation of a hydroxyapatite layer following ionic dissolution. These ions are also thought to contribute to the bioactivity of the bioactive glass, where degradation influences cellular signaling and differentiation. Previous work has demonstrated that ionic dissolution products from bioactive glass promote differentiation of human osteoblasts *in vivo* (92). The characterization of bioactive glass dissolution is complicated by a number of associated factors, including temperature, type of media, pH, agitation conditions (93). *In vitro* studies have been suggested to better replicate *in vivo* conditions, however there is not a wealth of information regarding the resorptive potential of bioactive glasses. Some studies have examined the presence of osteoclasts on bone grafts implanted *in vivo* (94, 95). One *in vitro* study has shown that osteoclasts will differentiate and resorb a bioactive glass scaffold (96). Another group showed that strontium substituted bioactive glass inhibits osteoclast resorption through ionic dissolution (97). While a majority of previous research with bioactive glasses uses 45S5 bioactive glass or glasses of similar composition, in part due to commercial availability, more recently new hybrid bioactive glass materials have been developed with tailorable degradation and dissolution properties (31). Additional research has focused on investigated the effects of bioactive glasses doped with trace amounts of Zn, Sr, Mg, and Cu on bioactivity (98).

Animal models

Bone grafting procedures are inherently complex processes, making it difficult to study differences in success rates of biomaterials and tissue engineered scaffolds clinically. Confounding factors can include patient variables (smoking and drinking rates, age, general health), bone graft type and source, and surgical technique (99). Additionally, newly developed materials are required to undergo rigorous testing both *in vitro* and *in vivo* to determine biocompatibility, mechanical integrity, degradation profiles, and efficacy (100). For these reasons, animal models are necessary to safely and effectively decipher how different factors contribute to surgical success or failure.

In tissue engineering, proper animal models aid in the comparison of materials across different studies and across different laboratories. Additionally, *in vivo* models can provide more understanding of cellular activity and tissue response to implanted biomaterials. The microenvironment in a surgical site is comprised of a multitude of cell types with a variety of physical and chemical signaling modalities and *in vitro* assays are often limited to one or a few cell types (100). Desirable characteristics for animal models include physiological and pathological similarities to the human condition being studied and a short time frame for healing response (101). Ethically, choosing an animal model and species must include considerations for cost to acquire and house subjects, tolerance to captivity, acceptability to the general public, and availability. Institutional Animal Care and Use Committees (IACUCs) are in place at research institutions to consider and approve the requirement for animal species and model.

Rats and mice are frequently used as proof-of-concept animal models due to lower cost and faster experimental time points (102). The rat calvaria model is a popular choice to test biomaterials anticipated for craniomaxillofacial applications. This defect is an orthotopic model with minimized contact between host bone and the implanted biomaterial, proving to be a strenuous test for bone bridging and healing (103). The rat femur segmental defect is another established model in orthopaedic research, which replicates some of the conditions of healing in human segmental defects (104). These models have a reproducible, defined geometry making it easier to analyze by histology and microcomputed tomography (μCT). However, the small size of many mouse and rat defects can pose a challenge for delivery of biomaterials. Additionally, rodent models are less important as a product moves along the pipeline toward clinical use. Defects in rodent models are too small to test clinical size defects, which are often 6-10mm in thickness, and the diffusion distances and cellular ingrowth rates in rodents do not match those seen in human defects (101).

Rabbit models are used in over one third of musculoskeletal animal studies due to size, ease of handling, and quick maturation. Rabbit bones differ in both size and shape as compared to human bones, and force loading is dissimilar due to the quadrupedal stance and high degree of knee flexion (102). Like rodent models, rabbit bones experience faster remodeling and skeletal dynamics than humans, making it difficult to extrapolate healing rates (100). Rabbit models are frequently used to screen and test biomaterials prior to experiments in larger preclinical models. For biomaterials intended for craniomaxillofacial applications, it has been suggested to move from rat to rabbit calvarial models before moving into canine and nonhuman primate mandibles (105). A common starting model for spine research is a single level bilateral spinal fusion in rabbits, first developed by Boden and colleagues in the 90s (99). Additionally, there are a number of established orthopaedic models for defect creation in the femur and tibia of rabbits (106).

Canine models are frequently used in bone grafting experimentation due to their suitable size and similarity in bone structure to humans; however, their use is limited due to ethical considerations related to use of the species and growing concerns from the general population (102). From 1970 to 2001, 9% of orthopaedic and trauma research used canine models (107). Canine bone size and shape can vary based on age and breed of the animal, but there are commercially available surgical tools specific for the dogs making defect creation and grafting easier and more replicable. Similar to rabbits, the quadrupedal stance of the dog can influence graft placement and healing when compared to humans. In regards to bone structure, canine bone has a higher mineral density than human bone and can withstand higher compressive strain prior to failure (100). Canine models are particularly common in dental research as the canine mandible is similar to that of humans, and the required critical-size defect has been extensively studied (108). There are also a number of accepted osteotomy (106) and spinal fusion (101) models in canines.

Skeletally mature sheep and goats have similar body mass and long bone dimensions to adult humans, and sheep and goat models are commonly used in orthopaedic bone research. Bone composition and turnover rate is similar between human and sheep bone; however, mature sheep bone has higher trabecular density and bone strength than that of adult humans (109). Sheep models are frequently chosen for bone grafting research due to similar rates of cellular infiltration and bony ingrowth in porous implants in sheep and humans (100). Additionally, sheep models may be more desirable than canine models due to ethical considerations of research on perceived companion animals. Sheep models are primarily used to study fractures, bone lengthening, osteoporosis, and osteoarthritis (107).

Porcine models are used in a variety of bone regeneration experiments; however, the large size of commercial pigs often precludes their use. The development of miniature pigs and micropigs alleviated some of the concerns with the species, but these smaller animals are still considered difficult to handle and expensive to house. Pigs are chosen to study bone necrosis, cartilage and bone fracture, and bony ingrowth of graft and dental implants (100). The pig mandible is the most similar to the human mandible, in regards to gross anatomy and physiology, of any of the previously discussed species (101). The eruption of teeth and size of dentition of the miniature pig is comparable to that of humans, and these pigs experience periodontal disease (gingivitis) in a progression that closely resembles the diseased state of humans (110). Additionally, the requirement for a critical-size defect in the minipig mandible has been established, making it an acceptable model for craniomaxillofacial research (111).

Non-human primates are considered the most appropriate species for bone research, but there are significant implications regarding their cost, potential zoonotic disease transmission, and handling difficulties (100). In bone tissue engineering research non-human primate models are often chosen after extensive study of bone repair and remodeling has already been conducted in other animals. There are a number of craniomaxillofacial models in non-human primates including periodontal disease bone regeneration (112), calvarial defects (113), dental implants (114), and mandibular ridge augmentation (115). In particular, non-human primate models are important to test drug dosing levels prior to clinical testing, as therapeutic doses differ between species (116). Orthopaedic models in non-human primates include osteotomy (117), spinal fusion (118), and segmental defects (119).

With all of the available animal models for testing biomaterials destined for clinical applications, it is important that researchers take into account the longevity of the study, cost, animal housing, and ethical considerations when choosing an appropriate species and defect site.

Analysis of *in vivo* studies

Once a satisfactory model has been chosen and the experiment conducted, it is equally important to use one or more suitable evaluation techniques to analyze the success or failure of the study. There are a variety of both *in vivo* and *ex vivo* techniques to evaluate cellular infiltration, new bone growth, and scaffold/biomaterial degradation. These techniques include radiography, computed tomography (CT) and micro CT (μCT), and histology. A combination of one or more of these methods, both qualitative and quantitative, can help to fully elucidate the outcome of a study.

Radiography is an imaging technique that uses x-rays to view anatomical sites of interest. Radiographs are non-destructive, can be taken without the need to harvest tissue, and can be used to monitor bone growth throughout a study; however, these are low resolution, two-dimensional (2D) representations of 3D structures and do not provide a significant amount of information regarding tissue structure (120). Additionally, when ceramics are used alone or as composites in bone grafting, it is impossible to determine new bone formation due to the highly radiopaque nature of ceramics overshadowing the bony ingrowth (121).

CT and μCT are non-destructive analysis techniques that allow for qualitative and quantitative evaluation of biomaterials and *in vivo* response. CT scans are used clinically to detect anatomic structures in multiple dimensions, which isn't possible with conventional radiographic techniques (122). CT scans can be used to create personalized knee and hip implants, giving more control on customizing the articulating component and the bone-implant interface (123). These custom implants lead to lower risk of complications such as implant loosening and surgical intervention; however, the technique is more expensive than conventional implants. In animal research, CT analysis has been used to accurately depict the size and quality of created defects (124). With the development of higher resolution micro-CT (μCT), conventional CT analysis is no longer a commonly used method in bone tissue research.

μCT scanning of bone, developed in the 1980s, has a much higher resolution than tradition CT imaging and can give a full three dimensional (3D) depiction of the architecture of bone with the ability to view and quantify individual trabeculae (125). For animal studies μCT imaging is particularly helpful in assessing the 3D growth of new bone and analyzing spatial and temporal changes in bone quantity and quality (126). One of the most frequently measured parameters with μCT is the volume of ossified tissue within a region of interest, referred to as bone volume/total volume (BV/TV). While μCT provides information about the quantity of bone, it also provides information pertaining to the quality of mineralized tissue. At a minimum to describe the trabecular architecture of bone, researchers should report the trabecular number (Tb.N), trabecular thickness (Tb.Th), and trabecular separation (Tb.Sp) of a volume of interest (127). One of the limitations of μCT analysis is the difficulty in separating residual scaffold or inorganic phases from newly ossified tissue (128). Ossified tissue is normally separated from soft tissue by thresholding 3D reconstructions based on density of the phases following calibration to known densities. This technique does not frequently work when separating bioactive glasses or ceramics from bone due to overlapping mineral densities in the phases. While it does have some drawbacks, μCT analysis is widely used in the field of bone engineering to accurately depict and measure quantity and quality of new bone within a region of interest.

Histological analysis involves 2D sections taken from fixed and prepared tissue sections of interest which can be stained in a number of ways to visualize cell species, bone, fibrous tissue, marrow, and soft tissue (120). For bone engineering, commonly utilized stains include Hematoxylin and Eosin, Masson-Goldner trichrome, Movat’s pentachrome, Alcian blue, and Sanderson’s rapid bone. Each stain provides different information regarding tissue formation and cellular populations within a sample of interest, and a thorough description of the stains and their outcomes is available (129). Once appropriated stained, the researcher can distinguish ossified tissue from soft tissue and residual biomaterial. Staining can also show inflammatory response (and cell populations), bone deposition, biomaterial degradation, resorption by macrophages and osteoclasts, and extracellular matrix formation. Histomorphometry is the quantification of histological images in regards to bone area, tissue area, and residual biomaterial within a specified region of interest by identifying and measuring these phases. The use of standardized histomorphometry procedures minimizes bias that can be introduced with qualitative evaluation of histology sections and can aid in the evaluation of experimental success. Additionally, histomorphometry can help increase reproducibility inter-study and intra-study.

By using some or all of the analysis techniques of radiography, µCT, histology, and histomorphometry, researchers can evaluation outcomes of *in vivo* experiments. These methods have standardized guidelines from the literature that can help to minimize differences in studies arising from bone harvesting techniques, available instrumentation, researcher aptitude, processing techniques, and a number of other factors.

References

1. Schultheiss, D., Bloom, D.A., Wefer, J., andJonas, U. Tissue engineering from Adam to the zygote: historical reflections. World Journal of Urology **18**, 84, 2000.
2. Lysaght, M.J., andHazlehurst, A.L. Tissue engineering: the end of the beginning. Tissue engineering **10**, 309, 2004.
3. Amini, A.R., Laurencin, C.T., andNukavarapu, S.P. Bone Tissue Engineering: Recent Advances and Challenges. Critical reviews in biomedical engineering **40**, 363, 2012.
4. Verron, E., Khairoun, I., Guicheux, J., andBouler, J.-M. Calcium phosphate biomaterials as bone drug delivery systems: a review. Drug Discovery Today **15**, 547, 2010.
5. Calori, G.M., Mazza, E., Colombo, M., andRipamonti, C. The use of bone-graft substitutes in large bone defects: any specific needs? Injury **42 Suppl 2**, S56, 2011.
6. Giannoudis, P.V., Dinopoulos, H., andTsiridis, E. Bone substitutes: An update. Injury **36**, S20, 2005.
7. Khan, S.N., Cammisa, F.P., Sandhu, H.S., Diwan, A.D., Girardi, F.P., andLane, J.M. The Biology of Bone Grafting. Journal of the American Academy of Orthopaedic Surgeons **13**, 77, 2005.
8. Khan, Y., Yaszemski, M.J., Mikos, A.G., andLaurencin, C.T. Tissue Engineering of Bone: Material and Matrix Considerations. The Journal of Bone & Joint Surgery **90**, 36, 2008.
9. Betz, R.R. Limitations of autograft and allograft: new synthetic solutions. Orthopedics **25**, S561, 2002.
10. Seeherman, H.J., Li, X.J., Bouxsein, M.L., andWozney, J.M. rhBMP-2 Induces Transient Bone Resorption Followed by Bone Formation in a Nonhuman Primate Core-Defect Model. The Journal of Bone & Joint Surgery **92**, 411, 2010.
11. Belfrage, O., Flivik, G., Sundberg, M., Kesteris, U., andTägil, M. Local treatment of cancellous bone grafts with BMP-7 and zoledronate increases both the bone formation rate and bone density. Acta Orthopaedica **82**, 228, 2011.
12. Moore, W.R., Graves, S.E., andBain, G.I. Synthetic bone graft substitutes. ANZ Journal of Surgery **71**, 354, 2001.
13. Swetha, M., Sahithi, K., Moorthi, A., Srinivasan, N., Ramasamy, K., andSelvamurugan, N. Biocomposites containing natural polymers and hydroxyapatite for bone tissue engineering. International Journal of Biological Macromolecules **47**, 1, 2010.
14. Malafaya, P.B., Silva, G.A., andReis, R.L. Natural–origin polymers as carriers and scaffolds for biomolecules and cell delivery in tissue engineering applications. Advanced Drug Delivery Reviews **59**, 207, 2007.
15. Pillai, O., andPanchagnula, R. Polymers in drug delivery. Current Opinion in Chemical Biology **5**, 447, 2001.
16. Burg, K.J.L., Porter, S., andKellam, J.F. Biomaterial developments for bone tissue engineering. Biomaterials **21**, 2347, 2000.
17. Nair, L.S., andLaurencin, C.T. Biodegradable polymers as biomaterials. Progress in Polymer Science **32**, 762, 2007.
18. Gunatillake, P.A., andAdhikari, R. Biodegradable synthetic polymers for tissue engineering. Eur Cell Mater **5**, 1, 2003.
19. Lim, T.-H., Brebach, G.T., Renner, S.M., Kim, W.-J., Kim, J.G., Lee, R.E., Andersson, G.B., andAn, H.S. Biomechanical evaluation of an injectable calcium phosphate cement for vertebroplasty. Spine **27**, 1297, 2002.

20. Moreira-Gonzalez, A., Jackson, I.T., Miyawaki, T., Barakat, K., andDiNick, V. Clinical outcome in cranioplasty: critical review in long-term follow-up. Journal of Craniofacial Surgery **14**, 144, 2003.
21. Guelcher, S.A. Biodegradable polyurethanes: synthesis and applications in regenerative medicine. Tissue Engineering Part B: Reviews **14**, 3, 2008.
22. Uhrich, K.E., Cannizzaro, S.M., Langer, R.S., andShakesheff, K.M. Polymeric systems for controlled drug release. Chemical reviews **99**, 3181, 1999.
23. Wu, Y.-C., Shaw, S.-Y., Lin, H.-R., Lee, T.-M., andYang, C.-Y. Bone tissue engineering evaluation based on rat calvaria stromal cells cultured on modified PLGA scaffolds. Biomaterials **27**, 896, 2006.
24. Bruin, P., Veenstra, G., Nijenhuis, A., andPennings, A. Design and synthesis of biodegradable poly (ester-urethane) elastomer networks composed of non-toxic building blocks. Die Makromolekulare Chemie, Rapid Communications **9**, 589, 1988.
25. Guelcher, S.A., Patel, V., Gallagher, K.M., Connolly, S., Didier, J.E., Doctor, J.S., andHollinger, J.O. Synthesis and in vitro biocompatibility of injectable polyurethane foam scaffolds. Tissue engineering **12**, 1247, 2006.
26. Page, J.M., Prieto, E.M., Dumas, J.E., Zienkiewicz, K.J., Wenke, J.C., Brown-Baer, P., andGuelcher, S.A. Biocompatibility and chemical reaction kinetics of injectable, settable polyurethane/allograft bone biocomposites. Acta Biomaterialia **8**, 4405, 2012.
27. Hutmacher, D.W., Schantz, J.T., Lam, C.X.F., Tan, K.C., andLim, T.C. State of the art and future directions of scaffold-based bone engineering from a biomaterials perspective. Journal of Tissue Engineering and Regenerative Medicine **1**, 245, 2007.
28. Kim, S.-S., Sun Park, M., Jeon, O., Yong Choi, C., andKim, B.-S. Poly(lactide-co-glycolide)/hydroxyapatite composite scaffolds for bone tissue engineering. Biomaterials **27**, 1399, 2006.
29. Yoshii, T., Dumas, J.E., Okawa, A., Spengler, D.M., andGuelcher, S.A. Synthesis, characterization of calcium phosphates/polyurethane composites for weight-bearing implants. Journal of Biomedical Materials Research Part B: Applied Biomaterials **100**, 32, 2012.
30. Lu, H.H., Pollack, S.R., andDucheyne, P. 45S5 bioactive glass surface charge variations and the formation of a surface calcium phosphate layer in a solution containing fibronectin. Journal of biomedical materials research **54**, 454, 2001.
31. Jones, J.R. Review of bioactive glass: from Hench to hybrids. Acta Biomater **9**, 4457, 2013.
32. Chen, Q.Z., Efthymiou, A., Salih, V., andBoccaccini, A.R. Bioglass®-derived glass–ceramic scaffolds: Study of cell proliferation and scaffold degradation in vitro. Journal of Biomedical Materials Research Part A **84A**, 1049, 2008.
33. O'Donnell, M.D., andHill, R.G. Influence of strontium and the importance of glass chemistry and structure when designing bioactive glasses for bone regeneration. Acta Biomaterialia **6**, 2382, 2010.
34. Srivastava, A.K., andPyare, R. Characterization of ZnO Substituted 45S5 Bioactive glasses and glass-ceramics. Journal of Materials Science Research **1**, p207, 2012.
35. Mahony, O., Tsigkou, O., Ionescu, C., Minelli, C., Ling, L., Hanly, R., Smith, M.E., Stevens, M.M., andJones, J.R. Silica-Gelatin Hybrids with Tailorable Degradation and Mechanical Properties for Tissue Regeneration. Advanced Functional Materials **20**, 3835, 2010.
36. Lu, H.H., El-Amin, S.F., Scott, K.D., andLaurencin, C.T. Three-dimensional, bioactive, biodegradable, polymer–bioactive glass composite scaffolds with improved mechanical

properties support collagen synthesis and mineralization of human osteoblast-like cells in vitro. Journal of Biomedical Materials Research Part A **64A**, 465, 2003.

37. Rezwan, K., Chen, Q.Z., Blaker, J.J., andBoccaccini, A.R. Biodegradable and bioactive porous polymer/inorganic composite scaffolds for bone tissue engineering. Biomaterials **27**, 3413, 2006.

38. Lee, S.H., Kim, B.S., Kim, S.H., Kang, S.W., andKim, Y.H. Thermally produced biodegradable scaffolds for cartilage tissue engineering. Macromolecular bioscience **4**, 802, 2004.

39. Jung, Y., Kim, S.-S., Kim, Y.H., Kim, S.-H., Kim, B.-S., Kim, S., Choi, C.Y., andKim, S.H. A poly (lactic acid)/calcium metaphosphate composite for bone tissue engineering. Biomaterials **26**, 6314, 2005.

40. Dumas, J.E., Davis, T., Holt, G.E., Yoshii, T., Perrien, D.S., Nyman, J.S., Boyce, T., andGuelcher, S.A. Synthesis, characterization, and remodeling of weight-bearing allograft bone/polyurethane composites in the rabbit. Acta Biomaterialia **6**, 2394, 2010.

41. Dumas, J.E., BrownBaer, P.B., Prieto, E.M., Guda, T., Hale, R.G., Wenke, J.C., andGuelcher, S.A. Injectable reactive biocomposites for bone healing in critical-size rabbit calvarial defects. Biomed Mater **7**, 024112, 2012.

42. Talley, A.D., Kalpakci, K.N., Shimko, D.A., Zienkiewicz, K., Cochran, D., andGuelcher, S. Effects of rhBMP-2 Dose and Ceramic Composition on New Bone Formation and Space Maintenance in a Canine Mandibular Ridge Saddle Defect Model. Tissue Engineering 2016.

43. Bragdon, B., Moseychuk, O., Saldanha, S., King, D., Julian, J., andNohe, A. Bone Morphogenetic Proteins: A critical review. Cellular Signalling **23**, 609, 2011.

44. Chen, D., Zhao, M., andMundy, G.R. Bone morphogenetic proteins. Growth factors **22**, 233, 2004.

45. Wozney, J.M. Bone Morphogenetic Proteins. Progress in Growth Factor Research **1**, 267, 1989.

46. Kretlow, J.D., Young, S., Klouda, L., Wong, M., andMikos, A.G. Injectable Biomaterials for Regenerating Complex Craniofacial Tissues. Advanced materials (Deerfield Beach, Fla) **21**, 3368, 2009.

47. Cahill, K.S., Chi, J.H., Day, A., andClaus, E.B. PRevalence, complications, and hospital charges associated with use of bone-morphogenetic proteins in spinal fusion procedures. JAMA **302**, 58, 2009.

48. Hollinger, J.O., Schmitt, J.M., Buck, D.C., Shannon, R., Joh, S.-P., Zegzula, H.D., andWozney, J. Recombinant human bone morphogenetic protein-2 and collagen for bone regeneration. 1998.

49. Boerckel, J.D., Kolambkar, Y.M., Dupont, K.M., Uhrig, B.A., Phelps, E.A., Stevens, H.Y., Garcia, A.J., andGuldberg, R.E. Effects of protein dose and delivery system on BMP-mediated bone regeneration. Biomaterials **32**, 5241, 2011.

50. Chew, S.Y., Wen, J., Yim, E.K.F., andLeong, K.W. Sustained Release of Proteins from Electrospun Biodegradable Fibers. Biomacromolecules **6**, 2017, 2005.

51. Luginbuehl, V., Meinel, L., Merkle, H.P., andGander, B. Localized delivery of growth factors for bone repair. Eur J Pharm Biopharm **58**, 197, 2004.

52. Ruhé, P.Q., Boerman, O.C., Russel, F.G.M., Spauwen, P.H.M., Mikos, A.G., andJansen, J.A. Controlled release of rhBMP-2 loaded poly(dl-lactic-co-glycolic acid)/calcium phosphate cement composites in vivo. Journal of Controlled Release **106**, 162, 2005.

53. Haidar, Z., Hamdy, R., andTabrizian, M. Delivery of recombinant bone morphogenetic proteins for bone regeneration and repair. Part A: Current challenges in BMP delivery. Biotechnology Letters **31**, 1817, 2009.
54. Moreland, D.B., Landi, M.K., andGrand, W. Vertebroplasty: techniques to avoid complications. The Spine Journal **1**, 66, 2001.
55. Fellah, B.H., Gauthier, O., Weiss, P., Chappard, D., andLayrolle, P. Osteogenicity of biphasic calcium phosphate ceramics and bone autograft in a goat model. Biomaterials **29**, 1177, 2008.
56. Horch, H.H., Sader, R., Pautke, C., Neff, A., Deppe, H., andKolk, A. Synthetic, pure-phase beta-tricalcium phosphate ceramic granules (Cerasorb®) for bone regeneration in the reconstructive surgery of the jaws. International Journal of Oral and Maxillofacial Surgery **35**, 708, 2006.
57. Cray Jr, J., Henderson, S.E., Smith, D.M., Kinsella Jr, C.R., Bykowski, M., Cooper, G.M., Almarza, A.J., andLosee, J.E. BMP-2–Regenerated Calvarial Bone: A Biomechanical Appraisal in a Large Animal Model. Annals of plastic surgery **73**, 591, 2014.
58. Smucker, J.D., Petersen, E.B., andFredericks, D.C. Assessment of MASTERGRAFT PUTTY as a graft extender in a rabbit posterolateral fusion model. Spine **37**, 1017, 2012.
59. Lee, J.H., Chang, B.-S., Jeung, U.-O., Park, K.-W., Kim, M.-S., andLee, C.-K. The First Clinical Trial of Beta-Calcium Pyrophosphate as a Novel Bone Graft Extender in Instrumented Posterolateral Lumbar Fusion. Clin Orthop Surg **3**, 238, 2011.
60. Moreira-Gonzalez, A., Lobocki, C., Barakat, K., Andrus, L., Bradford, M., Gilsdorf, M., andJackson, I.T. Evaluation of 45S5 Bioactive Glass Combined as a Bone Substitute in the Reconstruction of Critical Size Calvarial Defects in Rabbits. Journal of Craniofacial Surgery **16**, 63, 2005.
61. Conejero, J.A., Lee, J.A., andAscherman, J.A. Cranial defect reconstruction in an experimental model using different mixtures of bioglass and autologous bone. Journal of Craniofacial Surgery **18**, 1290, 2007.
62. Pina, S., Torres, P., andFerreira, J. Injectability of brushite-forming Mg-substituted and Sr-substituted α-TCP bone cements. Journal of Materials Science: Materials in Medicine **21**, 431, 2010.
63. Bohner, M., andBaroud, G. Injectability of calcium phosphate pastes. Biomaterials **26**, 1553, 2005.
64. Mathieu, L.M., Mueller, T.L., Bourban, P.E., Pioletti, D.P., Muller, R., andManson, J.A. Architecture and properties of anisotropic polymer composite scaffolds for bone tissue engineering. Biomaterials **27**, 905, 2006.
65. Ramay, H.R.R., andZhang, M. Biphasic calcium phosphate nanocomposite porous scaffolds for load-bearing bone tissue engineering. Biomaterials **25**, 5171, 2004.
66. Pattin, C.A., Caler, W.E., andCarter, D.R. Cyclic mechanical property degradation during fatigue loading of cortical bone. Journal of Biomechanics **29**, 69, 1996.
67. Ding, S.-J., Wei, C.-K., andLai, M.-H. Bio-inspired calcium silicate–gelatin bone grafts for load-bearing applications. Journal of Materials Chemistry **21**, 12793, 2011.
68. Lewis, G. Properties of acrylic bone cement: State of the art review. Journal of Biomedical Materials Research **38**, 155, 1997.
69. Karageorgiou, V., andKaplan, D. Porosity of 3D biomaterial scaffolds and osteogenesis. Biomaterials **26**, 5474, 2005.

70. Halacheva, S.S., Adlam, D.J., Hendow, E.K., Freemont, T.J., Hoyland, J., andSaunders, B.R. Injectable Biocompatible and Biodegradable pH-Responsive Hollow Particle Gels Containing Poly(acrylic acid): The Effect of Copolymer Composition on Gel Properties. Biomacromolecules **15**, 1814, 2014.
71. Boger, A., Bohner, M., Heini, P., Verrier, S., andSchneider, E. Properties of an injectable low modulus PMMA bone cement for osteoporotic bone. Journal of Biomedical Materials Research Part B: Applied Biomaterials **86B**, 474, 2008.
72. Rodriguez, L.C., Chari, J., Aghyarian, S., Gindri, I.M., Kosmopoulos, V., andRodrigues, D.C. Preparation and characterization of injectable brushite filled-poly (methyl methacrylate) bone cement. Materials **7**, 6779, 2014.
73. Dumas, J.E., Prieto, E.M., Zienkiewicz, K.J., Guda, T., Wenke, J.C., Bible, J., Holt, G.E., andGuelcher, S.A. Balancing the rates of new bone formation and polymer degradation enhances healing of weight-bearing allograft/polyurethane composites in rabbit femoral defects. Tissue Eng Part A **20**, 115, 2014.
74. Prieto, E.M., Talley, A.D., Gould, N.R., Zienkiewicz, K.J., Drapeau, S.J., Kalpakci, K.N., andGuelcher, S.A. Effects of particle size and porosity on in vivo remodeling of settable allograft bone/polymer composites. Journal of Biomedical Materials Research Part B: Applied Biomaterials, n/a, 2015.
75. Mundy, G. Regulatory mechanisms of osteoclast differentiation and function. Journal of Bone and Mineral Metabolism **14**, 59, 1996.
76. Boyle, W.J., Simonet, W.S., andLacey, D.L. Osteoclast differentiation and activation. Nature **423**, 337, 2003.
77. Jensen, E.D., Pham, L., Billington, C.J., Jr., Espe, K., Carlson, A.E., Westendorf, J.J., Petryk, A., Gopalakrishnan, R., andMansky, K. Bone morphogenic protein 2 directly enhances differentiation of murine osteoclast precursors. J Cell Biochem **109**, 672, 2010.
78. Schneider, J.G., Amend, S.R., andWeilbaecher, K.N. Integrins and bone metastasis: integrating tumor cell and stromal cell interactions. Bone **48**, 54, 2011.
79. Wilson, S.R., Peters, C., Saftig, P., andBromme, D. Cathepsin K activity-dependent regulation of osteoclast actin ring formation and bone resorption. J Biol Chem **284**, 2584, 2009.
80. Henriksen, K., Karsdal, M.A., andMartin, T.J. Osteoclast-derived coupling factors in bone remodeling. Calcif Tissue Int **94**, 88, 2014.
81. Williams, D.F. On the mechanisms of biocompatibility. Biomaterials **29**, 2941, 2008.
82. Sabir, M.I., Xu, X., andLi, L. A review on biodegradable polymeric materials for bone tissue engineering applications. Journal of Materials Science **44**, 5713, 2009.
83. Gorna, K., andGogolewski, S. Preparation, degradation, and calcification of biodegradable polyurethane foams for bone graft substitutes. Journal of Biomedical Materials Research Part A **67A**, 813, 2003.
84. Hafeman, A.E., Zienkiewicz, K.J., Zachman, A.L., Sung, H.J., Nanney, L.B., Davidson, J.M., andGuelcher, S.A. Characterization of the degradation mechanisms of lysine-derived aliphatic poly(ester urethane) scaffolds. Biomaterials **32**, 419, 2011.
85. Schubert, M.A., Wiggins, M.J., Anderson, J.M., andHiltner, A. Role of oxygen in biodegradation of poly(etherurethane urea) elastomers. J Biomed Mater Res **34**, 519, 1997.
86. Ambard, A.J., andMueninghoff, L. Calcium Phosphate Cement: Review of Mechanical and Biological Properties. Journal of Prosthodontics **15**, 321, 2006.

87. Yamada, S., Heymann, D., Bouler, J.M., andDaculsi, G. Osteoclastic resorption of calcium phosphate ceramics with different hydroxyapatite/β-tricalcium phosphate ratios. Biomaterials **18**, 1037, 1997.
88. Wenisch, S., Stahl, J.P., Horas, U., Heiss, C., Kilian, O., Trinkaus, K., Hild, A., andSchnettler, R. In vivo mechanisms of hydroxyapatite ceramic degradation by osteoclasts: Fine structural microscopy. Journal of Biomedical Materials Research Part A **67A**, 713, 2003.
89. Rameshbabu, N., andRao, K.P. Microwave synthesis, characterization and in-vitro evaluation of nanostructured biphasic calcium phosphates. Current Applied Physics **9**, S29, 2009.
90. Monchau, F., Lefèvre, A., Descamps, M., Belquin-myrdycz, A., Laffargue, P., andHildebrand, H.F. In vitro studies of human and rat osteoclast activity on hydroxyapatite, β-tricalcium phosphate, calcium carbonate. Biomolecular Engineering **19**, 143, 2002.
91. Großardt, C., Ewald, A., Grover, L.M., Barralet, J.E., andGbureck, U. Passive and active in vitro resorption of calcium and magnesium phosphate cements by osteoclastic cells. Tissue Engineering Part A **16**, 3687, 2010.
92. Sun, J.-Y., Yang, Y.-S., Zhong, J., andGreenspan, D.C. The effect of the ionic products of Bioglass® dissolution on human osteoblasts growth cycle in vitro. Journal of Tissue Engineering and Regenerative Medicine **1**, 281, 2007.
93. Jones, J.R., Sepulveda, P., andHench, L.L. Dose-dependent behavior of bioactive glass dissolution. Journal of Biomedical Materials Research **58**, 720, 2001.
94. Santos, F.A., Pochapski, M.T., Martins, M.C., Zenóbio, E.G., Spolidoro, L.C., andMarcantonio Jr, E. Comparison of Biomaterial Implants in the Dental Socket: Histological Analysis in Dogs. Clinical Implant Dentistry and Related Research **12**, 18, 2010.
95. Puumanen, K., Kellomäki, M., Ritsilä, V., Böhling, T., Törmälä, P., Waris, T., andAshammakhi, N. A novel bioabsorbable composite membrane of Polyactive® 70/30 and bioactive glass number 13-93 in repair of experimental maxillary alveolar cleft defects. Journal of Biomedical Materials Research Part B: Applied Biomaterials **75B**, 25, 2005.
96. Midha, S., van den Bergh, W., Kim, T.B., Lee, P.D., Jones, J.R., andMitchell, C.A. Bioactive Glass Foam Scaffolds are Remodelled by Osteoclasts and Support the Formation of Mineralized Matrix and Vascular Networks In Vitro. Advanced Healthcare Materials **2**, 490, 2013.
97. Gentleman, E., Fredholm, Y.C., Jell, G., Lotfibakhshaiesh, N., O'Donnell, M.D., Hill, R.G., andStevens, M.M. The effects of strontium-substituted bioactive glasses on osteoblasts and osteoclasts in vitro. Biomaterials **31**, 3949, 2010.
98. Hoppe, A., Güldal, N.S., andBoccaccini, A.R. A review of the biological response to ionic dissolution products from bioactive glasses and glass-ceramics. Biomaterials **32**, 2757, 2011.
99. Boden, S.D., Schimandle, J.H., andHutton, W.C. An Experimental Lumbar Intertransverse Process Spinal Fusion Model: Radiographic, Histologic, and Biomechanical Healing Characteristics. Spine **20**, 412, 1995.
100. Pearce, A.I., Richards, R.G., Milz, S., Schneider, E., andPearce, S.G. Animal models for implant biomaterial research in bone: a review. Eur Cell Mater **13**, 1, 2007.
101. Muschler, G.F., Raut, V.P., Patterson, T.E., Wenke, J.C., andHollinger, J.O. The design and use of animal models for translational research in bone tissue engineering and regenerative medicine. Tissue Engineering Part B: Reviews **16**, 123, 2010.
102. Chu, C.R., Szczodry, M., andBruno, S. Animal models for cartilage regeneration and repair. Tissue Engineering Part B: Reviews **16**, 105, 2010.

103. Luvizuto, E.R., Tangl, S., Zanoni, G., Okamoto, T., Sonoda, C.K., Gruber, R., andOkamoto, R. The effect of BMP-2 on the osteoconductive properties of β-tricalcium phosphate in rat calvaria defects. Biomaterials **32**, 3855, 2011.
104. Einhorn, T.A., Lane, J.M., Burstein, A.H., Kopman, C.R., andVigorita, V.J. The healing of segmental bone defects induced by demineralized bone matrix. A radiographic and biomechanical study. J Bone Joint Surg Am **66**, 274, 1984.
105. Einhorn, T.A. Clinically applied models of bone regeneration in tissue engineering research. Clinical orthopaedics and related research **367**, S59, 1999.
106. An, Y.H., Woolf, S.K., andFriedman, R.J. Pre-clinical in vivo evaluation of orthopaedic bioabsorbable devices. Biomaterials **21**, 2635, 2000.
107. Martini, L., Fini, M., Giavaresi, G., andGiardino, R. Sheep model in orthopedic research: a literature review. Comparative medicine **51**, 292, 2001.
108. SCHMITZ, J.P., andHollinger, J.O. The critical size defect as an experimental model for craniomandibulofacial nonunions. Clinical orthopaedics and related research **205**, 299, 1986.
109. Reichert, J.C., Saifzadeh, S., Wullschleger, M.E., Epari, D.R., Schütz, M.A., Duda, G.N., Schell, H., van Griensven, M., Redl, H., andHutmacher, D.W. The challenge of establishing preclinical models for segmental bone defect research. Biomaterials **30**, 2149, 2009.
110. Wang, S., Liu, Y., Fang, D., andShi, S. The miniature pig: a useful large animal model for dental and orofacial research. Oral Diseases **13**, 530, 2007.
111. Ma, J.L., Pan, J.L., Tan, B.S., andCui, F.Z. Determination of critical size defect of minipig mandible. J Tissue Eng Regen Med **3**, 615, 2009.
112. Emerton, K., Drapeau, S., Prasad, H., Rohrer, M., Roffe, P., Hopper, K., Schoolfield, J., Jones, A., andCochran, D. Regeneration of periodontal tissues in non-human primates with rhGDF-5 and beta-tricalcium phosphate. Journal of dental research **90**, 1416, 2011.
113. Ripamonti, U., Richter, P.W., Nilen, R.W.N., andRenton, L. The induction of bone formation by smart biphasic hydroxyapatite tricalcium phosphate biomimetic matrices in the non-human primate Papio ursinus. Journal of Cellular and Molecular Medicine **12**, 2609, 2008.
114. Wikesjö, U.M., Huang, Y.H., Xiropaidis, A.V., Sorensen, R.G., Rohrer, M.D., Prasad, H.S., Wozney, J.M., andHall, J. Bone formation at recombinant human bone morphogenetic protein-2-coated titanium implants in the posterior maxilla (Type IV bone) in non-human primates. Journal of clinical periodontology **35**, 992, 2008.
115. Wikesjö, U.M., Qahash, M., Polimeni, G., Susin, C., Shanaman, R.H., Rohrer, M.D., Wozney, J.M., andHall, J. Alveolar ridge augmentation using implants coated with recombinant human bone morphogenetic protein-2: histologic observations. Journal of clinical periodontology **35**, 1001, 2008.
116. Barnes, B., Boden, S.D., Louis-Ugbo, J., Tomak, P.R., Park, J.-S., Park, M.-S., andMinamide, A. Lower Dose of rhBMP-2 Achieves Spine Fusion When Combined With an Osteoconductive Bulking Agent in Non-human Primates. Spine **30**, 1127, 2005.
117. Seeherman, H., Li, R., Bouxsein, M., Kim, H., Li, X.J., Smith-Adaline, E.A., Aiolova, M., andWozney, J.M. rhBMP-2/calcium phosphate matrix accelerates osteotomy-site healing in a nonhuman primate model at multiple treatment times and concentrations. The Journal of Bone & Joint Surgery **88**, 144, 2006.
118. Boden, S.D., Moskovitz, P.A., Morone, M.A., andToribitake, Y. Video-Assisted Lateral Intertransverse Process Arthrodesis: Validation of a New Minimally Invasive Lumbar Spinal Fusion Technique in the Rabbit and Nonhuman Primate (Rhesus) Models. Spine **21**, 2689, 1996.

119. Cook, S.D., Wolfe, M.W., Salkeld, S.L., andRueger, D.C. Effect of recombinant human osteogenic protein-1 on healing of segmental defects in non-human primates. J Bone Joint Surg Am **77**, 734, 1995.
120. Hedberg, E.L., Kroese-Deutman, H.C., Shih, C.K., Lemoine, J.J., Liebschner, M.A., Miller, M.J., Yasko, A.W., Crowther, R.S., Carney, D.H., andMikos, A.G. Methods: a comparative analysis of radiography, microcomputed tomography, and histology for bone tissue engineering. Tissue Engineering **11**, 1356, 2005.
121. Meijer, G.J., de Bruijn, J.D., Koole, R., andvan Blitterswijk, C.A. Cell-based bone tissue engineering. PLoS Med **4**, e9, 2007.
122. Gündüz, E., Rodríguez-Torres, C., Gahleitner, A., Heissenberger, G., andBantleon, H.-P. Bone regeneration by bodily tooth movement: dental computed tomography examination of a patient. American Journal of Orthodontics and Dentofacial Orthopedics **125**, 100, 2004.
123. Harrysson, O.L., Hosni, Y.A., andNayfeh, J.F. Custom-designed orthopedic implants evaluated using finite element analysis of patient-specific computed tomography data: femoral-component case study. BMC Musculoskeletal Disorders **8**, 1, 2007.
124. Mengel, R., Kruse, B., andFlores-de-Jacoby, L. Digital Volume Tomography in the Diagnosis of Peri-Implant Defects: An In Vitro Study on Native Pig Mandibles. Journal of Periodontology **77**, 1234, 2006.
125. Feldkamp, L.A., Goldstein, S.A., Parfitt, M.A., Jesion, G., andKleerekoper, M. The direct examination of three-dimensional bone architecture in vitro by computed tomography. Journal of bone and mineral research **4**, 3, 1989.
126. van Lenthe, G.H., Hagenmüller, H., Bohner, M., Hollister, S.J., Meinel, L., andMüller, R. Nondestructive micro-computed tomography for biological imaging and quantification of scaffold–bone interaction in vivo. Biomaterials **28**, 2479, 2007.
127. Bouxsein, M.L., Boyd, S.K., Christiansen, B.A., Guldberg, R.E., Jepsen, K.J., andMuller, R. Guidelines for assessment of bone microstructure in rodents using micro-computed tomography. J Bone Miner Res **25**, 1468, 2010.
128. Komlev, V., Peyrin, F., Mastrogiacomo, M., Cedola, A., Papadimitropoulos, A., Rustichelli, F., andCancedda, R. Kinetics of in vivo bone deposition by bone marrow stromal cells into porous calcium phosphate scaffolds: an X-ray computed microtomography study. Tissue engineering **12**, 3449, 2006.
129. Rentsch, C., Schneiders, W., Manthey, S., Rentsch, B., andRammelt, S. Comprehensive histological evaluation of bone implants. Biomatter **4**, e27993, 2014.

CHAPTER III

REMODELING OF INJECTABLE, LOW-VISCOSITY POLYMER/CERAMIC BONE GRAFTS IN A SHEEP FEMORAL DEFECT MODEL

Introduction

Common treatment options for grafting metaphyseal bone defects include allogeneic bone and synthetic bone void fillers. Tissue engineering research has investigated alternatives to allograft that meet the performance requirements for bone void fillers (BVFs): osteoconductivity, controlled degradation to non-toxic degradation byproducts, suitable handling properties, and porosity (1-3). Ceramics are used to treat bone defects due to their osteoconductivity and/or bioactivity. Synthetic hydroxyapatite (HA) and β-tricalcium phosphate (β-TCP) have been commercially available since the 1980s and are widely used in dental and orthopaedic applications (4). Ceramic/polymer composites combine the osteoconductivity of ceramics with the ductility of polymers, resulting in a graft that meets many of the targeted properties for a BVF (5, 6). Additionally, the relative degradation rates of the ceramic and polymer phases can be tuned balance the rates of cellular infiltration, new bone formation, and graft resorption (7). However, the relative contributions of the polymer and ceramic degradation kinetics to bone healing are not well understood (5, 8).

Biodegradable polyurethane (PUR) composites have been tested in a variety of bone grafting applications (9-11). Lysine-derived PUR composites have non-cytotoxic degradation products, generate minimal inflammatory response, and promote cellular infiltration and new bone formation in rats (12, 13), rabbits (14, 15), and canines (16). These composites can be injected *in situ* to fill a wide variety of bone defect shapes and sizes and set within clinically relevant time frames (17). Allograft/PUR composites remodel by creeping substitution, characterized by osteoclast-mediated resorption of allograft particles and consequent deposition of mineralized matrix by osteoblasts (14, 18). Thus, remodeling progresses from the host bone-graft interface toward the interior of the defect over time. Allograft particles are resorbed within 6 – 12 weeks *in vivo* (15), while ceramics such as β-TCP and HA can persist for much longer (19, 20). Bone healing is optimized when remodeling is balanced (i.e., the rate of degradation of the graft matches that of new bone deposition (18)). Since lysine-derived polyurethanes undergo cell-mediated degradation, a more persistent ceramic phase may be more desirable for balanced remodeling of bone defects.

In this study, we investigated the remodeling of low viscosity (LV) PUR composites in a sheep femoral condyle plug defect model. Two types of LV composites were investigated: (1) LV/ceramic and (2) LV/allograft. The ceramic particles comprised Mastergraft® (85% β-TCP, 15% HA) Mini-Granules (Medtronic), an FDA-approved bone void filler that supports balanced remodeling and supports new bone formation in preclinical models of bone regeneration (21, 22). The loading of ceramic (CM) or allograft (A) particles in the LV composites was 45 wt%, which was the highest concentration that could be added to maintain flowability. A ceramic control group received only ceramic particles. After injection, LV composites expanded to yield foams with ~50% porosity, resulting in dilution of the CM or A particles in the final graft to ~25 wt% (~15 vol%). LV/A composites remodeled to form new bone in a rabbit femoral condyle plug defect model (14, 15, 23), but their ability to promote new bone formation in a larger and more stringent model in sheep has not been assessed. Since Mastergraft® ceramic particles remodel more slowly than allograft bone, we hypothesized that LV/CM composites would better support new bone formation and remodeling at later time points in a large animal preclinical model of bone regeneration compared to LV/A composites. We further hypothesized that healing of LV/CM composites, which have the advantageous handling properties of injectability and flowability, would heal comparably to the CM control, which was evaluated for up to 2 years to study its long-term degradation properties.

Experimental

Materials. Lysine triisocyanate (LTI)-polyethylene glycol (PEG) prepolymer (LTI-PEG, 21.7% NCO) was purchased from Ricerca Biosciences LLC (Painesville, OH). Glycerol, stannous octoate, and ε-caprolactone were purchased from Sigma-Aldrich (St. Louis, MO). Glycolide and DL-lactide were supplied by Polysciences (Warrington, PA). Triethylene diamine (TEDA) and dipropylene glycol (DPG) were purchased from Sigma Aldrich and mixed to obtain a 10% (w/w) solution of TEDA in dry DPG. MASTERGRAFT® Mini Granules (ceramic, CM) and sheep allograft bone particles (100-500 µm) were received from Medtronic, Inc. (Minneapolis, MN). To prepare oxidative degradation media, $CoCl_2$ and 30 wt% H_2O_2 were purchased from Sigma-Aldrich (St Louis, MO) and Fisher Scientific (Pittsburgh, PA), respectively.

Synthesis of polyester triol. The polyester triol was synthesized as previously described (24, 25). Briefly, a glycerol starter was mixed with ε-caprolactone, glycolide, and DL-lactide monomers under dry argon at 140 °C for 40 h. Afterwards, the polyester triol was cooled, washed with hexane, and dried under vacuum at 80 °C. The backbone of the polyester comprised 70% ε-caprolactone, 20% glycolide, and 10% DL-lactide, and the molecular weight was 450 g mol^{-1}.

Fabrication of Low-viscosity (LV) Bone Grafts. Sheep allograft (A) particles were lyophilized prior to use to remove excess water. The components of the LV grafts were mixed in a two-step method. In the first step, the polyester triol, particles (either 45 wt% CM or 45 wt% A), and TEDA (1.1 pphp) were added to a 10-mL cup and mixed by hand for 30 s. The LTI-PEG prepolymer was added to the cup and mixed by hand for 60 s. The index (ratio of isocyanate:hydroxyl equivalents x 100) was 115. For material characterization, the reactive mixture was mixed with 3 pphp of DI water (to simulate *in vivo* curing in the presence of moisture), loaded into a straight bore syringe, and injected into a 6-mm vial. These samples were allowed to cure for 24 h prior to cutting.

Composite Characterization. LV/A and LV/CM composites were cut into sections, mounted onto a scanning electron microscopy (SEM) pin stub mount, and sputter-coated for 40 s using a Cressington Q108 sputter coater, which deposited gold at a 30 mA current. A Hitachi S-4200 SEM was used to acquire images at a voltage of 1 kV.

Cylindrical samples (6 mm x 12 mm) were prepared with porosities of approximately 50% (measured gravimetrically) to represent *in vivo* foaming conditions. Samples were submerged in PBS at 37°C for 24 h prior to mechanical testing. Compression testing was performed using an MTS 898 Bionix system (Eden Prairie, MN) with a 1-kN load cell. The samples were preloaded to 3 N and compressed at a constant rate of 25 mm/min. The initial cross-sectional area of the cylinders was used to calculate compressive stress. The compressive modulus was calculated as the slope of the initial linear portion of the stress-strain curve. Porosity and compression data are presented as mean ± standard deviation of triplicate samples.

Polymer Degradation. PUR scaffolds without ceramic or allograft were prepared following the above mixing method. Triplicate samples (~50 mg) were cut from the foams and incubated at 37°C in either oxidative media or PBS. The PBS simulates the conditions for hydrolytic degradation. The oxidative media comprised 0.1 M $CoCl_2$ in 2 wt% H_2O_2 (2%OM) or 20 wt% H_2O_2 (20%OM), which recapitulates the *in vivo* microenvironment between adherent macrophages and the surface of the biomaterial (26, 27). The oxidative media was replaced every 3-4 days. At desired time points, samples were removed, rinsed 2x with DI water, incubated in DI water at 37°C for 1 h, rinsed 2x with DI water, and dried under vacuum at 40°C overnight prior to weighing.

Sheep Femoral Plug Study. Eighteen skeletally mature, non-pregnant female sheep (54 – 88 kg) were used in this study. All surgical and care procedures were carried out at IBEX Preclinical Research Inc. (Logan, UT) under aseptic conditions according to the approved IACUC protocol. Treatment groups are listed in Table 3.1. The individual components of the LV grafts were gamma-irradiated using a dose of 25 kGY. A semicircular incision was created in the periosteum and the periosteal flap was removed. Bilateral defects measuring 11 x 18 mm were drilled through a Kirschner wire guide and reamer in the distal aspect of the lateral femoral condyle of each sheep. Defects were filled with LV grafts, injected via a straight bore syringe, or CM control (C) grafts. The control group consisted of CM granules alone (approximately 2 cc). The defects receiving LV composites were filled approximately 40% to account for composite foaming and expansion *in situ*. Specimens were harvested at 4 months, 12 months, 15 months, or 2 years. One sheep from the 12-month group was sacrificed early due to complications not associated with the grafts (these data were not included in the analysis).

Table 3.1. Treatment groups evaluated in the sheep femoral plug defect

Treatment Group	**Particles**	**Particle diameter (μm)**	**% Matrix**	**n 16 weeks**	**n 12-15 months**	**n 24 months**
C	Mastergraft	500-1500	100	4	3*	4
LV/CM	Mastergraft	500-1500	45	4	7	1
LV/A	Allograft	100-500	45	4	6	2

*****One sheep from the 12-15 month group was sacrificed early due to complications not associated with the grafts.

Micro-computed tomography (μCT) analysis. A μCT50 (SCANO Medical, Basserdorf Switzerland) was used to acquire scans of the extracted mandibles in formalin at 70 kVp energy, 200 μA source current, 1000 projections per rotation, 800 ms integration time, and an isotropic voxel size of 24.2 μm. Axial images were reconstituted using manufacturer provided software. Attenuation values were converted to tissue mineral density (TMD) through calibration with hydroxyapatite (HA) phantoms with densities of 0 to 780 mg HA cm^{-3} (calibrations checked weekly). Using the cortical borders of the defect for alignment, the reconstructed image stack was oriented with the depth of the defect parallel to the z-axis. Radial analysis of morphometric parameters was conducted from the core of the implant to the interface with host bone. Four concentric annular volumes of interest with thickness of 1.83 mm and a length of 14 mm (from the outer cortical surface of the femur) were defined for each sample. The three inner cylindrical sections covered the defect volume, while the outer region provided information about the interface with host bone. Ossified tissue was segmented from soft tissue using the lower and upper thresholds of 240 mg $HAcm^{-3}$ and 1000 mg $HAcm^{-3}$ respectively, with a Gaussian noise filter settings of sigma 0.7 and support 2. Morphometric parameters within the annular regions were calculated, grouped by treatment and time point, and plotted versus the mean radial distance (R_m) from the core of the defect ($R_m=(R_o+R_i)/2$, where R_o and R_i correspond to the outer and inner radius of each region, respectively) (15, 18). Bone volume/total volume (BV/TV), trabecular number (Tb.N), trabecular thickness (Tb.Th), and trabecular separation (Tb.Sp) within the regions of interest were computed using SCANCO's Medical microCT systems software as described previously (15, 18). A host bone control was run using the same parameters and analyzed for comparison to the graft groups (28). Additional scans were run on LV/A and LV/CM composites (prepared as above) and packed ceramic particles (to replicate group C) to provide initial morphometric parameter values for all test groups.

Histology. After fixation in formalin the defects were cut approximately in half with one side dehydrated in a graded series of ethanol and embedded in methyl methacrylate. One pair of longitudinal ground sections were taken from approximately the center of each sample. One section was stained with Stevenel's blue/van Gieson and the other was stained with hematoxylin and eosin. Sections were qualitatively evaluated for residual implant material, new bone formation, and cellular response at high and low magnifications.

Histomorphometry. For quantitative analysis, Stevenel's blue/van Gieson stained sections were imaged at 2x and 20x magnification with an Olympus camera (DP71) using an Olympus BX60 microscope. Residual matrix particles (A or CM), residual PUR, and newly formed bone were quantified for each sample (two data points per slide) in an area of interest (6 mm x 14.6 mm) in the center of each defect using color analysis on Metamorph software (Version 7.0.1, Waltham, MA). The area of interest was divided into 6 regions measuring 1.83 mm wide and corresponding to the volumes of interest measured by µCT as described previously (28).

Statistical analysis. Porosity, modulus, and yield strength statistics were tested via a Student's t-test between the LV/CM and LV/A groups. A two-way ANOVA was run in GraphPad on µCT radial analysis and histomorphometry data at 4 months to identify statistically significant differences between groups as a function of radial distance and particle composition (allograft or ceramic). Statistical significance was considered for $p < 0.05$.

Results

Composite characterization. Physical and mechanical properties of LV grafts are summarized in Table 3.2. Initial porosities were similar for LV/A (52.6%) and LV/CM composites (53.2%). Representative SEM images (Figure 3.1) illustrate the interconnected pore structure and high porosity of the composites. The compressive modulus and yield strength (Table 3.2) were significantly higher for LV/A compared to LV/CM.

Table 3.2. Physical and mechanical properties of LV composites.

Treatment Group	Porosity (%)	Bulk Modulus (MPa)	Yield Strength (MPa)
LV/CM	52.4 ± 0.3	1.45 ± 0.29	0.320 ± 0.047
LV/A	48.0 ± 3.0	2.80 ± 0.18[a]	0.455 ± 0.050[a]

[a]Significantly higher at $p < 0.05$

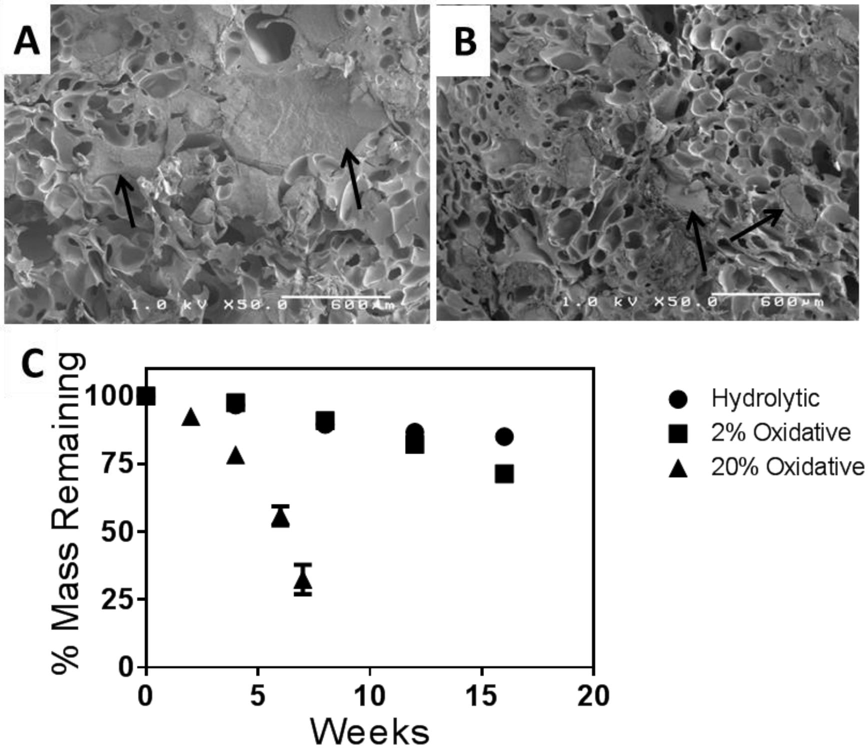

Figure 3.1. SEM images of composite grafts (A) LV/CM and (B) LV/A. Black arrows point to matrix particles present within the composites. The scale bar represents 600 µm. (C) *In vitro* degradation of PUR scaffolds under hydrolytic, 2% oxidative media, and 20% oxidative media conditions.

Polymer Degradation. In vitro hydrolytic and oxidative degradation (in 2% H_2O_2 or 20% H_2O_2) of the polyurethane component is displayed in Figure 3.1. Samples degraded within 7 weeks in 20%OM, losing 22% of sample mass within the first 4 weeks. As expected, samples in 2%OM degraded more slowly than those in 20% OM (29% mass loss after 16 weeks). Polymer degradation was the slowest under hydrolytic conditions with samples only losing 15% mass after 16 weeks.

Preclinical study. Defects were created bilaterally in the femoral condoyle of the sheep (Figure 3.2A). For the LV graft delivery, the composites were mixed and loaded into a straight-bore syringe. The syringe was inserted into the defect site (Figure 3.2B) to deliver the grafts (Figure 3.2C). Following the foaming reaction of the PUR, the graft material expanded outside of the limits of the defect (Figure 3.2D). The excess graft was removed to leave the scaffold flush with the host bone (Figure 3.2E). For the control defects, CM particles were delivered via a straight bore syringe (Figure 3.2F) and packed into the defect.

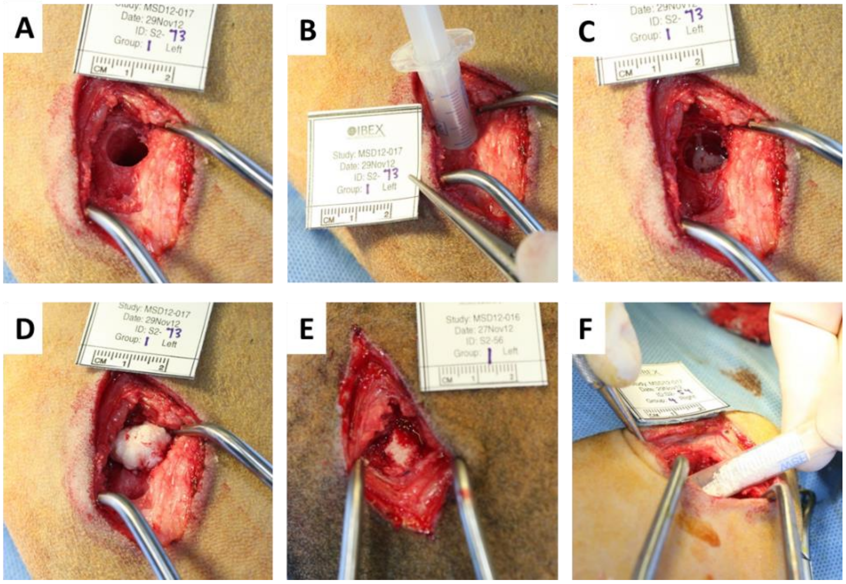

Figure 3.2. Surgical photographs of (A) defect creation, (B) injection of LV/CM graft, (C) LV/CM graft immediately following delivery, (D) LV/CM graft following foaming reaction, (E) LV/CM graft once trimmed to match the host bone, and (F) delivery of CM control group.

μCT morphometric analysis. Figure 3.3 displays μCT images of the best and worst performing samples in each treatment group at the different time points. Defects treated with the CM control showed residual ceramic particles, visible as bright white particles in the images, at 4 months. The amount of residual ceramic decreased at the 1- and 2-year time points as the composites remodeled. All defects showed bridging of the defect with new cortex by 12 months with minimal depression (Figure 3.4). LV/CM-treated defects exhibited a similar pattern of remodeling compared to the ceramic control. However, healing was more variable, with some groups showing evidence of voids or depression of the cortex, which was predominantly apparent at 12-15 months (Figure 3.5). LV/A composites resorbed faster than the ceramic groups, as evidenced by less residual allograft at 4 and 12 – 15 months. Healing of the LV/A composites was also variable (Figure 3.6); some defects had completely bridged with new bone at 12 – 15 months, while others revealed evidence of voids and depression of the cortex.

Morphometric parameters evaluated by μCT were plotted as a function of the mean radial distance from the core of the defect to monitor remodeling (Figure 3.7). At 4 months, BV/TV (which includes both new bone and residual ceramic or allograft particles) was highest in the center of the defect and decreased radially outward toward the host bone interface for the control group. LV composites showed the opposite trend, with the highest BV/TV near the host bone interface due to their lower mineral content compared to the control. Within the defect area, BV/TV for the LV/A and LV/CM groups were significantly different from the control. Similar trends were seen with Tb.N and Tb.Th parameters. For Tb.Sp, all groups had values close to that of the host bone. Radial trends were also evident at 12-15 months, as remodeling was not complete at this time.

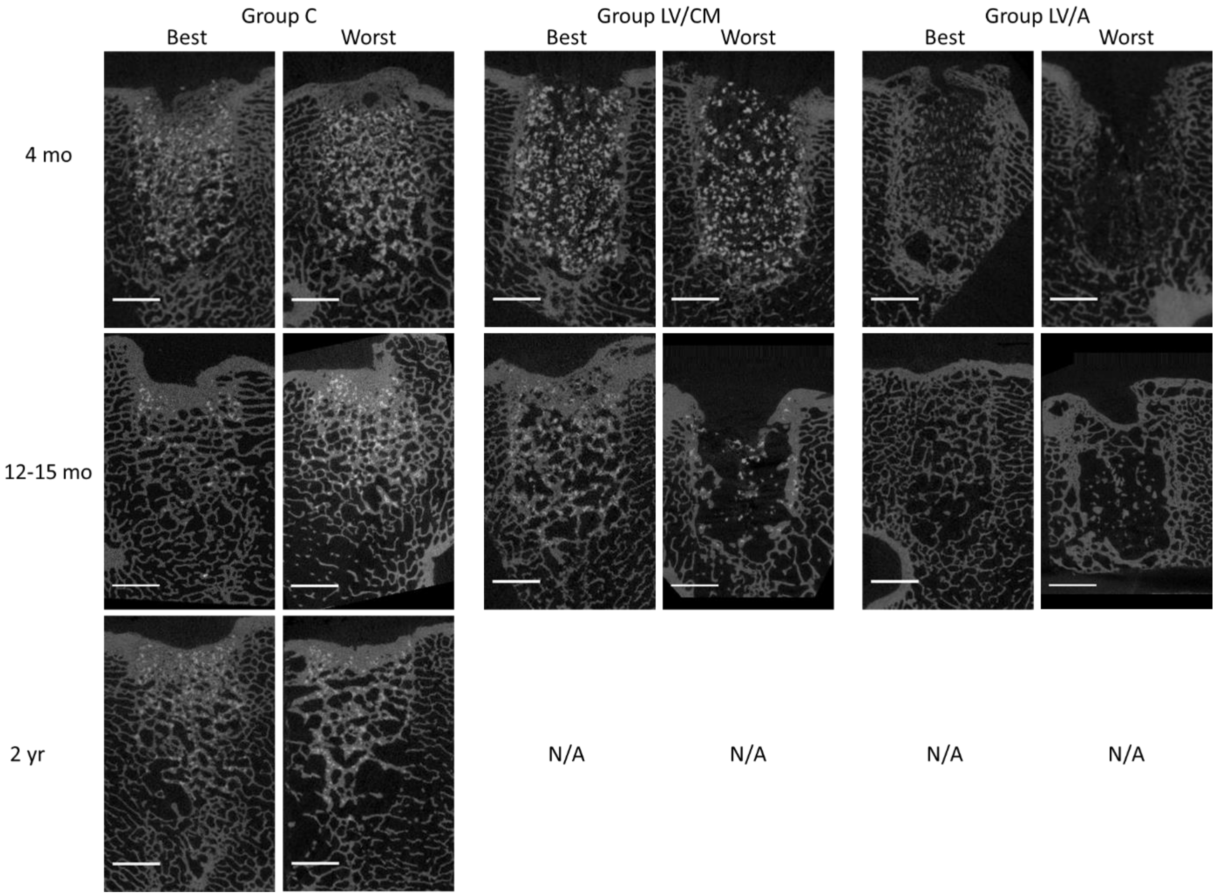

Figure 3.3. 2D µCT images of sheep femoral plug defects showing the best and worst performing grafts in each group. The scale bar represents 5 mm.

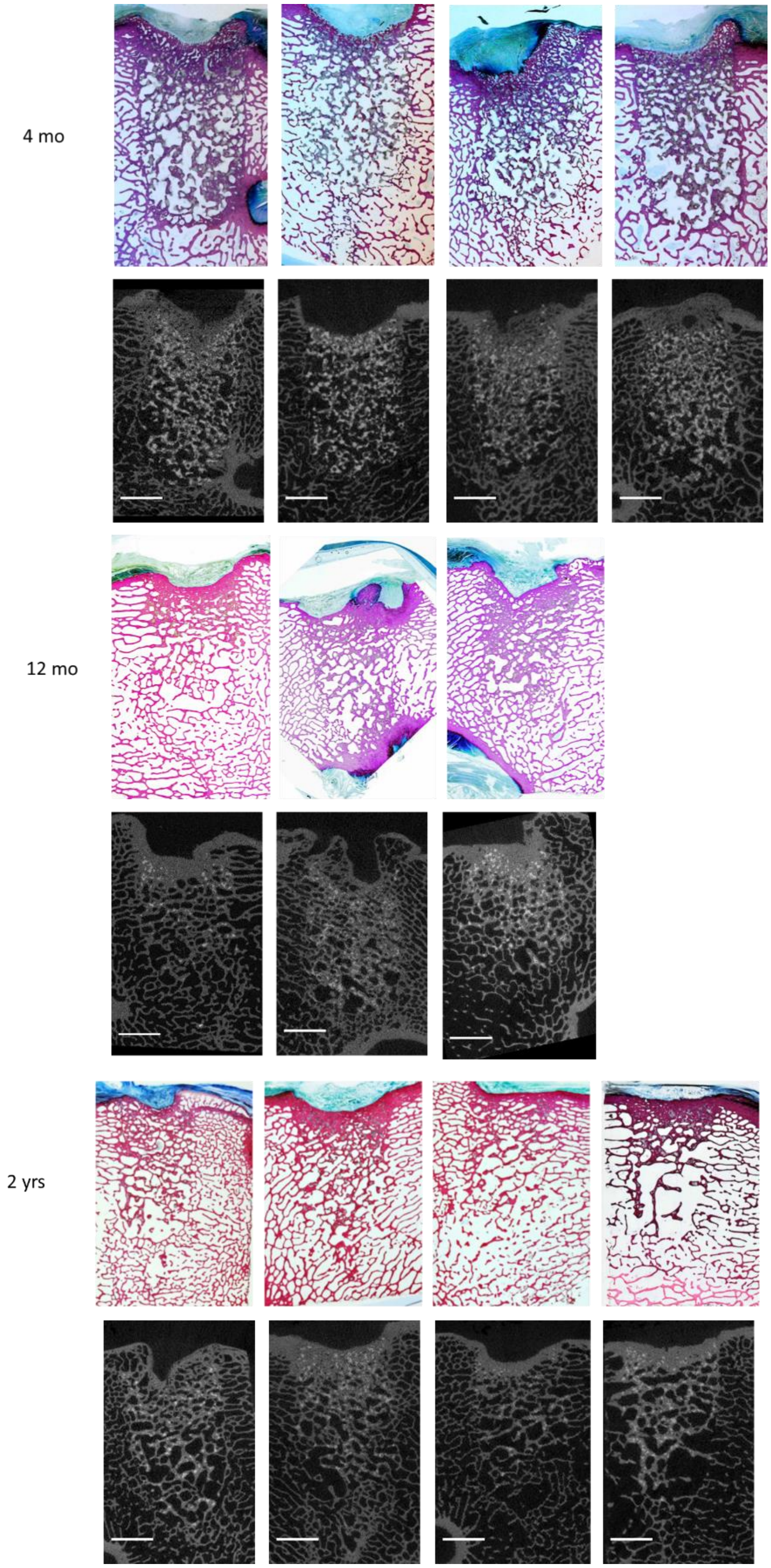

Figure 3.4. 2D μCT images (scale bar represents 5 mm) and Stevenson's blue/van Gieson stained histological sections (1x) for all samples in group C at 4 month, 12 month, and 2 year time points.

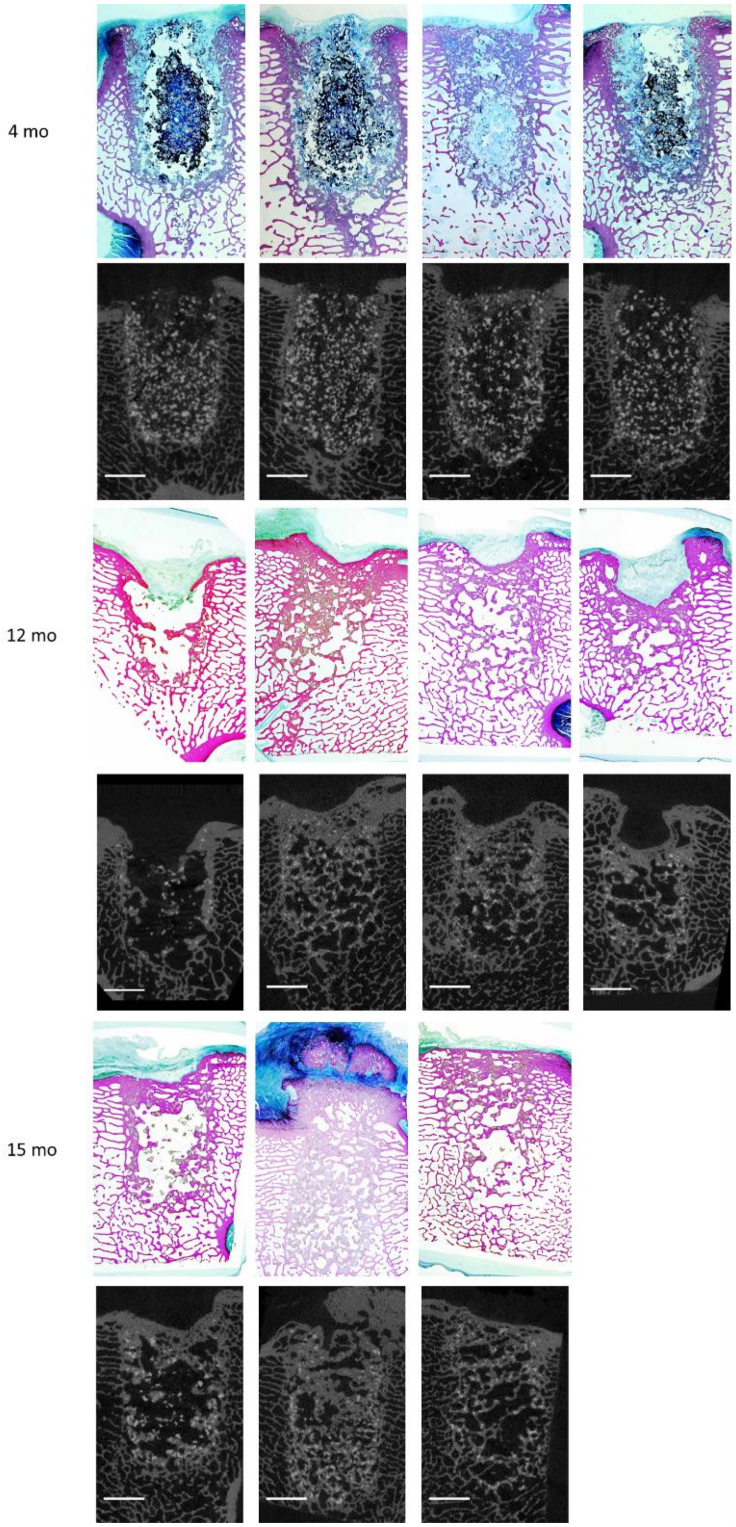

Figure 3.5. 2D μCT images (scale bar represents 5 mm) and Stevenson's blue/van Gieson stained histological sections (1x) for all samples in group LV/CM at 4 month, 12 month, and 15 month time points.

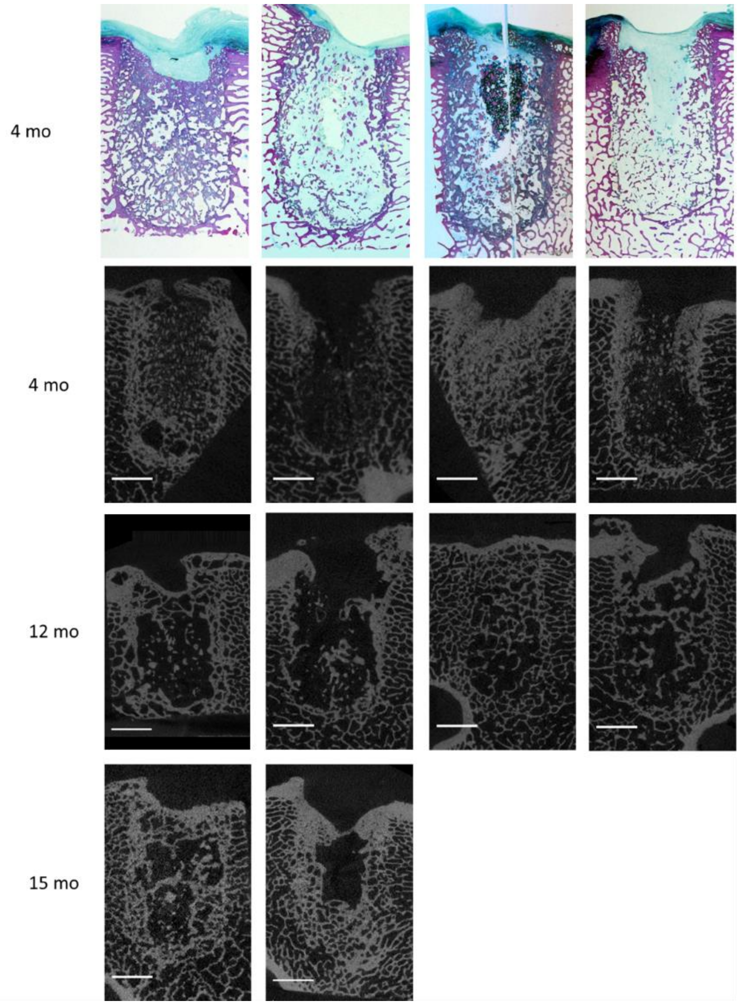

Figure 3.6. 2D µCT images (scale bar represents 5 mm) for all samples in group LV/A at 4 month, 12 month, and 15 month time points. Stevenson's blue/van Gieson stained histological sections (1x) of samples at 4 months.

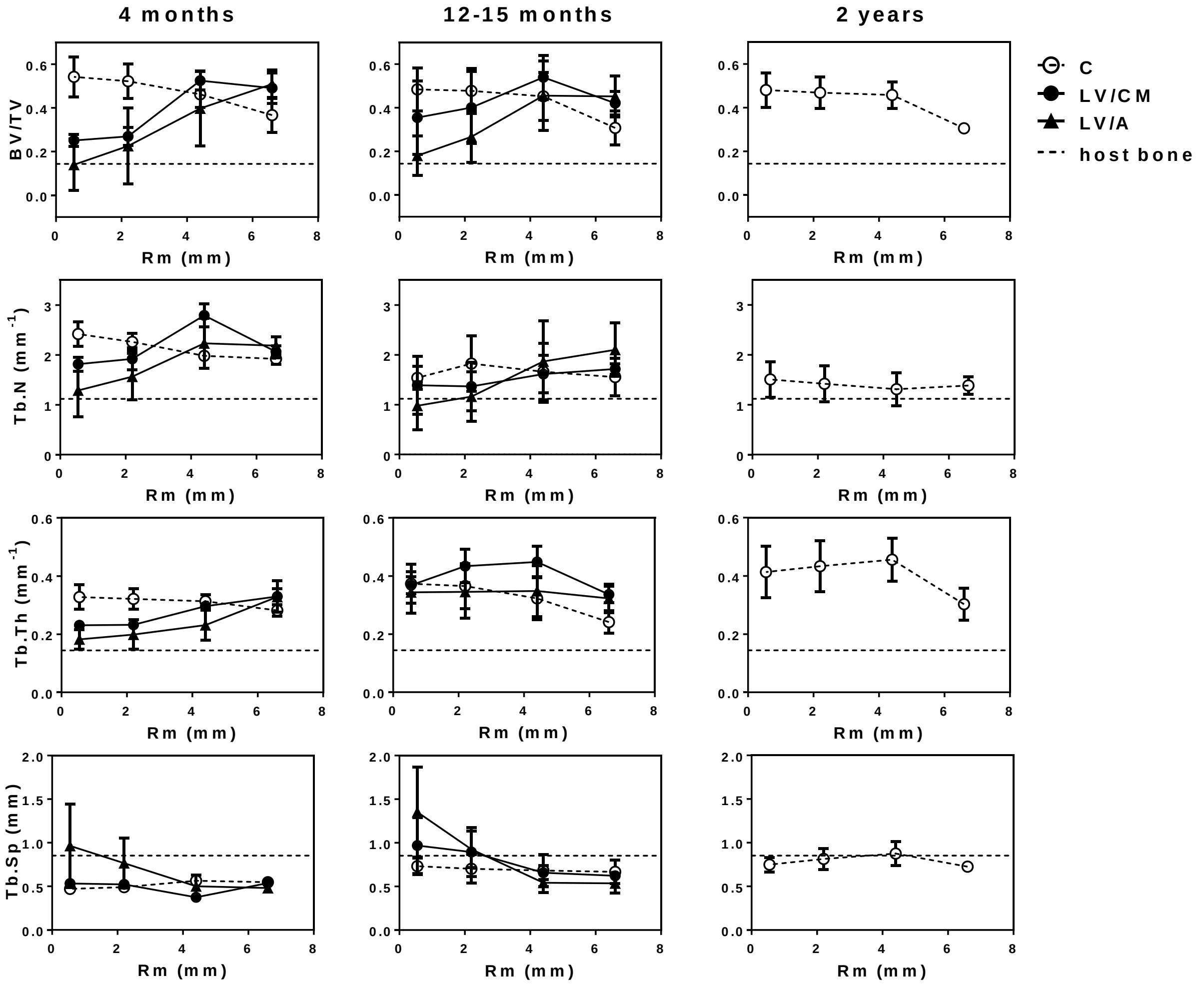

Figure 3.7. Quantitative analysis of morphometric parameters by µCT at each time point.

BV/TV for the control group decreased from 4 months to 1 year as the ceramic particles resorbed. Over the same time period, LV/CM treated samples showed increased BV/TV, particularly toward the center of the defect due to continuing new bone formation. BV/TV for LV/A remained largely unchanged, with some samples experiencing high degrees of remodeling and some showing little new bone. Tb.N values trended toward the value of host bone for all groups at 12-15 months. Tb.Th. at 12-15 months was largely independent of radial position as the defects had more interconnected bone rather than individual matrix particles. By 2 years, the morphometric parameters for the control group did not show as large a dependence on radial position, with values comparable to the 12-15 month time point, suggesting that remodeling was primarily complete.

Histology. Low-magnification images of histological sections of the best and worst performing samples (Figure 3.8) show extensive new bone formation in the CM control samples at 4 months with residual CM particles embedded in the new bone. LV/CM composites had large amounts of remaining matrix and PUR, particularly in the core of the defect. In LV/A samples, allograft particles are visible throughout the defect, with those close to the periphery of the graft undergoing active remodeling and those in the interior surrounded by residual polymer. At 12-15 months, both LV/CM and control groups showed CM particle remodeling and new bone throughout the defect.

High-magnification images of histological sections (Figure 3.9) reveal active remodeling of the grafts at 4 months, as evidenced by the presence of bone lining cells and osteoid. Remodeling of CM was visible at 4 months with degraded CM present within multinucleated osteoclast-like cells (OCL - double arrows) present in both the control and LV/CM groups. The majority of the new bone nucleated from the ceramic phase; however, some appositional new bone growth was observed on the residual PUR in the LV/CM samples. Lamellar bone formation (black arrows) was ongoing in LV/A grafts near the periphery of the defect. At 12 months, residual CM particles were still evident within the defects in the LV/CM and control groups, with ongoing CM remodeling by OCL, but the majority of the particles were fully or partially incorporated into new bone. Similar to the 12 month samples, residual CM was still evident at 2 years in the control group, with the particles fully incorporated into new bone. Based on low counts of macrophages and giant cells, the LV grafts appear to be well tolerated.

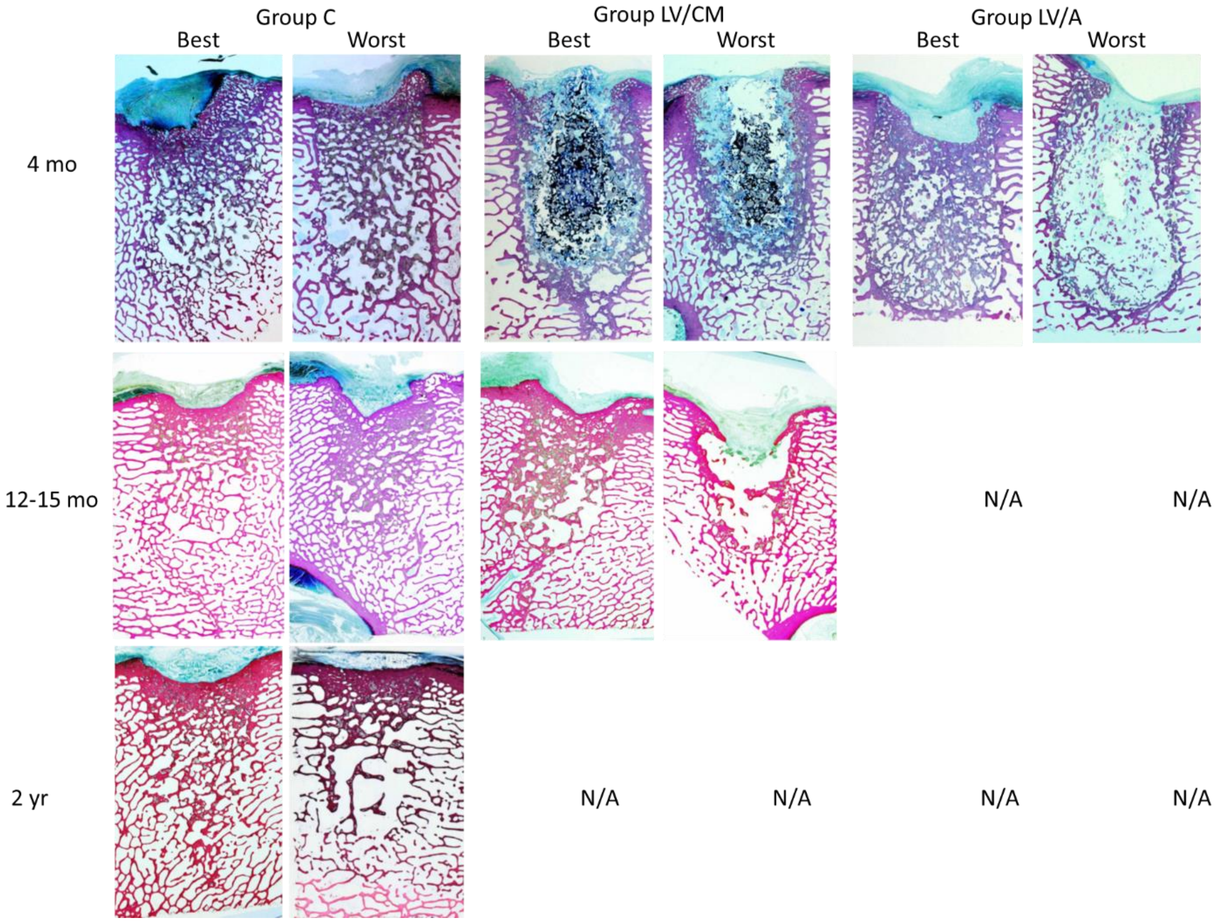

Figure 3.8. Low magnification histological analysis of new bone formation and residual matrix showing the best and worst performing samples in each group. Black/gray represents residual CM matrix, pink represents new bone or residual allograft, and dark blue points to remaining PUR.

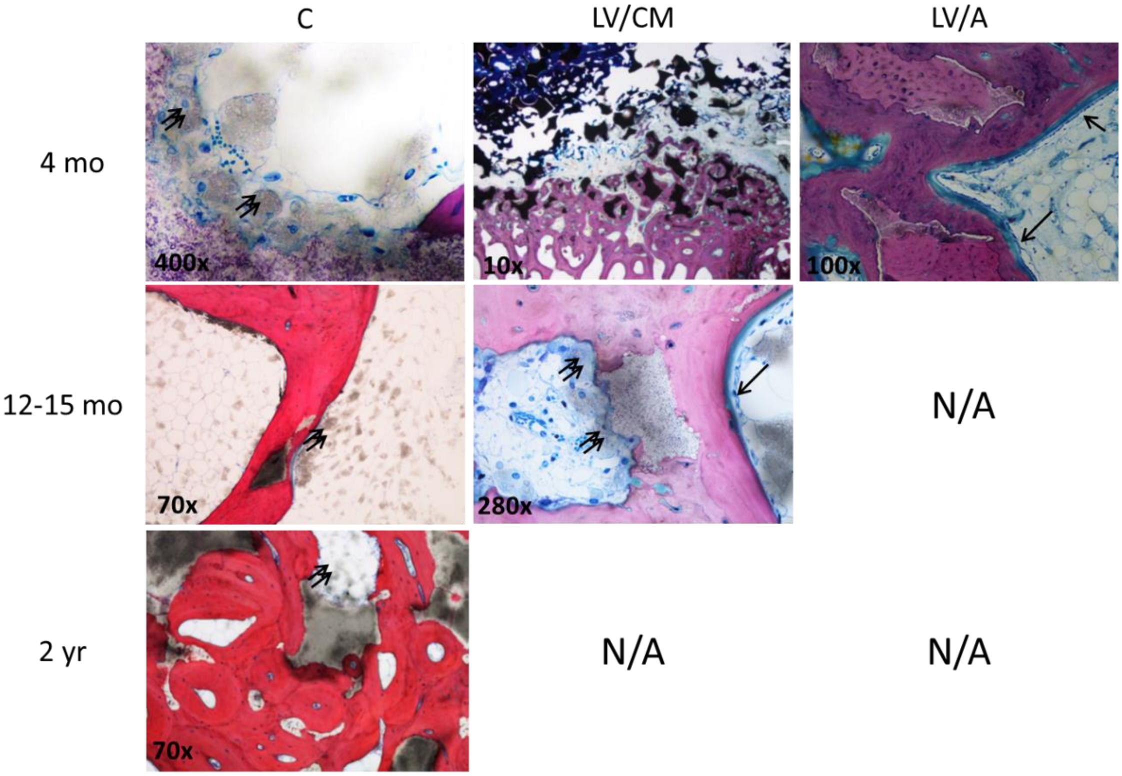

Figure 3.9**.** High magnification histological analysis of new bone formation and residual matrix. Pink/red represents new bone or residual allograft, cells are in blue, and residual CM stains black/gray. Non-mineralized fibrous tissue appears green. Residual PUR stains dark purple. Single arrows point to ongoing lamellar bone formation. Double arrows represent multinucleated osteoclast like cells (OCLs) incorporating CM matter.

Histomorphometry. At four months, the histomorphometry data are consistent with the radial μCT analysis (Figure 3.10). While the new bone formed in the ceramic control group was not dependent on radial position, the area% residual ceramic particles decreased with increasing radial distance from the center of the defect. LV composites remodeled from the host bone interface radially inward, with the highest amount of new bone near the host bone interface for the LV/CM and LV/A groups. The new bone present in the control defects was not statistically different from LV/CM or LV/A at any of the regions. The amount of residual ceramic was highest at the center of the defect and decreased radially outward for the LV/CM composites. The remaining allograft in the LV/A composites did not show a radial trend, with 12-15% of allograft remaining in the defect at all of the radial positions, suggesting that the allograft was not yet remodeling as the theoretical volume of the filler was initially ~15%. Residual PUR present within LV/CM and LV/A groups presented a trend of slower remodeling in the core of the defect. At 12 -15 months, new bone and remaining CM matrix were not dependent on radial position for either the control or LV/CM groups and results were similar between groups. Ceramic particles were still present at the later time point (less than 10%), but were more significantly remodeled than at 4 months.

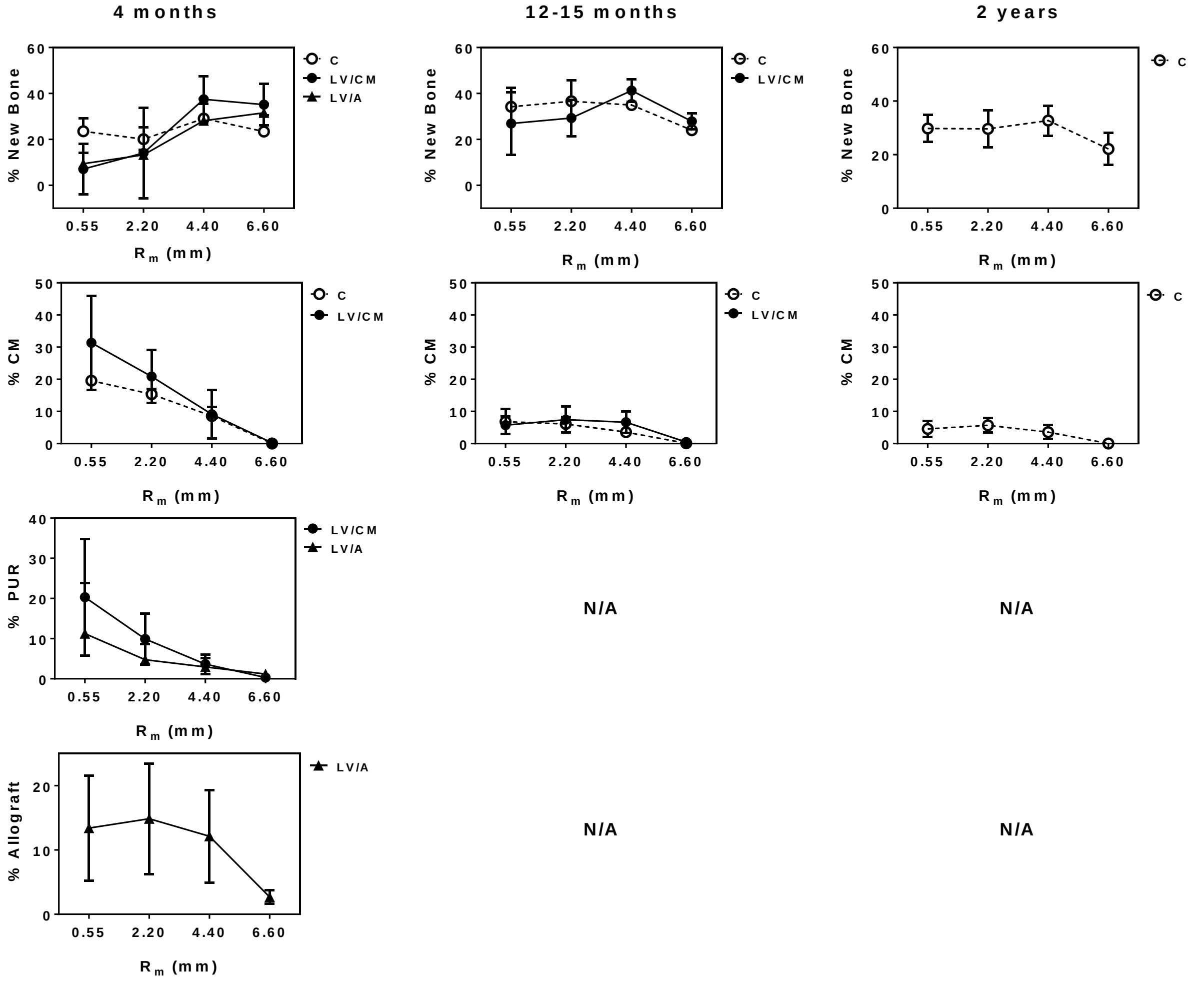

Figure 3.10**.** Histomorphometric analysis of new bone formation, residual matrix, and remaining PUR in LV composites and CM control.

Discussion

While ceramics are often used in bone void filler applications due to their osteoconductivity and biocompatibility, they typically cannot be administered by minimally invasive surgical techniques and have brittle mechanical properties. In this study, we designed low-viscosity (LV), injectable, compression-resistant ceramic/polymer composites and evaluated their remodeling potential in an ovine femoral condyle plug defect model. The ceramic component (CM) was MasterGraft™ (Medtronic, Memphis, TN), an FDA-approved bone void filler comprising 85% β-tricalcium phosphate (β-TCP) and 15% hydroxyapatite (HA). The polymer component was a poly(ester urethane) previously shown to support cellular infiltration, new bone formation, and degradation to non-cytotoxic breakdown products (14, 17, 29). The study was designed to answer two questions: (1) Do LV/CM composites heal similarly to the ceramic control? (2) What is the long-term fate of the ceramic particles? New bone formation and graft resorption were assessed at 4 months, 12 – 15 months, and 2 years. Appositional new bone growth was observed on the surface of the ceramic particles for both the control and LV/CM groups. While the mechanism of healing was similar for the control and LV/CM groups, the control group showed more reproducible healing at later (1 – 2 years) time points. LV grafts with allograft or ceramic showed more variable healing, most likely due to the low volume fraction of ceramic or allograft particles within the composites. In the control group, the ceramic particles were almost completely resorbed at 2 years.

The porosity of the LV/A and LV/CM composites was ~50%, which is comparable to the porosity of LV/A composites reported previously (14, 15, 17) that support cellular infiltration and new bone formation in a rabbit femoral plug defect model (30). The modulus and yield strength were higher for LV/A than LV/CM, which may be due to the smaller size of the allograft particles

(100 – 500 µm) compared to the CM granules (500 – 1500 µm). Smaller particles have previously been shown to lead to decreased pore size and increased yield strength of LV/A composites (15).

Lysine-derived polyurethane scaffolds undergo both hydrolytic and oxidative degradation *in vivo* (29). In buffer, the polymer component showed ~20% mass loss at 4 months. However, under oxidative conditions that simulate the adherent macrophage-biomaterial pocket (20% H_2O_2 + 0.1 M $CoCl_2$ (31)), the polymer degraded significantly faster (~75% mass loss at 7 weeks), which is consistent with previous studies on lysine-derived polyurethanes (29) Considering that new bone grows on both the ceramic and polymer phases, these observations may explain the less predictable healing observed at time points > 4 months. At these later time points, substantial polymer degradation is anticipated in the interior of the defect due to hydrolysis. Infiltration of cells into these interior regions is conjectured to accelerate resorption of the partially degraded polymer, resulting in insufficient surface area for new bone to form (18).

Lysine-derived polyurethane/allograft composites remodel and support new bone formation in metaphyseal bone defects in rats (12) and rabbits (15, 18). However, in the sheep defects evaluated in the present study, LV/A composites showed variable healing. Voids were observed in some of the LV/A-treated defects, as evidenced by µCT and histological sections. Allograft composites remodel by creeping substitution, in which the allograft particles are resorbed by osteoclasts followed by deposition of new bone by osteoblasts (14). Under conditions where the rate of polymer degradation exceeds that of new bone formation, resorption gaps can form due to insufficient surface area on which new bone can grow (18). These findings suggest that the imbalance between the rates of allograft resorption, polymer resorption, and new bone formation in LV/A composites may not affect healing of bone defects in smaller (rabbit) defects but may result in unpredictable healing in larger (sheep) defects.

The quantitative radial µCT and histomorphometric analysis support the notion that the ceramic control showed the most predictable healing. At 4 months, BV/TV (Figure 5) and area% new bone (Figure 7) were higher in the interior of the ceramic control group than in the LV grafts. For the ceramic control and LV/CM groups, new bone formed primarily on the surface of the ceramic particles. Consequently, the mechanism of healing was similar for the ceramic control and LV/CM groups, but the ceramic control group showed more new bone formation due in part to the higher initial concentration of ceramic particles.

While new bone formation progressed toward the interior of the ceramic control and LV/CM defects at 12 – 15 months, the area% new bone was more variable for LV/CM as evidenced by the larger error bars (Figure 7). The variability in healing at 12 – 15 months is further evidenced by images of µCT (Figure 3) and histological (Figure 5) sections, which show the differences in healing between the best and worst samples in each group. Histomorphometric measurements (Figure 7) show that the residual ceramic in the interior region of LV/CM grafts was 31.3 area%, which is higher than the calculated volume-averaged ceramic content of the composite (~15 vol%). This observation suggests that the ceramic particles were non-uniformly distributed in the defect and concentrated in the interior region as a result of the foaming reaction, which could have contributed to the more variable healing in the LV/CM group. The increased variability in healing of LV/CM composites from 4 to 12 months points to the importance of long-term time points for evaluating resorbable polymer/ceramic composites. Preclinical studies should be conducted with sufficient time points to fully characterize the resorption of the graft so that the mechanism of remodeling can be appropriately assessed and understood.

The Mastergraft® Mini-Granules evaluated in this study have been shown to support new bone formation in preclinical models of bone regeneration (21, 22). However, the long-term fate of this FDA-approved ceramic bone void filler has not been previously reported. New bone formation and ceramic resorption increased from 4 to 12 – 15 months (Figure 7). Similarly, the morphometric parameter Tb.N decreased with time and decreasing radial position (Figure 4) as the individual particles became incorporated into the new bone structure and the number of isolated ceramic granules decreased (15). However, the changes in these parameters from 12 – 15 months to 2 years were more modest (Figure 7). These observations suggest that remodeling was predominantly complete within the first year. *In vivo* resorption of β-TCP has been reported to be 80% complete at 6.5 months and 97% complete within 1.6 years (32). Considering the initial composition of the ceramic (85% β-TCP and 15% HA), the residual material at 2 years (~5 area%) may primarily comprise the more slowly degrading HA component.

Conclusions

In this study, the healing of low-viscosity, injectable ceramic and allograft composites was compared the ceramic clinical control in a large animal preclinical model of bone regeneration. At early time points (4 months), LV/CM composites healed similarly to the ceramic clinical control, while LV/A components showed more variable healing due to osteoclast-mediated of the allograft particles. At longer time points (12 – 15 months), healing of LV/CM composites was more variable due to the non-homogeneous distribution and lower concentration of the ceramic particles compared to the ceramic clinical control. Resorption of the ceramic particles was almost complete at 2 years. This study highlights the importance of optimizing the loading and distribution of ceramic particles in polymer/ceramic composites to maximize bone healing.

References

1. Lyons, F., Gleeson, J., Partap, S., Coghlan, K., andO'Brien, F. Novel Microhydroxyapatite Particles in a Collagen Scaffold: A Bioactive Bone Void Filler? Clinical Orthopaedics and Related Research® **472**, 1318, 2014.
2. Van der Stok, J., Van Lieshout, E.M.M., El-Massoudi, Y., Van Kralingen, G.H., andPatka, P. Bone substitutes in the Netherlands – A systematic literature review. Acta Biomaterialia **7**, 739, 2011.
3. Calori, G.M., Mazza, E., Colombo, M., andRipamonti, C. The use of bone-graft substitutes in large bone defects: any specific needs? Injury **42 Suppl 2**, S56, 2011.
4. Daculsi, G., Durand, M., Fabre, T., Vogt, F., Uzel, A.P., andRouvillain, J.L. Development and clinical cases of injectable bone void filler used in orthopaedic. IRBM **33**, 254, 2012.
5. Bohner, M., Galea, L., andDoebelin, N. Calcium phosphate bone graft substitutes: Failures and hopes. Journal of the European Ceramic Society **32**, 2663, 2012.
6. Scaglione, S., Lazzarini, E., Ilengo, C., andQuarto, R. A composite material model for improved bone formation. J Tissue Eng Regen Med **4**, 505, 2010.
7. Wagoner Johnson, A.J., andHerschler, B.A. A review of the mechanical behavior of CaP and CaP/polymer composites for applications in bone replacement and repair. Acta Biomaterialia **7**, 16, 2011.
8. Bongio, M., van den Beucken, J.J.J.P., Leeuwenburgh, S.C.G., andJansen, J.A. Development of bone substitute materials: from 'biocompatible' to 'instructive'. Journal of Materials Chemistry **20**, 8747, 2010.
9. Rezwan, K., Chen, Q.Z., Blaker, J.J., andBoccaccini, A.R. Biodegradable and bioactive porous polymer/inorganic composite scaffolds for bone tissue engineering. Biomaterials **27**, 3413, 2006.
10. Dong, Z., Li, Y., andZou, Q. Degradation and biocompatibility of porous nano-hydroxyapatite/polyurethane composite scaffold for bone tissue engineering. Applied Surface Science **255**, 6087, 2009.
11. Ryszkowska, J.L., Auguścik, M., Sheikh, A., andBoccaccini, A.R. Biodegradable polyurethane composite scaffolds containing Bioglass® for bone tissue engineering. Composites Science and Technology **70**, 1894, 2010.
12. Dumas, J.E., Zienkiewicz, K., Tanner, S.A., Prieto, E.M., Bhattacharyya, S., andGuelcher, S.A. Synthesis and characterization of an injectable allograft bone/polymer composite bone void filler with tunable mechanical properties. Tissue Engineering Part A **16**, 2505, 2010.
13. Yoshii, T., Dumas, J.E., Okawa, A., Spengler, D.M., andGuelcher, S.A. Synthesis, characterization of calcium phosphates/polyurethane composites for weight-bearing implants. Journal of Biomedical Materials Research Part B: Applied Biomaterials **100**, 32, 2012.
14. Dumas, J.E., Davis, T., Holt, G.E., Yoshii, T., Perrien, D.S., Nyman, J.S., Boyce, T., andGuelcher, S.A. Synthesis, characterization, and remodeling of weight-bearing allograft bone/polyurethane composites in the rabbit. Acta Biomaterialia **6**, 2394, 2010.
15. Prieto, E.M., Talley, A.D., Gould, N.R., Zienkiewicz, K.J., Drapeau, S.J., Kalpakci, K.N., andGuelcher, S.A. Effects of particle size and porosity on in vivo remodeling of settable allograft bone/polymer composites. Journal of Biomedical Materials Research Part B: Applied Biomaterials, n/a, 2015.

16. Talley, A.D., Kalpakci, K.N., Zienkiewicz, K.J., Cochran, D.L., andGuelcher, S.A. Space Maintenance and New Bone Formation with Low-Viscosity, Compression-Resistant Bone Grafts in a Canine Mandibular Ridge Saddle Defect. Tissue Eng **Submitted**.
17. Page, J.M., Prieto, E.M., Dumas, J.E., Zienkiewicz, K.J., Wenke, J.C., Brown-Baer, P., andGuelcher, S.A. Biocompatibility and chemical reaction kinetics of injectable, settable polyurethane/allograft bone biocomposites. Acta Biomaterialia **8**, 4405, 2012.
18. Dumas, J.E., Prieto, E.M., Zienkiewicz, K.J., Guda, T., Wenke, J.C., Bible, J., Holt, G.E., andGuelcher, S.A. Balancing the rates of new bone formation and polymer degradation enhances healing of weight-bearing allograft/polyurethane composites in rabbit femoral defects. Tissue Eng Part A **20**, 115, 2014.
19. Yuan, H., Fernandes, H., Habibovic, P., de Boer, J., Barradas, A.M., de Ruiter, A., Walsh, W.R., van Blitterswijk, C.A., andde Bruijn, J.D. Osteoinductive ceramics as a synthetic alternative to autologous bone grafting. Proc Natl Acad Sci U S A **107**, 13614, 2010.
20. Bodde, E.W.H., Wolke, J.G.C., Kowalski, R.S.Z., andJansen, J.A. Bone regeneration of porous β-tricalcium phosphate (Conduit™ TCP) and of biphasic calcium phosphate ceramic (Biosel®) in trabecular defects in sheep. Journal of Biomedical Materials Research Part A **82A**, 711, 2007.
21. Kinsella, C.R.J., Bykowski, M.R., Lin, A.Y., Cray, J.J., Durham, E.L., Smith, D.M., DeCesare, G.E., Mooney, M.P., Cooper, G.M., andLosee, J.E. BMP-2-Mediated Regeneration of Large-Scale Cranial Defects in the Canine: An Examination of Different Carriers. Plastic and Reconstructive Surgery **127**, 1865, 2011.
22. Herford, A.S., Lu, M., Buxton, A.N., Kim, J., Henkin, J., Boyne, P.J., Caruso, J.M., Rungcharassaeng, K., andHong, J. Recombinant human bone morphogenetic protein 2 combined with an osteoconductive bulking agent for mandibular continuity defects in nonhuman primates. Journal of Oral and Maxillofacial Surgery **70**, 703, 2012.
23. Dumas, J.E., BrownBaer, P.B., Prieto, E.M., Guda, T., Hale, R.G., Wenke, J.C., andGuelcher, S.A. Injectable reactive biocomposites for bone healing in critical-size rabbit calvarial defects. Biomed Mater **7**, 024112, 2012.
24. Guelcher, S., Srinivasan, A., Hafeman, A., Gallagher, K., Doctor, J., Khetan, S., McBride, S., andHollinger, J. Synthesis, in vitro degradation, and mechanical properties of two-component poly(ester urethane)urea scaffolds: effects of water and polyol composition. Tissue Eng **13**, 2321, 2007.
25. Guelcher, S.A., Patel, V., Gallagher, K.M., Connolly, S., Didier, J.E., Doctor, J.S., andHollinger, J.O. Synthesis and in vitro biocompatibility of injectable polyurethane foam scaffolds. Tissue engineering **12**, 1247, 2006.
26. Christenson, E.M., Anderson, J.M., andHiltner, A. Oxidative mechanisms of poly(carbonate urethane) and poly(ether urethane) biodegradation: In vivo and in vitro correlations. J Biomed Mater Res A **70A**, 245, 2004.
27. Martin, J.R., Gupta, M.K., Page, J.M., Yu, F., Davidson, J.M., Guelcher, S.A., andDuvall, C.L. A porous tissue engineering scaffold selectively degraded by cell-generated reactive oxygen species. Biomaterials **35**, 3766, 2014.
28. Harmata, A., Ma, Y., Sanchez, C., Zienkiewicz, K., Elefteriou, F., Wenke, J., andGuelcher, S. d-amino Acid Inhibits Biofilm but not New Bone Formation in an Ovine Model. Clinical Orthopaedics and Related Research®, 1, 2015.

29. Hafeman, A.E., Zienkiewicz, K.J., Zachman, A.L., Sung, H.J., Nanney, L.B., Davidson, J.M., andGuelcher, S.A. Characterization of the degradation mechanisms of lysine-derived aliphatic poly(ester urethane) scaffolds. Biomaterials **32**, 419, 2011.

30. Talley, A.D., Funk, S.S., Zienkiewicz, K.J., Dasgupta, J., Wenke, J.C., Davidson, J.M., Holt, G.E., andGuelcher, S.A. *In vivo* rhBMP-2 Release from Degradable Polyurethane Composites. Artif Organs **Submitted**.

31. Zhao, Q.H., McNally, A.K., Rubin, K.R., Renier, M., Wu, Y., Rose-Caprara, V., Anderson, J.M., Hiltner, A., Urbanski, P., andStokes, K. Human plasma alpha2-macroglobulin promotes in vitro oxidative stress cracking of Pellethane 2363-80A: In vivo and in vitro correlations. J Biomed Mater Res **27**, 379 1993.

32. Wiltfang, J., Merten, H.A., Schlegel, K.A., Schultze-Mosgau, S., Kloss, F.R., Rupprecht, S., andKessler, P. Degradation characteristics of α and β tri-calcium-phosphate (TCP) in minipigs. Journal of Biomedical Materials Research **63**, 115, 2002.

CHAPTER IV

IN VIVO rhBMP-2 RELEASE KINETICS FROM INJECTABLE DEGRADABLE POLYURETHANE COMPOSITE BONE GRAFTS

Introduction

Treatment of non-unions and large bony defects often comprises autologous or allogeneic bone grafts (1). However, these approaches are limited by the availability of autograft and patient morbidity associated with harvesting (2). Tissue engineering approaches that incorporate growth factors or other signaling molecules are effective at regenerating new tissue such as bone. In treating bony defects, growth factors can be combined with delivery systems to regulate osteogenesis and bone tissue regeneration (3). Ideally, a growth factor delivery system will fulfill the targeted requirements for bone grafts, which include osteoconductivity, osteoinductivity, degradation to non-toxic byproducts, appropriate mechanical strength, and porosity (4,5).

Biodegradable lysine-derived polyurethane scaffolds have been extensively investigated for bone tissue engineering applications (6,7). These non-immunogenetic materials breakdown by hydrolytic and cell-mediated oxidative degradation to non-toxic decomposition products (8,9). When tested in femoral plug defects in rabbits, the polyurethane scaffolds supported cellular infiltration and new bone formation (10). Considering the high ductility but low mechanical strength of polymers, they are often blended with ceramics to improve their mechanical properties and osteoconductivity (11). Additionally, polymer/ceramic composites have been utilized as delivery systems for growth factors in bone repair (12,13).

Osteoinductive growth factors delivered locally help regulate the complex process of bone repair and restoration. Recombinant human bone morphogenetic protein-2 (rhBMP-2), the most extensively investigated growth factor for bone regeneration, enhances new bone formation by stimulating recruitment of osteoprogenitor cells and osteoblast differentiation (14). A variety of rhBMP-2 delivery vehicles have been studied in preclinical models of bone regeneration, including calcium phosphates (15), hydrogels (16,17), collagen scaffolds (18), and poly(lactic-co-glycolic acid) (19). RhBMP-2 delivered via an absorbable collagen sponge (ACS) (INFUSE® bone graft, Medtronic) is FDA-approved for the treatment of posterior-lateral spinal fusions, fractures of the tibial mid-diaphysis, and lateral ridge augmentation and sinus lift procedures. A high initial burst release of rhBMP-2 is observed when delivered with the ACS carrier. Recent studies have shown that an initial burst followed by sustained release of the growth factor contributed to more new bone (20,21). Furthermore, rhBMP-2 release and new bone formation is highly dependent on the nature of the carrier, which demonstrates the importance of measuring *in vivo* release kinetics for delivery systems of interest (21).

High porosity and increased pore size of bone grafts enhance mass transfer of oxygen and nutrients, thereby increasing osteoblast proliferation and survival in 3D scaffolds (22). Additionally, highly interconnected scaffolds lead to more bone growth within shorter periods of time (23). Porosity can be especially important in a scaffold containing a slowly degrading phase, such as ceramic particles. One approach to increase porosity and interconnectivity of scaffolds is to include a porogen that rapidly dissolves to form pores. With the incorporation of a growth factor, a more highly interconnected and porous scaffold would be expected to release the growth factor more rapidly.

Measurement of rhBMP-2 release kinetics *in vitro* entails a simple ELISA analysis following an elution study. In contrast, *in vivo* release kinetics are more challenging to measure, requiring the use of 125I radiolabeled protein (24,25) or fluorescent tagging with non-invasive imaging (26,27). In the present study, we measured the release of rhBMP-2 from injectable, cell-degradable polyurethane composites *in vitro* and in a rabbit femoral plug defect model over 8 weeks. While previous studies have reported diffusion-controlled release of rhBMP-2 from polyurethane scaffolds *in vitro* (20,28), we hypothesized that under *in vivo* conditions, the release kinetics are controlled by both diffusion and degradation of the scaffold, which degrades in response to reactive oxygen species (ROS) secreted by infiltrating cells (8). New bone formation measured for polyurethane composites incorporating a sucrose porogen or ceramic microparticles was compared to a control comprising rhBMP-2 delivered from the ACS carrier. While composites containing a porogen have greater porosity and interconnectivity, we hypothesized that composites incorporating ceramic microparticles would enhance new bone formation and healing due to their increased osteoconductivity.

Experimental

Materials. Lysine triisocyanate-polyethylene glycol (PEG, 200 g mol-1) prepolymer (LTI-PEG, 21.7% NCO) was obtained from Ricerca Biosciences LLC (Painesville, OH). Glycerol, stannous octoate, and ε-caprolactone were purchased from Sigma-Aldrich (St. Louis, MO). Glycolide and DL-lactide were supplied by Polysciences (Warrington, PA). Triethylene diamine (TEDA) and dipropylene glycol (DPG) were purchased from Sigma Aldrich and mixed to obtain a 10% (w/w) solution of TEDA in dry DPG. MASTERGRAFT® Mini Granules and absorbable collagen sponges (ACS) were received from Medtronic Spinal and Biologics (Memphis, TN). Na125I was purchased from PerkinElmer (Waltham, MA). Ultrapure sucrose was purchased from Spectrum Chemicals & Laboratory Products (Brunswick, NJ). Recombinant human bone morphogenetic protein-2 (rhBMP-2) was purchased from R&D systems (Minneapolis, MN). For oxidative media, CoCl2 was bought from Sigma-Aldrich (St Louis, MO) and 30 wt% H2O2 from Fisher Scientific (Pittsburgh, PA).

Synthesis of polyester triol. The polyester triol was synthesized as previously described (29,30). Briefly, glycerol was mixed with ε-caprolactone, glycolide, and DL-lactide monomers under argon at 140 °C for 40 hrs. The polyester triol was then cooled, washed with hexane, and dried under vacuum at 80 °C. The backbone of the polyester triol consisted of 70% ε-caprolactone, 20% glycolide, and 10% DL-lactide, with a molecular weight of 450 g mol^{-1}.

rhBMP-2 radiolabeling. To determine *in vivo* release kinetics, a fraction of the rhBMP-2 was radiolabeled as described previously (24). 100 µl of a 1.43 CM/ml rhBMP-2 solution, 20 µl of a 0.1 M NaOH solution and 2mCi of Na125I were combined in a pre-coated iodination tube (Pierce, Rockford, IL). After incubation at room temperature for 15 min, the solution was dialyzed (10kDa molecular weight cutoff (MWCO) Slide-A-Lyzer®, Pierce) for 24 hr with three times media change against an aqueous rhBMP-2 buffer containing 5mM glutamic acid, 2.5 wt% glycine, 0.5 wt% sucrose, and 0.01 wt% Tween 80 (pH 4.5). The labeled rhBMP-2 was mixed with unlabeled rhBMP-2 to obtain a hot:cold ratio of 1:8. The solution was aliquoted and lyophilized in appropriate doses.

Fabrication of composites. Ultrapure sucrose was ground and sieved to 100-500 µm. Low-viscosity (LV), injectable polyurethane composites were prepared by mixing the components using a two-step method. In the first step, polyester triol, matrix particles (sucrose (S) or Mastergraft (ceramic - CM)), and TEDA (1.2 pphp) were added to a 10-mL cup and mixed by hand for 30 s. CM (85% β-tricalcium phosphate/15% hydroxyapatite) ceramic granules resorb at a rate designed to match that of new bone formation and is cleared by the United States Food and Drug Administration (FDA) for sale as a bone void filler. The LTI-PEG and lyophilized rhBMP-2 were added to the cup and mixed by hand for 60 s. The index (ratio of isocyanate:hydroxyl equivalents x 100) was 115. The composites contained either 45 wt% CM (LV/CM) or 40 wt% S (LV/S). For *in vivo* grafting, a rhBMP-2 dose of 100 µg/mL (defect volume) was tested. For material characterization, the reactive mixture was mixed with 3 pphp of DI water (to simulate the fluid of *in vivo* conditions), loaded into a straight bore syringe, and injected into a 6mm vial for further analysis.

Material Characterization. LV/S samples were immersed in PBS at 37°C for 7 days, with PBS changes every 2 days, to leach the sucrose from the scaffold. Afterwards, LV/S was washed 3 times with DI H2O and dried in a vacuum oven at 40°C overnight. LV/S, LV/CM, and leached LV/S samples were cut into thin sections, mounted onto a scanning electron microscopy (SEM) pin stub mount, and sputter-coated for 45 s using a Cressington Q108 sputter coater, which deposited gold at a 30 mA current. A Hitachi S-4200 SEM was used to acquire images at a voltage of 1kV.

Oxidative degradation of lysine-derived polyurethane scaffolds. Polyurethane foams without sucrose or ceramic particles were fabricated as described above. Triplicate samples (~50 CM) were cut from the foams and incubated at 37°C in oxidative media containing 0.1M CoCl2 in 20 wt% H2O2. This oxidative media simulates the privileged microenvironment between adherent macrophages and the biomaterial surface (31,32). The media was replaced every 2-3 days to preserve the oxidative power of the solution. At desired time points samples were removed from media, washed 3x with DI water, and dried under vacuum at 40°C overnight prior to weighing. Data were plotted as the remaining mass percent over time when normalized to initial weight.

Mechanical Testing. Cylindrical samples with 6 mm diameter and lengths of approximately 12 mm were prepared with porosities of approximately 50% (measured gravimetrically). Samples were submerged in phosphate-buffered saline for 24 h prior to mechanical testing. Compression testing was performed using an MTS 898 Bionix system (Eden Prairie, MN) with a 1-kN load cell. Samples were preloaded to 1 N (LV/S) or 3 N (LV/CM) and compressed at a constant rate of 25 mm/min. The original cross sectional area of the cylinders was used to calculate compressive stress. Compressive modulus was calculated as the slope of the initial linear portion of the stress-strain curve. The LV/S composites could not be compressed to failure due to their high elasticity, and therefore compressive stress was reported at 20% strain as a measure of compressive strength. Porosity and compression data were presented as mean ± standard deviation of triplicate samples. Statistics were tested by an unpaired Student's t-test and significance measured at $p < 0.05$.

Table 4.1. *In vivo* study design for rhBMP-2 release experiment in rabbits

Treatment Group	**Filler**	**rhBMP-2 (μg/cm^3 defect volume)**	**n 8 weeks**
ACS	N/A	100	4
LV/CM	mastergraft	100	4
LV/S	sucrose	100	4

Animal Study. Six male New Zealand white rabbits weighing 3.1-3.6 kg were used in this study. All surgical and care procedures were carried out under aseptic conditions according to the approved IACUC protocol. The study design is listed in Table 4.1. The individual components of the LV grafts were gamma-irradiated using a dose of 25 kGY. Bilateral critical-sized defects of 5 mm by 6-8 mm in depth were drilled in the lateral femoral condoyles of each rabbit. Defects were treated with LV/CM, LV/S, or ACS (n=4) augmented with rhBMP-2. The ACS carrier was chosen as the clinical control due to its widespread use in bone repair and FDA approval. For the LV grafts, the reactive paste was injected into the defect site and allowed to cure for 10 min prior to soft tissue closure. For the ACS carrier, the lyophilized growth factor was reconstituted in sterile water and injected onto the collagen sponge. The sponge was allowed to adsorb the rhBMP-2 solution for at least 15 min prior to implantation. A dose of 100 μg/ml rhBMP-2 (based on defect volume) was investigated, considering a previous study reporting that a dose of 80 μg/ml rhBMP-2 with LV grafts was shown to enhance bone formation and bridging in rabbit calvarial defects (7). The rabbits were euthanized after eight weeks. The femurs were extracted and fixed in 10% formalin for two weeks prior to processing for histology.

In vitro and in vivo release kinetics. For *in vitro* release measurements, three replicate rhBMP-2-loaded porous scaffolds (~ 50 CM) were placed in a closed vial containing 1 mL of release media (α-MEM with 1% BSA) in an incubator at 37°C. The composites contained 100 μg rhBMP-2/mL scaffold to mimic the *in vivo* study. BSA was included to minimize adsorption of rhBMP-2 to the sample vial (28). Media was collected and replaced every day to minimize degradation of the rhBMP-2. The media samples were pooled as indicated on the release plot and concentration was measured for triplicate samples using a Human BMP-2 Quantikine ELISA kit (R&D systems). The release plot was generated from a logarithm curve fit of the raw data. *In vivo* retention of rhBMP-2 was measured using a scintillation probe collimated with a hollow tube wrapped in leaded tape (Model 44-3 scintillator, Ludlum Measurement Inc., Sweetwater, TX) and connected to a digital scaler (Model 2241-3 scaler, Ludlum Measurements Inc.). The rabbits were restrained and radioactive counts were obtained over 1 min intervals, repeated twice at each time point. The 125I counts were normalized to time 0 measurements and corrected for radioactive decay.

Release Kinetics Analysis. Cumulative release curves were fit to the semi-empirical Weibull-model, Equation 4.1 (33,34):

$$\frac{M_t}{M_\infty} = 1 - \exp\left(-a \cdot t^b\right) \tag{4.1}$$

where M_t = the cumulative amount of rhBMP-2 released at time t, M_∞ = the cumulative amount of rhBMP-2 released at infinite time (assumed equivalent to the amount of rhBMP-2 added to the graft), and a and b are constants. Values of $b < 0.75$ suggest a Fickian diffusion release mechanism, while $b > 0.75$ suggests a combined release mechanism (33,34).

Micro-computed tomography (µCT) analysis. A µCT50 (SCANCO Medical, Basserdorf Switzerland) was used to acquire scans of the extracted femurs in formalin at 70 kVp energy, 114 µA source current, 250 projections per rotation, 400 ms integration time, and an isotropic voxel size of 36 µm. Axial images were reconstituted using manufacturer provided software. Attenuation values were converted to tissue mineral density (TMD) through calibration with hydroxyapatite (HA) phantoms with densities of 0 to 780 CM HA cm-3 (calibrations checked weekly). Using the cortical borders of the defect for alignment, the reconstructed image stack was re-oriented so that the depth of the defect was parallel to the z-axis. Radial analysis of morphometric parameters was conducted from the core of the implant to the interface with host bone. Three concentric annular volumes of interest with thickness of 1 mm and a cylindrical core with a diameter of 1mm each with the approximate length of 7 mm (from the outer cortical surface of the femur) were defined for each sample. The three inner cylindrical sections covered the defect volume, while the outer region provided information about the interface with host bone. Ossified tissue was segmented from soft tissue using the lower and upper threshold of 289 CM HAcm-3 and 1000 CM HAcm-3 respectively, with a Gaussian noise filter settings of sigma 0.7 and support 2. Morphometric parameters within the annular regions were calculated, grouped by treatment and time point, and plotted versus the mean radial distance (R_m) from the core of the defect ($R_m=(R_o+R_i)/2$, where R_o

and R_i correspond to the outer and inner radius of each region, respectively). Bone volume/total volume (BV/TV), trabecular number (Tb.N), trabecular thickness (Tb.Th), and trabecular separation (Tb.Sp) within the regions of interest were computed using SCANCO's Medical microCT systems software as previously described (35).

Histology. After fixation in formalin, the femurs were dehydrated in a graded series of ethanol and embedded in poly(methylmethacrylate). Sections were cut from the resulting blocks using an Exakt band saw. The sections were then ground and polished using an Exakt grinding system to <100 μm and stained with Sanderson's rapid bone stain. New bone stained red while remaining CM stained black. The polymer was stained dark blue and cells stained light blue.

Results

Composite characterization. Physical and mechanical properties of LV grafts are summarized in Table 4.2. Initial porosities were similar for LV/CM and LV/S groups (~50%) and comparable to LV/allograft composites described in a previous study (7). Representative SEM images (Figure 4.1) illustrate the pore structure of the composites. The sucrose leaches from the LV/S scaffolds within a few days in an aqueous environment, resulting in a porosity of 67% (Figure 1C). As expected, the addition of ceramic particles in LV/CM increased the compressive modulus compared to LV/S. Additionally, the compressive stress measured at 20% strain for LV/CM composites was more than twice that for the LV/S composites.

Table 4.2. Physical and mechanical properties of LV grafts tested in the rhBMP-2 release study

Treatment Group	**Initial Porosity (%)**	**Porosity After Leaching (%)**	**Modulus (MPa)**	**Compressive Strength at 20% Strain (MPa)**
LV/CM	53.2 ± 1.3	N/A	1.45 ± 0.29[a]	0.29 ± 0.06[a]
LV/S	50.5 ± 2.8	67.1 ± 1.8	0.86 ± 0.13	0.13 ± 0.03

[a] statistically different with $p < 0.05$

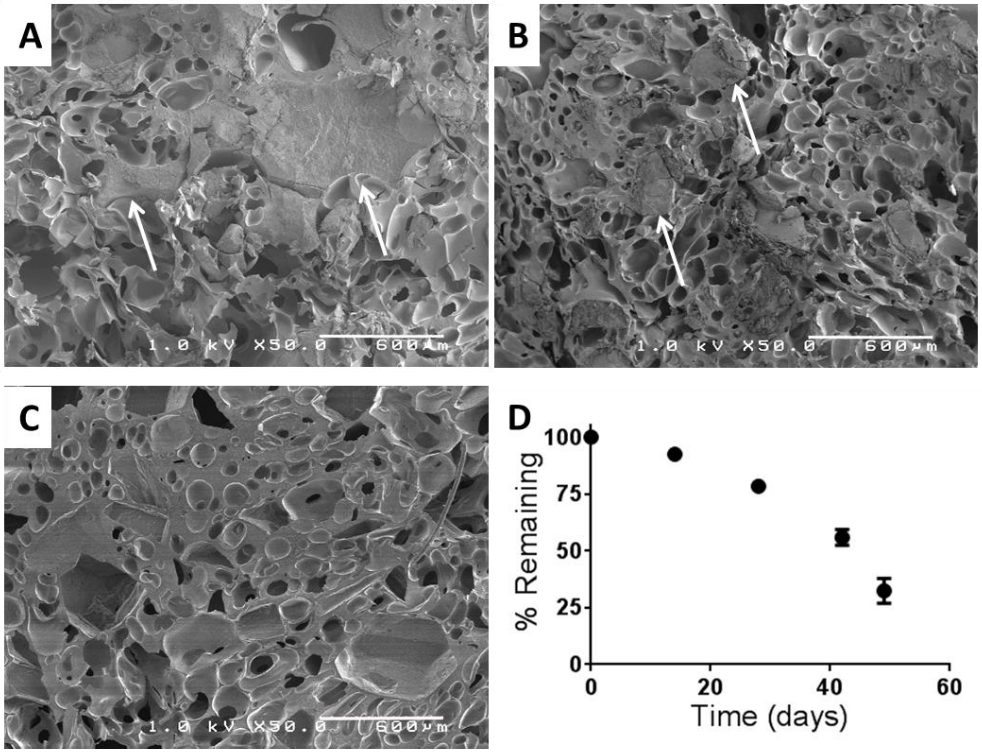

Figure 4.1. SEM images of (A) LV/CM, (B) LV/S before leaching, and (C) LV/S after leaching of the sucrose particles where the scale bar represents 600 µm. White arrows point to filler particles embedded in polymer. (D) Degradation (mass loss) of PUR foams in oxidative media (0.1M $CoCl_2$ in 20 wt% H_2O_2) over time.

rhBMP-2 release. To evaluate the *in vitro* release of rhBMP-2, lyophilized protein was incorporated into LV composites or ACS and the release kinetics measured by ELISA (Figure 4.2A). After one week, all of the growth factor was released from the ACS samples. Conversely, the LV grafts showed less than 50% release of rhBMP-2 within this time frame. By four weeks, approximately 75% of rhBMP-2 was released from the LV grafts. There was minimal difference in release kinetics between LV/CM and LV/S composites, despite the significant difference in porosity.

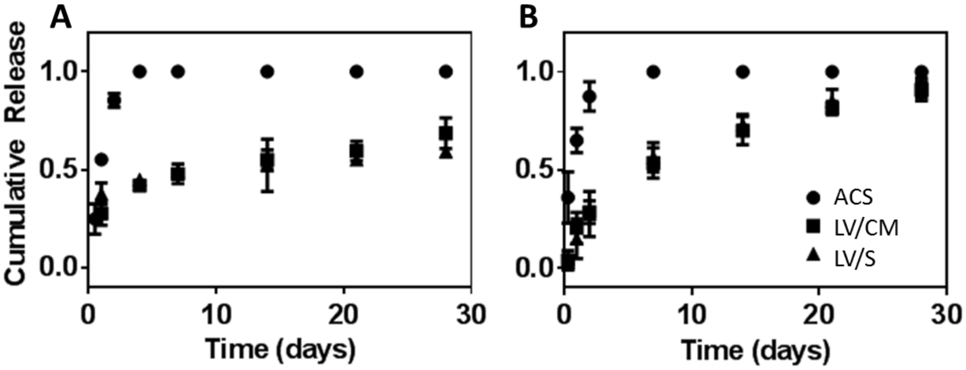

C

Treatment Group	*In vitro*			*In vivo*		
	a	b	R^2	*a*	b	R^2
ACS	0.774	1.37	0.998	1.01	0.848	0.998
LV/S	0.468	0.184	0.982	0.167	0.806	0.997
LV/CM	0.323	0.359	0.983	0.184	0.765	0.993

Figure 4.2. Cumulative rhBMP-2 release kinetics from LV and ACS grafts. (A) *In vitro* release measured by ELISA. (B) *In vivo* release measured by ^{125}I radiolabeling. (C) Fitting of *in vitro* and *in vivo* release kinetics data to the Weibull model.

In vivo release of rhBMP-2 was measured in femoral plug defects in rabbits (Figure 4.2B). This study provided data for the local release of rhBMP-2 from the defect site, but did not investigate the systemic biodistribution of the growth factor. Similar to the *in vitro* results, the release from the ACS samples was complete after the first week. In the LV samples, there was a burst release of 25% growth factor within the first 3 days and 50% within the first week. No growth factor was measured within the defect site after 4 weeks. The rhBMP-2 release was slightly faster for LV composites *in vivo* compared to *in vitro*.

Cumulative release curves were fit to the semi-empirical Weibull model (Eq 4.1). The values of the parameter b measured *in vitro* for the LV/S and LV/CM were 0.184 and 0.359 respectively, which are within the range for Fickian diffusion ($b < 0.75$). In contrast, the values of 0.848 (LV/S) and 0.765 (LV/CM, Figure 4.2C) determined by fitting the *in vivo* release kinetics to the Weibull model are within the range for a combined (Fickian diffusion and scaffold degradation) release mechanism. Fitting the ACS release data yielded b values of 1.37 *in vitro*, corresponding to a complex release mechanism, and 0.848 *in vivo*, corresponding to a combined release mechanism.

Oxidative degradation of lysine-derived polyurethane scaffolds. The polyurethane foams prepared without sucrose or CM microparticles had a porosity of 72.3 ± 2.2 %, which is higher than that of samples fabricated with the microparticles. Mass loss was measured at several time points for up to 7 weeks (Figure 4.1D), at which time the samples had degraded too extensively to weigh the samples. The samples lost 50% of their mass within 6 – 7 weeks, which is consistent with a previous sub-cutaneous implantation study (8).

μCT analysis. Representative μCT images of all three treatment groups are presented in Figure 3A-C, where the dotted lines represent the approximate edges of the original defects. Defects treated with LV/S did not heal, and minimal new bone was visible in the defect. ACS-treated defects showed isolated islands of new bone throughout the defect, but the bone structure was not a continuous phase as observed in host bone. In the LV/CM group, new bone formation was visible interspersed within the residual CM particles (bright white particles) throughout the volume of the defect. Morphometric parameters evaluated by □CT were plotted as a function of the mean radial distance from the core of the defect to monitor remodeling (Figure 3D-G). The bone volume/total volume (BV/TV) data, which includes both new bone and residual CM, showed that the vol% of mineralized graft was highest in the center of the defect for the LV/CM samples. For the LV/S and ACS groups, BV/TV was lowest in the center of the defect and increased radially outward toward the host bone interface. A similar trend was evident with the trabecular number (Tb.N) parameter. ACS-treated defects did not heal as well as expected, most likely due to the lower dose of rhBMP-2 (100 µg/mL) compared to the dose recommended for the collagen carrier in rabbits (400 µg/mL). The trabecular thickness (Tb.Th) and trabecular spacing (Tb.Sp) parameters showed similar results between LV/S and ACS, with LV/CM composites showing the highest Tb.Th and lowest Tb.Sp. All groups showed a dependence of morphometric parameters based on radial position, as remodeling was not complete by 8 weeks.

Histology. In all treatment groups, a large number of cells were visible within the defect, which suggests that cells had infiltrated the bone grafts by 8 weeks. However, the LV/CM was the only one that showed substantial new bone formation. Figure 4 shows representative high-magnification images of histological sections for the LV/CM group. New bone appears red, residual CM particles appear black, and cells are blue. Appositional growth of new bone was observed near the surface of the CM particles.

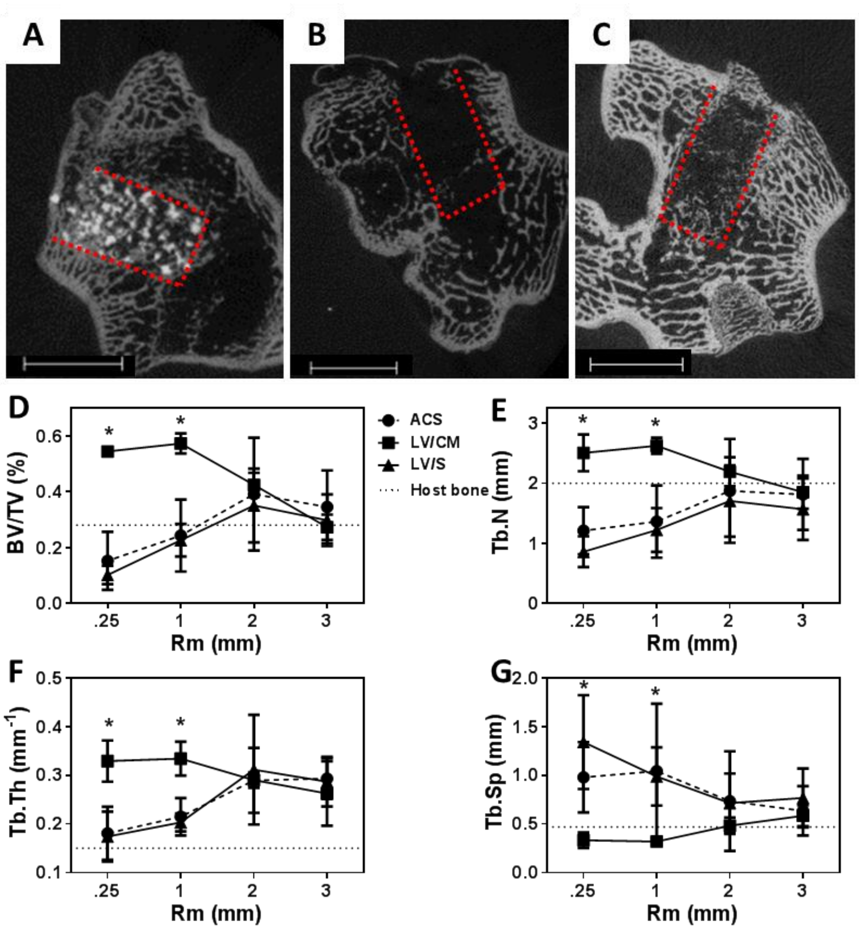

Figure 4.3. Analysis of new bone formation in the rabbit release study by μCT. (A-C) Representative 2D images of femoral condyle plug defects treated with (A) ACS, (B) LV/CM, and (C) LV/S at 8 weeks. The dotted lines indicate the approximate edges of the defect and the scale bar represents 5 mm (D-G) Morphometric parameters evaluated by μCT: (D) BV/TV (vol%), (E) Tb.N. (mm), (F) Tb.Th. (mm-1), and (G) Tb.Sp. (mm).

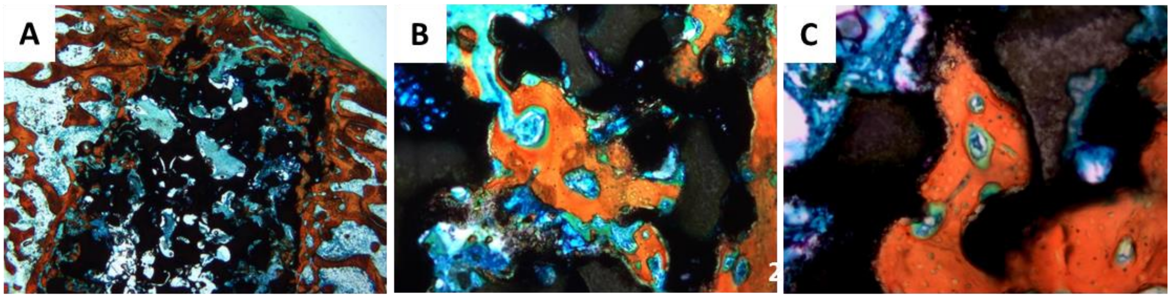

Figure 4.4. Representative images of histological sections of LV/CM. (A) 2X, (B) 10X, and (C) 20X. Red staining represents new bone, blue represents cells, and remaining polymer and CM particles stain black.

Discussion

The ACS carrier provides a bolus release of rhBMP-2 within the first week, which has prompted investigations of alternative release systems that provide a more sustained release of rhBMP-2 (36). Previous studies have reported that a more sustained release of rhBMP-2 enhances new bone formation compared to a bolus release at doses below that recommended for the ACS carrier (21,34). However, the release kinetics of rhBMP-2 from lysine-derived polyurethane bone grafts, which undergo both hydrolytic and cell-mediated oxidative degradation, have not been measured *in vivo*. In the present study, we measured the release kinetics of rhBMP-2 from two injectable, lysine-derived polyurethane scaffolds augmented with either fast-degrading sucrose (LV/S) or slow-degrading MASTERGRAFT® (LV/CM) particles to control expansion, porosity, and osteoconductivity. Both LV/S and LV/CM showed diffusion- and degradation-controlled release of rhBMP-2, in contrast to previous studies reporting diffusion-controlled release *in vitro* (20,28). While LV/S supported a burst and sustained release of rhBMP-2 compared to the burst release alone observed for ACS, both of these treatment groups supported minimal new bone formation at this lower dose (100 μg/ml rhBMP-2, or 25% of the recommended dose for the ACS carrier in rabbits (7)) at 8 weeks due to rapid degradation of the scaffold. In contrast, LV/CM treated defects showed a burst and sustained release of rhBMP-2 for 8 weeks and appositional new bone growth near the surface of the CM particles. These observations suggest that both an enduring matrix as well as sustained release of rhBMP-2 are required to promote bone healing at sub-optimal doses of rhBMP-2.

LV/CM composites were less porous than LV/S composites containing the soluble sucrose porogen. The addition of the ceramic matrix to LV/CM significantly increased the Young's modulus of the scaffold compared to LV/S, which is consistent with previous studies investigating polymer-ceramic composites (37). The high porosity of the LV/CM composites dilutes the concentration of ceramic particles to an approximate volume of 13 vol%, thus the increase in modulus may not be as high as expected considering the modulus of ceramics can reach 100 GPa (5).

In vitro degradation of lysine-derived polyurethane scaffolds was measured under oxidative conditions, resulting in complete degradation of the scaffold within 7-8 weeks. In contrast, under hydrolytic conditions these scaffolds exhibited much slower degradation, with mass loss measured over 25 weeks *in vitro* (8). Images of tissue sections of LV/CM-treated defects (Figure 4) reveal that the majority of the polymer had degraded by 8 weeks, which is in agreement with the *in vitro* oxidative degradation data (Figure 1D). Similarly, LV/S-treated defects showed essentially no residual polymer. These observations suggest that the *in vitro* model of oxidative degradation is a more accurate predictor of *in vivo* degradation of lysine-derived polyurethanes than the hydrolytic model.

The burst release profile observed for the ACS carrier corroborates previous studies showing a bolus release mechanism (38,39). The Weibull model fit shows that the release kinetics from the ACS carrier correspond to a combined release mechanism *in vivo*, most likely due to simultaneous diffusion and collagen degradation, and a complex release mechanism *in vitro*. A previous study has reported that the collagen sponge is completely degraded within 2 weeks *in vivo* (40). Despite the ~15% higher porosity of the LV/S group compared to LV/CM, both groups showed similar rhBMP-2 release kinetics *in vitro* and *in vivo*. It is conjectured that the 50% porosity of the LV/CM composites created a sufficiently interconnected pore structure such that the increased porosity of the LV/S composites did not significantly increase release. A previous study on small molecule release from hydrogels also showed no difference in release kinetics with an 11% change in porosity (41). Fickian diffusion was observed to control release of rhBMP-2 from LV/S and LV/CM composites *in vitro*, which is consistent with previous studies (28). In contrast, *in vivo* release is controlled by a combined release mechanism. One possibility for this difference in release kinetics is the accelerated degradation of the scaffold *in vivo* due to the transient inflammatory response and macrophage-mediated oxidative degradation, which has been previously described for lysine-derived polyurethanes (8). The increased degradation may create conditions under which *in vivo* release is controlled by both diffusion and scaffold degradation. These findings are consistent with the *in vitro* (Figure 1D) and *in vivo* (Figure 4) degradation data, which show nearly complete degradation of the lysine-derived polyurethane at 8 weeks.

Although release kinetics were similar between LV/CM and LV/S groups, the ceramic microparticles in the LV/CM composites contributed to more new bone formation at 8 weeks as measured by µCT and observed by histology. The LV/CM graft promoted increased new bone formation compared to the LV/S and ACS groups. With a substantially lower rhBMP-2 concentration in the grafts (100 µg/mL) than the recommended dose for the ACS carrier in rabbits (400 µg/mL), the extended release of rhBMP-2 from the LV/CM grafts contributed to more new bone and better remodeling than that observed the rapid (1 week) release from the ACS carrier. These results are similar to previous studies reporting that an initial burst followed by a sustained release is optimal for bone remodeling and healing (20,21). Additionally, the osteoconductive and slowly resorbing CM particles, even at a relatively low concentration of 13 vol% within the graft, provided a surface on which new bone could grow, which was not observed in either the LV/S or ACS samples due to the extensive degradation of the polyurethane (LV/S) and collagen (ACS) scaffolds.

Conclusion

In this study, we investigated the effects of rhBMP-2 delivery system and matrix content of LV composite bone grafts on rhBPM-2 release and new bone formation in a rabbit femoral plug model. LV grafts had an initial burst of rhBMP-2 followed by an extended release over a month, whereas the ACS control experienced a fast release within the first week. The addition of the ceramic matrix in the LV/CM composite led to more new bone and better healing than the LV/S or ACS control, as evidenced by radial µCT and histology. This work emphasizes the efficacy of a lower dose of rhBMP-2 when released from a polymer-ceramic composite and the importance of release mechanism elucidation for growth factor delivery systems of interest.

References

1. Borrelli, J, Prickett WD, Ricci WM. Treatment of Nonunions and Osseous Defects With Bone Graft and Calcium Sulfate: Clinical Orthopaedics and Related Research **411**, 245, 2003.
2. Yuan H, Fernandes H, Habibovic P, Boer J de, Barradas AMC, Ruiter A de, et al. Osteoinductive ceramics as a synthetic alternative to autologous bone grafting. PNAS **107**, 13614, 2010.
3. Bose S, Roy M, Bandyopadhyay A. Recent advances in bone tissue engineering scaffolds. Trends in Biotechnology **30**, 546, 2012.
4. Scaglione S, Lazzarini E, Ilengo C, Quarto R. A composite material model for improved bone formation. J Tissue Eng Regen Med **4**, 505, 2010.
5. Rezwan K, Chen QZ, Blaker JJ, Boccaccini AR. Biodegradable and bioactive porous polymer/inorganic composite scaffolds for bone tissue engineering. Biomaterials **27**, 3413, 2006.
6. Bonzani IC, Adhikari R, Houshyar S, Mayadunne R, Gunatillake P, Stevens MM. Synthesis of two-component injectable polyurethanes for bone tissue engineering. Biomaterials **28**, 423, 2007.
7. Dumas JE, BrownBaer PB, Prieto EM, Guda T, Hale RG, Wenke JC, et al. Injectable reactive biocomposites for bone healing in critical-size rabbit calvarial defects. Biomed. Mater **7**, 024112, 2012.
8. Hafeman AE, Zienkiewicz KJ, Zachman AL, Sung H-J, Nanney LB, Davidson JM, et al. Characterization of the degradation mechanisms of lysine-derived aliphatic poly(ester urethane) scaffolds. Biomaterials **32**, 419, 2011.
9. Zhang J-Y, Beckman EJ, Hu J, Yang G-G, Agarwal S, Hollinger JO. Synthesis, Biodegradability, and Biocompatibility of Lysine Diisocyanate–Glucose Polymers. Tissue Engineering **8**, 771, 2002.
10. Dumas JE, Prieto EM, Zienkiewicz KJ, Guda T, Wenke JC, Bible J, et al. Balancing the Rates of New Bone Formation and Polymer Degradation Enhances Healing of Weight-Bearing Allograft/Polyurethane Composites in Rabbit Femoral Defects. Tissue Engineering Part A **20**, 115, 2013.
11. Bohner M, Galea L, Doebelin N. Calcium phosphate bone graft substitutes: Failures and hopes. Journal of the European Ceramic Society **32**, 2663, 2012.
12. Laurencin CT, Attawia MA, Lu LQ, Borden MD, Lu HH, Gorum WJ, et al. Poly(lactide-co-glycolide)/hydroxyapatite delivery of BMP-2-producing cells: a regional gene therapy approach to bone regeneration. Biomaterials **22**, 1271, 2001.
13. Habraken WJEM, Wolke JGC, Jansen JA. Ceramic composites as matrices and scaffolds for drug delivery in tissue engineering. Advanced Drug Delivery Reviews **59**, 234, 2007.
14. Dimitriou R, Jones E, McGonagle D, Giannoudis PV. Bone regeneration: current concepts and future directions. BMC Medicine **9**, 66, 2011.
15. Bose S, Tarafder S. Calcium phosphate ceramic systems in growth factor and drug delivery for bone tissue engineering: A review. Acta Biomaterialia **8**, 1401, 2012.
16. Kimura Y, Miyazaki N, Hayashi N, Otsuru S, Tamai K, Kaneda Y, et al. Controlled Release of Bone Morphogenetic Protein-2 Enhances Recruitment of Osteogenic Progenitor Cells for *De Novo* Generation of Bone Tissue. Tissue Engineering Part A **16**, 1263, 2010.
17. Bhakta G, Lim ZXH, Rai B, Lin T, Hui JH, Prestwich GD, et al. The influence of collagen and hyaluronan matrices on the delivery and bioactivity of bone morphogenetic protein-2 and ectopic bone formation. Acta Biomaterialia **9**, 9098, 2013.
18. Lee J, Susin C, Rodriguez NA, De Stefano J, Prasad HS, Buxton AN, et al. Sinus

augmentation using rhBMP-2/ACS in a mini-pig model: relative efficacy of autogenous fresh particulate iliac bone grafts. Clinical Oral Implants Research **24**, 497, 2013.
19. Shen H, Hu X, Yang F, Bei J, Wang S. An injectable scaffold: rhBMP-2-loaded poly(lactide-co-glycolide)/hydroxyapatite composite microspheres. Acta Biomaterialia **6**, 455, 2010.
20. Brown KV, Li B, Guda T, Perrien DS, Guelcher SA, Wenke JC. Improving Bone Formation in a Rat Femur Segmental Defect by Controlling Bone Morphogenetic Protein-2 Release. Tissue Engineering Part A **17**, 1735, 2011.
21. Boerckel JD, Kolambkar YM, Dupont KM, Uhrig BA, Phelps EA, Stevens HY, et al. Effects of protein dose and delivery system on BMP-mediated bone regeneration. Biomaterials **32**, 5241, 2011.
22. Amini AR, Adams DJ, Laurencin CT, Nukavarapu SP. Optimally Porous and Biomechanically Compatible Scaffolds for Large-Area Bone Regeneration. Tissue Engineering Part A **18**, 1376, 2012.
23. Hing KA, Best SM, Tanner KE, Bonfield W, Revell PA. Mediation of bone ingrowth in porous hydroxyapatite bone graft substitutes. J. Biomed. Mater. Res. **68A**, 187, 2004.
24. Kempen DHR, Lu L, Hefferan TE, Creemers LB, Maran A, Classic KL, et al. Retention of in vitro and in vivo BMP-2 bioactivities in sustained delivery vehicles for bone tissue engineering. Biomaterials **29**, 3245, 2008.
25. Jeon O, Song SJ, Kang S-W, Putnam AJ, Kim B-S. Enhancement of ectopic bone formation by bone morphogenetic protein-2 released from a heparin-conjugated poly(l-lactic-co-glycolic acid) scaffold. Biomaterials **28**, 2763, 2007.
26. Artzi N, Oliva N, Puron C, Shitreet S, Artzi S, Bon Ramos A, et al. In vivo and in vitro tracking of erosion in biodegradable materials using non-invasive fluorescence imaging. Nat Mater **10**, 2011.
27. Wöhl-Bruhn S, Badar M, Bertz A, Tiersch B, Koetz J, Menzel H, et al. Comparison of in vitro and in vivo protein release from hydrogel systems. Journal of Controlled Release **162**, 127, 2012.
28. Li B, Yoshii T, Hafeman AE, Nyman JS, Wenke JC, Guelcher SA. The effects of rhBMP-2 released from biodegradable polyurethane/microsphere composite scaffolds on new bone formation in rat femora. Biomaterials **30**, 6768, 2009.
29. Guelcher SA, Patel V, Gallagher KM, Connolly S, Didier JE, Doctor JS, et al. Synthesis and In Vitro Biocompatibility of Injectable Polyurethane Foam Scaffolds. Tissue Engineering **12**, 1247, 2006.
30. Guelcher S, Srinivasan A, Hafeman A, Gallagher K, Doctor J, Khetan S, et al. Synthesis, In Vitro Degradation, and Mechanical Properties of Two-Component Poly(Ester Urethane)Urea Scaffolds: Effects of Water and Polyol Composition. Tissue Engineering **13**, 2321, 2007.
31. Christenson EM, Anderson JM, Hiltner A. Oxidative mechanisms of poly(carbonate urethane) and poly(ether urethane) biodegradation:In vivo andin vitro correlations. Journal of Biomedical Materials Research **70A**, 245, 2004.
32. Martin JR, Gupta MK, Page JM, Yu F, Davidson JM, Guelcher SA, et al. A porous tissue engineering scaffold selectively degraded by cell-generated reactive oxygen species. Biomaterials **35**, 3766, 2014.
33. Papadopoulou V, Kosmidis K, Vlachou M, Macheras P. On the use of the Weibull function for the discernment of drug release mechanisms. International Journal of Pharmaceutics **309**, 44, 2006.
34. Li B, Brown KV, Wenke JC, Guelcher SA. Sustained release of vancomycin from

polyurethane scaffolds inhibits infection of bone wounds in a rat femoral segmental defect model. Journal of Controlled Release **145**, 221, 2010.
35. Bouxsein ML, Boyd SK, Christiansen BA, Guldberg RE, Jepsen KJ, Müller R. Guidelines for assessment of bone microstructure in rodents using micro–computed tomography. Journal of Bone and Mineral Research **25**, 1468, 2010.
36. Luginbuehl V, Meinel L, Merkle HP, Gander B. Localized delivery of growth factors for bone repair. European Journal of Pharmaceutics and Biopharmaceutics **58**, 197, 2004.
37. Mathieu LM, Mueller TL, Bourban P-E, Pioletti DP, Müller R, Månson J-AE. Architecture and properties of anisotropic polymer composite scaffolds for bone tissue engineering. Biomaterials **27**, 905, 2006.
38. Uludag H, Gao T, Porter TJ, Friess W, Wozney JM. Delivery Systems for BMPs: Factors Contributing to Protein Retention at an Application Site. The Journal of Bone & Joint Surgery **83**, S128, 2001.
39. Seeherman H, Wozney JM. Delivery of bone morphogenetic proteins for orthopedic tissue regeneration. Cytokine & Growth Factor Reviews **16**, 329, 2005.
40. Kroese-Deutman HC, Ruhé PQ, Spauwen PHM, Jansen JA. Bone inductive properties of rhBMP-2 loaded porous calcium phosphate cement implants inserted at an ectopic site in rabbits. Biomaterials **26**, 1131, 2005.
41. Bettini R, Colombo P, Massimo G, Catellani PL, Vitali T. Swelling and drug release in hydrogel matrices: polymer viscosity and matrix porosity effects. European Journal of Pharmaceutical Science **2**, 213, 1994.

CHAPTER V

EFFECTS OF rhBMP-2 DOSE AND CERAMIC COMPOSITION ON NEW BONE FORMATION AND SPACE MAINTENANCE IN A CANINE MANDIBULAR RIDGE SADDLE DEFECT MODEL

Introduction

Treatment of alveolar ridge atrophy and large ridge defects poses significant clinical challenges, which are compounded by the need to restore form and function through placement of dental implants. Implant surgery requires height and width of the alveolar ridge to support dental implants and restore normal dentition. A variety of bone grafts can be used to promote lateral ridge augmentation, including allogenic or autogenic bone, recombinant human growth factors, osteoconductive scaffolds, and guided bone regeneration (GBR) using degradable or non-degradable membranes (1). However, these approaches are limited by unpredictable host bone or graft resorption, exposure of the bone graft or membrane leading to infection, and the necessity of additional surgical sites (2). Thus, there is considerable interest in tissue engineering approaches to repair alveolar defects with the long-term goal of producing functional grafts that support simultaneous dental implant placement.

Synthetic substitutes for bone grafting include ceramics and bioactive glasses. Ceramics such as tricalcium phosphate (TCP) and hydroxyapatite (HA) have been used extensively in bone grafting for a variety of applications (3). Bioactive glasses stimulate bone regeneration due to ion dissolution and surface bonding with bone, and the original 45S5 Bioglass® has been used in more than a million patients for bone defect repair in craniomaxillofacial (CMF) and orthopedic applications (4). Both ceramics and bioactive glasses are often combined with polymers to enhance their mechanical and handling properties (5). Injectable and biodegradable lysine-derived polyurethane (PUR) scaffolds have been extensively investigated in bone regeneration applications (6, 7). When tested in femoral plug defects in rabbits, PUR/ceramic composites supported local, sustained delivery of recombinant human bone morphogenetic protein-2 (rhBMP-2) leading to cellular infiltration and new bone formation. The mechanical properties of PUR/ceramic composites can be tuned by varying the crosslink density of the polymer phase, making them suitable even for weight-bearing applications (8, 9).

Local delivery of synthetic growth factors has been reported to enhance healing of CMF bone defects (10). Delivery of rhBMP-2, an osteoinductive factor that stimulates osteoblast differentiation and new bone formation, from an absorbable collagen sponge (ACS) is FDA-approved for localized alveolar ridge augmentation and sinus lift procedures. Previous studies have demonstrated the efficacy of rhBMP-2 in preclinical calvarial defect models in rats (11-13) and rabbits (7, 14), preclinical lateral ridge augmentation models in dogs and non-human primates (15, 16), and in alveolar ridge augmentation in humans (17).

Bone grafting is often combined with GBR to maintain the anatomic contour and height of the alveolar ridge height. GBR requires placement of a resorbable or non-resorbable barrier membrane around the graft to prevent soft tissue prolapse and stabilize the graft (18-20). However, the GBR approach is limited by complications including wound failure, seromas, and infection, as well as the potential need for a secondary surgery to remove the membrane (21-23). Due to inconsistent outcomes and limitations associated with GBR, it is desirable to find a bone graft that does not require the use of membranes to maintain the defect volume during bone remodeling. In this study, we investigated injectable low-viscosity (LV) PUR/ceramic composites augmented with 100 μg/ml (low) or 400 μg/ml (high) rhBMP-2 as space-maintaining bone grafts in a canine ridge saddle defect model. LV grafts were injected as a reactive paste that set in 5 – 10 minutes to form a solid porous composite with bulk modulus exceeding 1 MPa. We hypothesized that LV grafts would enhance new bone formation and maintain space without the use of protective membranes, and that a more slowly degrading ceramic matrix would more effectively maintain the mandibular ridge height and width.

Experimental

Materials. Lysine-triisocyanate prepolymer (LTI-PEG, 21.7% NCO) was purchased from Ricerca Biosciences LLC (Painesville, OH). Glycerol, stannous octoate, ε-caprolactone, and APTES were purchased from Sigma-Aldrich (St. Louis, MO). Glycolide and DL-lactide were supplied by Polysciences (Warrington, PA). Triethylene diamine (TEDA) and dipropylene glycol (DPG) were purchased from Sigma Aldrich and mixed to obtain a 10% (w/w) solution of TEDA in dry DPG. MASTERGRAFT® Mini Granules (ceramic, CM) were received from Medtronic Spinal. (Memphis, TN). 45S5 bioactive glass (BG) particles (150 – 212 µm) were purchased from Mo-Sci Corporation (Rolla, MO). Recombinant human bone morphogenetic protein-2 (rhBMP-2) was received from Medtronic Spinal (Memphis, TN).

Synthesis of polyester triol. The polyester triol was synthesized as described previously (25, 26). Briefly, glycerol was mixed with ε-caprolactone, glycolide, and DL-lactide monomers under argon at 140°C for 40 hrs. The resulting polyester triol was cooled, washed with hexane, and vacuum-dried at 80°C. The backbone of the polyester consisted of 70% ε-caprolactone, 20% glycolide, and 10% DL-lactide, and the molecular weight was 450 g mol^{-1}.

Surface modification of bioactive glass. The surface of the bioactive glass particles was modified as described previously to ensure adequate interfacial bonding and mechanical properties (10, 27-29). Briefly, melt-derived 45S5 BG particles were cleaned via sonication in acetone in deionized (DI) water (95 vol%) and subsequently sonicated three times in DI water to rinse the particles. Next, particles were silanized via a solution of APTES for 5 h at room temperature, rinsed with ethanol, and annealed at 100 °C for 1 h. For surface-initiated ring-opening polymerization, a mixture comprising a 1:1000 M ratio of Sn(Oct)2: dried ε-caprolactone and a 0.83:1 weight ratio of Sil-BG:ε-caprolactone was reacted while stirring at 110 °C. The polymerization time of 24 hrs corresponded to a final poly(ε-caprolactone) (PCL) molecular weight of 19,225 g mol^{-1}. Finally, non-grafted PCL was extracted with chloroform and particles were dried at 40 °C for 24 h.

Fabrication of low-viscosity (LV) bone grafts. CM granules were ground and sieved to 100-500 μm. The components of the LV grafts were mixed in a two-step method. In the first step, the polyester triol, particles (either 45 wt% CM or 45 wt% BG), and TEDA (1.1 pphp) were added to a 10-mL cup and mixed by hand for 30 s. The LTI-PEG and lyophilized rhBMP-2 were added to the cup and mixed by hand for 60 s. The index (ratio of isocyanate:hydroxide equivalents x 100) was 115. For material characterization, the reactive mixture was mixed with 3 pphp of DI water (to simulate *in vivo* curing in the presence of moisture), loaded into a straight bore syringe, and injected into a 6-mm vial. These samples were allowed to cure for 24 h prior to cutting.

Characterization of physical and mechanical properties. Composite bone grafts were cut into sections, mounted onto a scanning electron microscopy (SEM) pin stub mount, and sputter-coated for 40 s using a Cressington Q108 sputter coater, which deposited gold at a 30 mA current. A Hitachi S-4200 SEM was used to acquire images at a voltage of 1kV. Images (n=3 per formulation) were analyzed for pore size using ImageJ 1.47p image analysis software. Cylindrical samples with 6 mm diameter and lengths of approximately 12 mm were prepared with porosities of approximately 50% (measured gravimetrically). Samples were submerged in phosphate-buffered saline for 24 h prior to mechanical testing. Compression testing was performed using an MTS 898 Bionix system (Eden Prairie, MN) with a 1kN load cell. Samples were preloaded to 3N and compressed at a constant rate of 25 mm/min. The original cross sectional area of the cylinders was used to calculate compressive stress. The compressive strength was reported at sample failure, and the bulk (compressive) modulus was calculated as the slope of the initial linear portion of the stress-strain curve. Porosity, pore size, and compression data are presented as mean ± standard deviation of triplicate samples.

Table 5.1. Treatment groups evaluated in the canine mandibular ridge saddle defects.

Treatment Group	Particles	Particle diameter (μm)	rhBMP-2 (μg cm-3 defect volume)	n 16 weeks
LV/BG-L	Bioactive glass	150 - 212	100	6
LV/BG-H	Bioactive glass	150 - 212	400	6
LV/CM-L	Mastergraft	100-500	100	6
LV/CM-H	Mastergraft	100 - 500	400	6

Evaluation of LV bone grafts in a canine mandibular ridge saddle defect model. Six skeletally mature hounds were used in this study. All surgical and care procedures were carried out under aseptic conditions according to the approved IACUC protocol. Treatment groups are listed in Table 5.1. The individual components of the LV grafts were gamma-irradiated using a dose of 25 kGY. In the first surgery, the dogs underwent bilateral extraction of the four mandibular premolars and first molar (Figure 5.1A). After at least a two-month healing period, a second surgery was performed to create two saddle defects bilaterally in each mandible (4 defects per dog) measuring approximately 7-10 mm mesiodistally, 6-8 mm apico-coronally, and 8-10 mm bucco-lingually (Figure 5.1B). A soft tissue pocket was created by stitching the gingiva on the mesiodistal boundaries of the defect (Figure 5.1C). The LV bone grafts were mixed with rhBMP-2 and injected into the soft tissue pocket at the defect site (Figure 5.1D) and allowed to cure for 10 min prior to soft tissue closure (Figure 5.1E). Defects were filled with LV/CM or LV/BG at a low (100 µg/ml) or a high (400 µg/ml) dose of rhBMP-2 (n=6 per group). The dogs were euthanized after sixteen weeks. The mandibles were extracted (Figure 5.1F) and fixed in 10% formalin for two weeks prior to processing for histology.

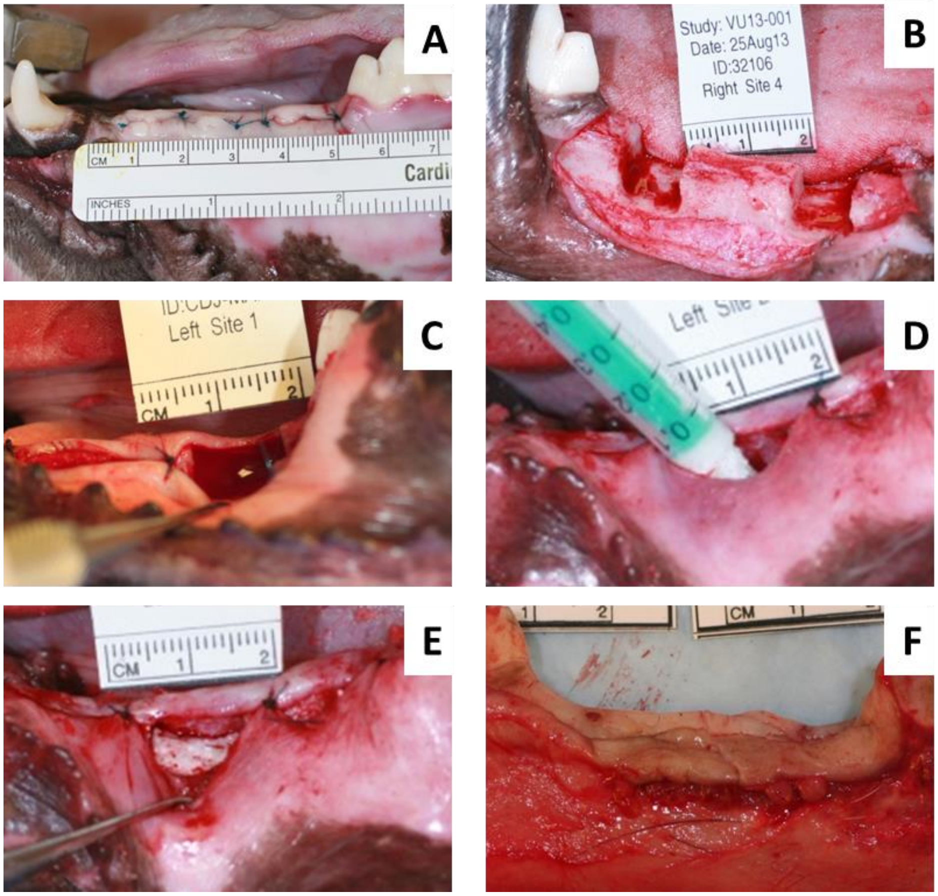

Figure 5.1. Surgical photographs of saddle defect creation. (A) Tooth extraction surgery. (B) Second surgery to create the saddle defect in the mandibular ridge. (C) Creation of a soft tissue pocket around defect site. (D) Injection of LV grafts in the saddle defects. (E) LV graft after the polyurethane reaction. (F) Mandibular ridge following canine sacrifice and bone extraction.

Analysis of bone morphometry by Micro-Computed Tomography (µCT). A µCT50 (SCANO Medical, Basserdorf Switzerland) was used to acquire scans of the extracted mandibles in formalin at 70 kVp energy, 200 µA source current, 1000 projections per rotation, 800 ms integration time, and an isotropic voxel size of 24.2 µm. Axial images were reconstituted using manufacturer provided software. Attenuation values were converted to tissue mineral density (TMD) through calibration with hydroxyapatite (HA) phantoms with densities of 0 to 780 mg HA cm^{-3} (calibrations checked weekly). Using the coronal boundary of the defect for alignment, the reconstructed image stack was re-oriented so that the apico-coronal direction was parallel to the z-axis. Ridge width in the defect (bucco-lingual direction) was measured at 2 mm intervals up to a total distance of 6 mm from the coronal base of the defect. Ridge width within the defect area was normalized to host bone ridge width on either side of the defect. Maximum ridge height (apico-coronal direction) was measured at the mesiodistal center of the defect for each sample. Morphometric parameters were measured in a region of interest measuring 10 mm (mesiodistally) by 3 mm (bucco-lingually) by 3 mm (apico-coronally). Ossified tissue was segmented from soft tissue using the lower and upper threshold of 240 $mgHAcm^{-3}$ and 1000 $mgHAcm^{-3}$, respectively, with a Gaussian noise filter settings of sigma 0.7 and support 2. Bone volume/total volume (BV/TV), trabecular number (TB.N.), trabecular thickness (Tb.Th.), and trabecular separation (Tb.Sp.) within the regions of interest were computed using SCANCO's Medical microCT systems software as described previously (30).

Histology. After fixation in formalin, the explanted mandibles were dehydrated in a graded series of ethanol and embedded in poly(methylmethacrylate) (PMMA). Using an Exakt band saw, sections were cut from each block in the center of the defect (bucco-lingually) using the µCT images as reference. The sections were then ground and polished to <100 µm using an Exakt grinding system and stained with Sanderson's rapid bone stain. New bone stained red, residual CM stained black, and infiltrating cells stained blue. Residual BG particles appeared white and did not absorb the stain. Histological sections were used to measure the maximum ridge height within the defect area similar to a method previously reported (31) used for the µCT 2D sections. Measurements of the maximum ridge height (highest point within the defect area) were taken using Metamorph software (Version 7.0.1, Waltham, MA). Values of maximum ridge height by both methods were plotted together for each group.

Statistical analysis. Differences in porosity, modulus, and yield strength between groups were tested for statistical significance by unpaired Student's t-tests. Maximum ridge height, by µCT, was analyzed by one-way ANOVA. Morphometric parameters, including BV/TV, Tb.N., Tb.Th, and Tb.Sp, were tested by one-way ANOVA. A two-way ANOVA was run to test significance of normalized ridge width data comparing among means of each group at the different vertical positions. To compare maximum ridge heights measured from µCT and histological sections, a Bland-Altman plot was constructed, in which the average value for each group is plotted against the difference between methods. Statistical significance was considered for $p < 0.05$.

Results

Composite characterization. Physical and mechanical properties of LV grafts are summarized in Table 5.2. Both LV/CM and LV/BG grafts exhibited initial porosities of 48 – 52%, which are comparable to values reported previously for allograft bone (32, 33) and ceramic composites (8). Representative SEM images (Figure 5.2) show the morphology of the pores in the grafts. The ceramic particles are embedded in the polyurethane network for both LV/BG and LV/CM composites. The average pore diameter was significantly higher for LV/CM composites

(100.1 ± 1.2 μm) compared to LV/BG composites (88.6 ± 2.2 μm). The modulus of LV/CM composites (3.1 ± 0.4 MPa) was significantly higher than that of LV/BG composites (1.2 ± 0.1 MPa, Table 5.2). Additionally, the yield strain at failure was significantly higher for LV/BG composites (27.4 ± 5.2 %) when compared to LV/CM composites (16.5 ± 4.2 %). In contrast, there were no significant differences in compressive yield strength of LV/CM (0.38 ± 0.05 MPa) and LV/BG (0.37 ± 0.03 MPa) composites.

Table 5.2. Physical and mechanical properties of LV composites tested in the canine saddle defect.

Treatment Group	Porosity (%)	Pore diameter (μm)	Bulk Modulus (MPa)	Yield Strength (MPa)	Yield Strain (%)
LV/BG	52.4 ± 0.3	88.6 ± 2.2[a]	1.2 ± 0.1[a]	0.37 ± 0.03	27.4 ± 5.2[a]
LV/CM	48.0 ± 3.0	100.1 ± 1.2	3.1 ± 0.4	0.38 ± 0.05	16.5 ± 4.2

[a] statistically different with $p < 0.05$

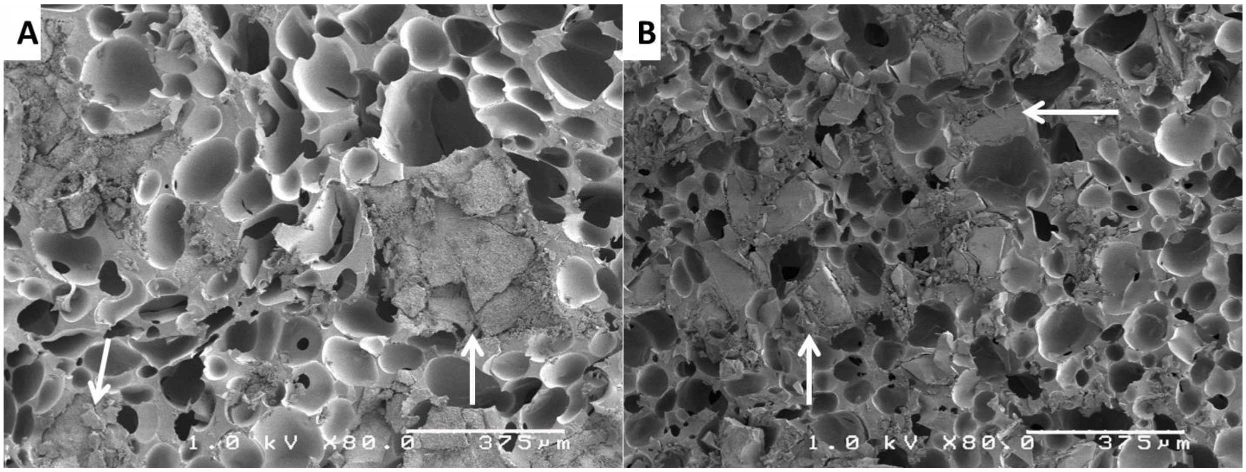

Figure 5.2. SEM images of (A) LV/CM and (B) LV/BG composite bone grafts. White arrows point to matrix particles embedded within the PUR scaffold.

μCT analysis. Representative 2D μCT images of axial and longitudinal cross-sections of all treatment groups are presented in Figure 5.3. New bone is visible in the defect site for all treatment groups. Defects treated with LV/BG-L and LV/CM-L groups demonstrated less new bone and lower ridge heights than the equivalent high dose groups. In the LV/CM samples, residual CM particles are dispersed throughout the new bone (bright white particles), whereas residual bioactive glass cannot be distinguished from new bone in the LV/BG samples. Ridge width at the mesiodistal center of the defect was measured at 2, 4, and 6 mm above the baseline of the defect (Figure 5.3C) from 2D sections in the transverse plane (Figure 5.3D). The normalized ridge width was calculated by dividing the width measured at the center of the defect (dashed white line in Figure 5.3D) by the average width of the host bone in the ridge (solid white lines in Figure 5.3D) and plotted versus height above the baseline (Figure 5.4A). For defects treated with the low dose of rhBMP-2, normalized ridge width decreased with increasing ridge height. In contrast, defects treated with the high dose of rhBMP-2 maintained ridge width comparable to that of the host bone with increasing ridge height up to 6 mm above the defect baseline. At 4 mm above the base of the defect, the LV/CM-H group showed significantly greater ridge width compared to LV/BG-L. At 6 mm above the base of the defect, both high-dose treatment groups displayed significantly greater normalized ridge widths compared to the low-dose groups. Maximum ridge heights were also measured at the mesiodistal center of the defect from axial (coronal plane) sections as illustrated in Figure 5.3E. The high dose treatment groups showed significantly higher maximum ridge heights compared to the low dose groups (Figure 5.4B). There were no significant differences between LV/CM-L and LV/BG-L groups or between LV/CM-H and LV/BG-H groups. Morphometric parameters were also analyzed to assess the quality of the new bone within the defect site (Figure 5.4C-F). There were no significant differences in BV/TV, Tb.N., Tb.Th., or Tb.Sp. between groups.

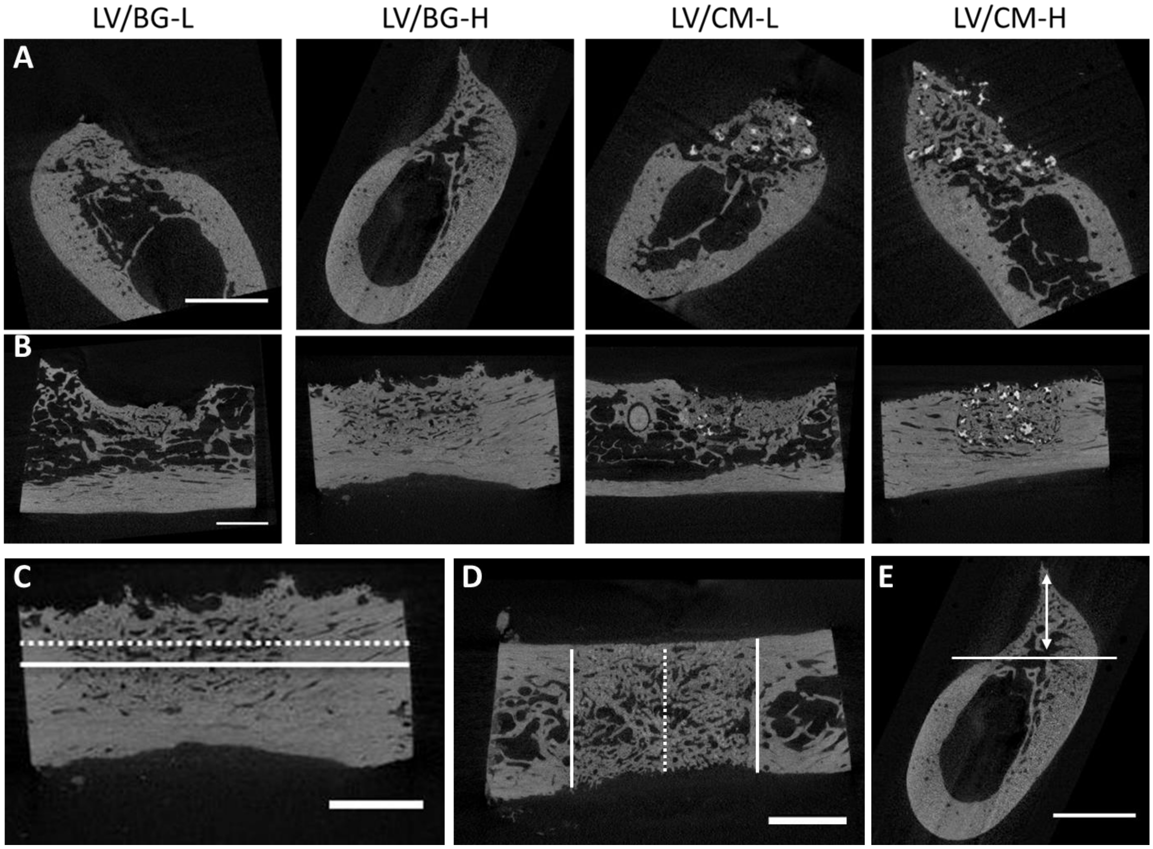

Figure 5.3. µCT analysis of saddle defects after 16 weeks. (A) Representative 2D images of axial (coronal plane) cross-sections. (B) Representative 2D images of longitudinal (sagittal plane) cross-sections. (C) Schematic illustrating measurement of ridge width from a 2D longitudinal cross-section at 2 mm (solid line) and 4 mm (dotted line) above the base of the defect. (D) Schematic illustrating measurement of ridge width from a 2D transverse-plane cross-section. Normalized ridge width was calculated as the width measured at the mesiodistal center of the defect (dashed white line) divided by the average width of the host bone bone (solid white lines). Measurements were taken at heights 2, 4, and 6 mm above the base of the defect (shown in Panel C). (E) Representative image depicting measurement of the maximum ridge height in 2D longitudinal sections at the mesiodistal center of the defect. The solid line shows the base of the defect and the double arrow represents the maximum ridge height. The scale bar denotes 5 mm.

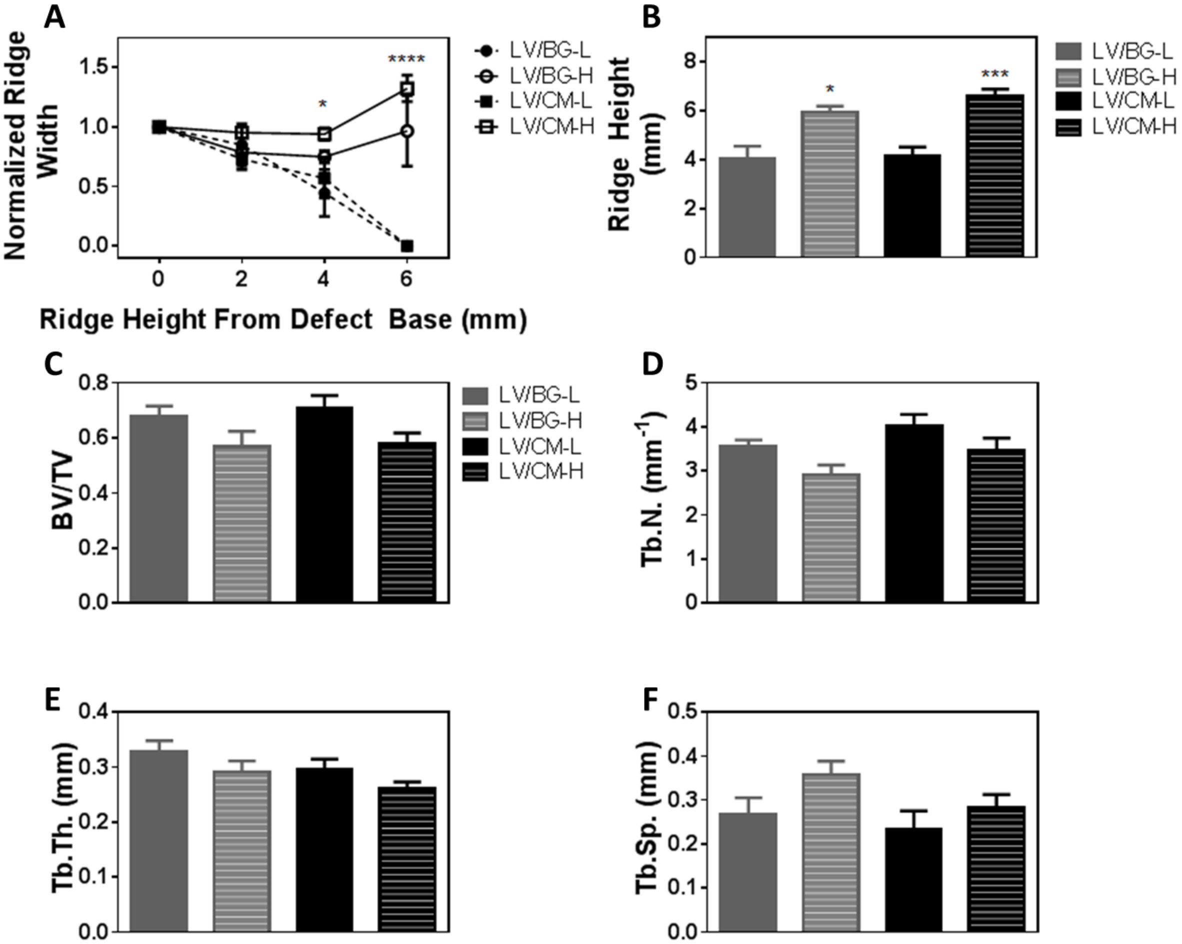

Figure 5.4. Quantitative analysis of space maintenance and new bone formation by µCT. (A) Normalized ridge width measured at the mesiodistal center of the defect as a function of height above the baseline of the defect. The LV/CM-H group was significantly different from LV/BG-L at 4 mm above the base of the defect ($p < 0.05$). The high-dose treatments were significantly different from low-dose treatments at 6 mm above the base of the defect ($p < 0.0001$) (B) Maximum ridge height measured at the mesiodistal center of the defect. Significant differences between low- and high- dose groups are denoted by (*) $p < 0.05$ and (***) $p < 0.001$. No significant differences between LV/BG-L and LV/CM-L or between LV/CM-L and LV/CM-H were observed. (C-F) Morphometric parameters measured from µCT images: (C) BV/TV, (D) Tb.N., (E) Tb.Th, (F) Tb.Sp. No significant differences in morphometric parameters were observed between groups.

Histology. Figure 5.5 shows representative low- and high-magnification images of histological sections for all treatment groups. With Sanderson's rapid bone stain, new bone appears red, cells are blue, and residual CM particles appear black. BG particles do not stain and appear white or grey. No residual polymer was observed in any of the sections, suggesting that it had completely degraded by 16 weeks. Similar to the µCT images (Figure 5.3), the histological sections showed more new bone formation in the high dose groups (Figure 5.5A). Few BG particles were observed, suggesting that the BG had been substantially resorbed by 16 months. In contrast, residual CM particles were observed within the defect site for the LV/CM groups. Appositional new bone growth was observed near the surface of the CM particles, suggesting that the matrix functioned as a scaffold for bone formation. Residual ceramic particles were embedded in new bone. Osteoid was also observed near the ceramic/bone interface, providing evidence of active remodeling. Ridge height in the defect area was measured from histological sections and compared to the same data obtained from µCT (Figure 5.5B). The high-dose treatment groups exhibited significantly higher ridge heights compared to the low-dose groups for both µCT and histomorphometric methods. The Bland-Altman plot, which tests for differences between the µCT and histomorphometric measurements as a function of sample mean, shows no global differences between approaches within a 95% confidence interval (Figure 5.5C).

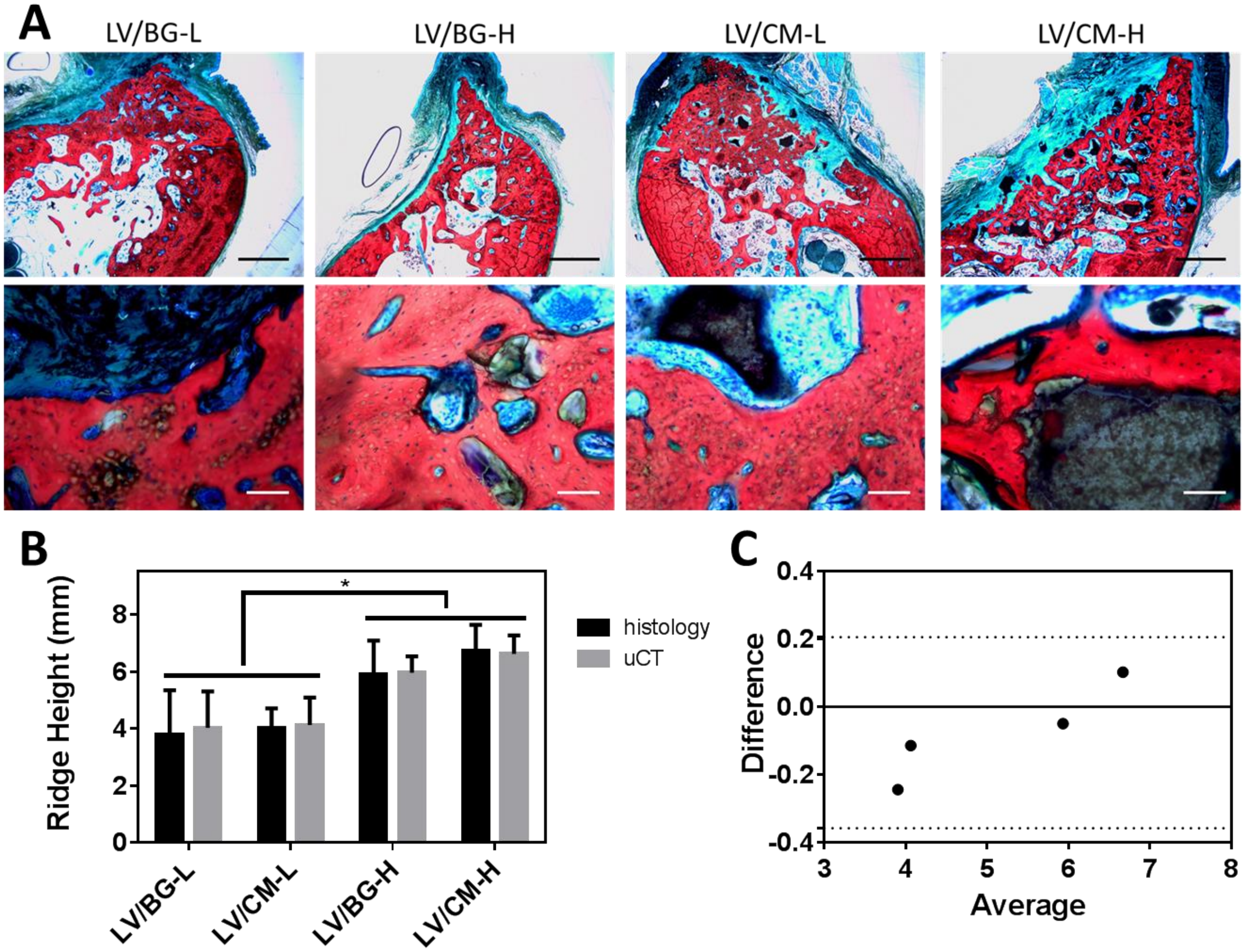

Figure 5.5. Histological analysis of new bone formation and space maintenance. (A) Low- (1.25x, top row) and high- (10x, bottom row) magnification images of histological sections show new bone formation (NB, red), infiltrating cells (blue), and osteoid (O) with residual CM (black) or BG (clear) particles. No residual polymer was observed. (B) Comparison of ridge height measured at the mesiodistal center of the defect from histological sections (black bars) and from 2D μCT images (grey bars). Significant differences between low- and high- dose groups are denoted by (*) $p < 0.05$ and (***) $p < 0.001$. (C) Bland-Altman plot shows no significant differences between the histological and μCT measurements of ridge height with a 95% confidence interval (dotted lines).

Discussion

Ridge augmentation is a significant clinical challenge. Regeneration of alveolar bone is often required prior to implant placement in patients facing bone atrophy, tooth loss, or trauma, but there is no clinical standard of care for vertical ridge augmentation in patients. Previous studies have investigated GBR as a strategy for maintaining the volume of the bone defect and promoting new bone formation in vertical ridge augmentation models, but results from these studies have proven to be inconsistent and complications have been reported, including wound failure, seroma, and graft exposure leading to infection (21-23, 34). In the present study, we hypothesized that injectable and settable bone grafts with bulk moduli exceeding that of the soft tissue would maintain space and support bone healing without the use of protective membranes. We found that LV grafts augmented with 400 μg/ml rhBMP-2 and initial bulk modulus exceeding 1.2 MPa maintained the initial width and height of the alveolar ridge, while the anatomic contour was not preserved at the low (100 μg/ml) dose.

In order to design compression-resistant grafts for ridge augmentation, it is important to know the critical bulk modulus of the graft required to maintain the anatomic contour of the ridge (35, 36). A recent study reported that an ACS carrier coated with poly(D,L-lactic-*co*-glycolic acid) maintained the contour ridge of the ridge and promoted new bone formation at an rhBMP-2 dose of 400 μg/ml dose (37). However, the mechanical properties for this scaffold have not been reported. In the present study, both LV/BG (1.2 MPa) and LV/CM (3.1 MPa) composites maintained both the height and width of the mandibular ridge at the 400 μg/ml dose. The tensile and stress relaxation properties of porcine oral soft tissue have been recently characterized (36, 38). The Young's modulus of lingual and buccal attached gingiva ranges from 18.8 – 19.8 MPa, and the tensile strength ranges from 2.8 – 3.9 MPa (36). These values are approximately one order of magnitude greater than those measured for LV grafts. GBR membranes, including chitosan (13 – 55 MPa) (39), poly(trimethylene carbonate) (5 – 7 MPa) (40), calcium sulfate/poly(β-amino ester) gels (100 – 400 MPa) (41), and starch/poly-ε-caprolactone scaffolds (34 – 45 MPa) (42), generally have moduli comparable to or exceeding that of human gingiva. The membranes protect the absorbable collagen sponge (ACS), which has a Young's modulus of <0.1MPa (35, 43), against compression by the adjacent tissue (44). Addition of ceramic particles to the ACS carrier maintained space and promoted new bone formation in porcine full-thickness mandibular defects without the protective titanium crib (44). While the mechanical properties of the ceramic/collagen composite were not reported, a recent study has shown that addition of up to 80% hydroxyapatite to collagen scaffolds increases the bulk modulus to ~1 MPa (43). These observations point to an initial bulk modulus of ~1 MPa as the lower limit for compression-resistant grafts in the mandibular ridge.

The effects of the composition of the ceramic particles on space maintenance and new bone formation in the mandibular ridge saddle defect model were also investigated. Two FDA-cleared synthetic ceramic bone graft substitutes were tested in this study: MASTERGRAFT® Mini Granules (CM) and 45S5 Bioglass® (BG) particles. CM particles were evaluated due to their compression-resistant and osteoconductive qualities when combined with the ACS carrier and rhBMP-2 in porcine mandibular continuity defects (44) and in posterolateral fusion both in non-human primates (45) and humans (46) Residual CM particles were present in the defect at 16 weeks, some of which were in the process of active remodeling with new bone growth appositional to the surface. These observations are consistent with a previous study evaluating CM/collagen composites augmented with rhBMP-2 in mandibular continuity defects in nonhuman primates (44). In this study, a significant amount of residual CM was present at 6 months, most of which was in the process of active remodeling (44). In contrast, minimal residual BG particles were present in the defect at 16 weeks (Figure 5A) due to both the rapid resorption of BG particles by osteoclasts (47) and the dissolution products that stimulate osteoprogenitor cells (4). Defects treated with LV/CM-H composites showed a modest increase in ridge width at 4 and 6 mm above the defect compared to LV/BG-H (Figure 4A). However, no significant differences in ridge height measured in the middle of the defect were observed between the two groups (Figure 5B-C). The modest differences in ridge width could result from differences in the initial bulk modulus of the composites and/or the degradation rate of the ceramic components.

While the ceramic composition exhibited a modest effect on new bone formation and space maintenance, the concentration of rhBMP-2 affected new bone formation in a dose-responsive manner. The high dose of rhBMP-2 was selected on the basis that it is at the high end of the recommended dose range for dogs (200 – 400 μg/ml) (48). The ridge height at the center of the defect was ≥6 mm for the high dose groups compared to ≤4 mm for the low dose groups (Figure 5B). The Bland-Altman plot shows that the μCT and histological methods for measuring ridge height yield results that are statistically the same, which suggests that the μCT method reported in this study is an appropriate method for measuring ridge height compared to the more conventional histological approach. Furthermore, the ridge width was maintained near the upper surface of the defect for the high dose groups while the low dose groups revealed a trend of narrowing ridge width (Figure 4A). LV composites exhibit diffusion- and degradation-mediated of rhBMP-2 for up to 4 weeks *in vivo*. Considering previous studies reporting that a sustained release of rhBMP-2 can promote new bone formation at a sub-optimal dose of rhBMP-2 in femoral segmental defects (49, 50), the low dose was anticipated to more effectively heal the ridge defects. Inadequate healing of the low-dose treatment groups in the present study could be attributed to the challenges of the mandibular ridge defect model, in which the graft is subject to compressive forces that are greater than the forces on the graft in the femoral segmental defect model. While the low-dose treatment did not maintain the host ridge height, the quality of the new bone that formed was similar to that observed for the high-dose treatment, as evidenced by the fact that no significant differences were observed between any of the morphometric parameters (BV/TV, Tb.N, Tb.Sp, or Tb.Th) calculated from the µCT data. In previous studies, compression-resistant CM/collagen grafts maintained space and supported new bone formation in non-human primate posterolateral fusion (51) and mandibular continuity defect (44) models without protective membranes. However, the optimal dose for bone healing was 2.0 mg/ml, which was 33% higher than the recommended dose for the ACS carrier (1.5 mg/ml). In contrast, the LV/CM and LV/BG carriers supported new bone formation at a dose within the recommended range for dogs. Additional testing in a non-human primate model of lateral ridge augmentation is required to determine whether adequate space maintenance and bone healing can be achieved at a dose lower than that of the compression-resistant CM/collagen carrier.

The study was designed to answer the question whether injectable low-viscosity (LV) PUR/ceramic composites augmented with rhBMP-2 could maintain the contour of the ridge and promote new bone formation in a large animal model of ridge augmentation at a clinically relevant time point. Both LV/BG and LV/CM grafts maintained ridge height and width at the high dose of rhBMP-2 at 16 weeks. No residual polymer was observed in any of the four treatment groups, which is consistent with previous studies reporting that lysine-derived polyurethanes undergo cell-mediated degradation (52) and almost completely degrade at 12 weeks in rabbit models of bone regeneration (7, 31). Images of histological sections (Figure 5B) show appositional new bone growth on the surface of the CM particles. Thus, increasing the volume fraction of the ceramic component is anticipated new increase new bone formation, although the resulting composite would have limited injectability (31, 53). Assessing outcomes at an intermediate (e.g., 8 week) time point could provide additional insight into the spatio-temporal dynamics of bone healing, including the relative contributions of the polymer and ceramic degradation rates to new bone formation (54). Another limitation of this study is that the LV grafts were not compared to a clinical control, such as autograft or ACS. However, to our knowledge, this is the first study to report an injectable, settable, and compression-resistant bone graft that maintains the height and width of the mandibular ridge in a model in which conventional grafts such as the ACS carrier (55-57) and autograft (58) resorb without GBR membranes. In ongoing studies, the injectable LV/CM graft without a GBR membrane will be compared to the ACS carrier with the membrane in a preclinical model of lateral ridge augmentation to assess its potential as a compression-resistant carrier for rhBMP-2.

Conclusion

Injectable, settable, and compression-resistant LV bone grafts augmented with rhBMP-2 were evaluated in a canine mandibular ridge saddle defect model. Composite bone grafts synthesized from a lysine-derived polyurethane and ceramic particles exhibited bulk moduli exceeding 1 MPa. At the rhBMP-2 dose recommended for the ACS carrier in dogs (400 μg/ml), LV grafts maintained the width and height of the host mandibular ridge and supported new bone formation, while at sub-optimal (100 μg/ml) doses the anatomic contour of the ridge was not maintained. These findings suggest that both the initial bulk modulus and also the rhBMP-2 dose regulate healing of compression-resistant bone grafts for healing mandibular ridge defects.

References

1. Esposito, M., Grusovin, M.G., Felice, P., Karatzopoulos, G., Worthington, H.V., andCoulthard, P. Interventions for replacing missing teeth: horizontal and vertical bone augmentation techniques for dental implant treatment. The Cochrane Library 2009.
2. Demarosi, F., Leghissa, G.C., Sardella, A., Lodi, G., andCarrassi, A. Localised maxillary ridge expansion with simultaneous implant placement: A case series. British Journal of Oral and Maxillofacial Surgery **47**, 535, 2009.
3. Bohner, M., Galea, L., andDoebelin, N. Calcium phosphate bone graft substitutes: Failures and hopes. Journal of the European Ceramic Society **32**, 2663, 2012.
4. Jones, J.R. Review of bioactive glass: from Hench to hybrids. Acta Biomater **9**, 4457, 2013.
5. Rezwan, K., Chen, Q.Z., Blaker, J.J., andBoccaccini, A.R. Biodegradable and bioactive porous polymer/inorganic composite scaffolds for bone tissue engineering. Biomaterials **27**, 3413, 2006.
6. Bonzani, I.C., Adhikari, R., Houshyar, S., Mayadunne, R., Gunatillake, P., andStevens, M.M. Synthesis of two-component injectable polyurethanes for bone tissue engineering. Biomaterials **28**, 423, 2007.
7. Dumas, J.E., BrownBaer, P.B., Prieto, E.M., Guda, T., Hale, R.G., Wenke, J.C., andGuelcher, S.A. Injectable reactive biocomposites for bone healing in critical-size rabbit calvarial defects. Biomed Mater **7**, 024112, 2012.
8. Dumas, J.E., Davis, T., Holt, G.E., Yoshii, T., Perrien, D.S., Nyman, J.S., Boyce, T., andGuelcher, S.A. Synthesis, characterization, and remodeling of weight-bearing allograft bone/polyurethane composites in the rabbit. Acta Biomaterialia **6**, 2394, 2010.
9. Harmata, A.J., Ward, C.L., Zienkiewicz, K.J., Wenke, J.C., andGuelcher, S.A. Investigating the effects of surface-initiated polymerization of ε-caprolactone to bioactive glass particles on the mechanical properties of settable polymer/ceramic composites. Journal of Materials Research **29**, 2398, 2014.
10. Ji, W., Wang, H., van den Beucken, J.J.J.P., Yang, F., Walboomers, X.F., Leeuwenburgh, S., andJansen, J.A. Local delivery of small and large biomolecules in craniomaxillofacial bone. Advanced Drug Delivery Reviews **64**, 1152, 2012.
11. Luvizuto, E.R., Tangl, S., Zanoni, G., Okamoto, T., Sonoda, C.K., Gruber, R., andOkamoto, R. The effect of BMP-2 on the osteoconductive properties of β-tricalcium phosphate in rat calvaria defects. Biomaterials **32**, 3855, 2011.
12. Notodihardjo, F.Z., Kakudo, N., Kushida, S., Suzuki, K., andKusumoto, K. Bone regeneration with BMP-2 and hydroxyapatite in critical-size calvarial defects in rats. Journal of Cranio-Maxillofacial Surgery **40**, 287, 2012.
13. Mariner, P.D., Wudel, J.M., Miller, D.E., Genova, E.E., Streubel, S.O., andAnseth, K.S. Synthetic hydrogel scaffold is an effective vehicle for delivery of INFUSE (rhBMP2) to critical-sized calvaria bone defects in rats. J Orthop Res **31**, 401, 2013.
14. Jung, R.E., Weber, F.E., Thoma, D.S., Ehrbar, M., Cochran, D.L., andHämmerle, C.H.F. Bone morphogenetic protein-2 enhances bone formation when delivered by a synthetic matrix containing hydroxyapatite/tricalciumphosphate. Clinical Oral Implants Research **19**, 188, 2008.
15. Jovanovic, S.A., Hunt, D.R., Bernard, G.W., Spiekermann, H., Wozney, J.M., andWikesjo, U.M. Bone reconstruction following implantation of rhBMP-2 and guided bone regeneration in canine alveolar ridge defects. Clin Oral Implants Res **18**, 224, 2007.

16. Huh, J.-B., Kim, S.-E., Kim, H.-E., Kang, S.-S., Choi, K.-H., Jeong, C.-M., Lee, J.-Y., andShin, S.-W. Effects of anodized implants coated with Escherichia coli-derived rhBMP-2 in beagle dogs. International Journal of Oral and Maxillofacial Surgery **41**, 1577, 2012.
17. de Freitas, R.M., Spin-Neto, R., Junior, E.M., Pereira, L.A.V.D., Wikesjö, U.M.E., andSusin, C. Alveolar Ridge and Maxillary Sinus Augmentation Using rhBMP-2: A Systematic Review. Clinical Implant Dentistry and Related Research **17**, e192, 2015.
18. Schwarz, F., Mihatovic, I., Golubovic, V., Hegewald, A., andBecker, J. Influence of two barrier membranes on staged guided bone regeneration and osseointegration of titanium implants in dogs: part 1. Augmentation using bone graft substitutes and autogenous bone. Clin Oral Implants Res **23**, 83, 2012.
19. Iglhaut, G., Schwarz, F., Grundel, M., Mihatovic, I., Becker, J., andSchliephake, H. Shell technique using a rigid resorbable barrier system for localized alveolar ridge augmentation. Clin Oral Implants Res **25**, e149, 2014.
20. Ruskin, J.D., Hardwick, R., Buser, D., Dahlin, C., andSchenk, R.K. Alveolar ridge repair in a canine model using rhTGF-β1 with barrier membranes. Clinical oral implants research **11**, 107, 2000.
21. Jovanovic, S.A., Hunt, D.R., Bernard, G.W., Spiekermann, H., Wozney, J.M., andWikesjö, U.M. Bone reconstruction following implantation of rhBMP-2 and guided bone regeneration in canine alveolar ridge defects. Clinical oral implants research **18**, 224, 2007.
22. Schliephake, H., Drewes, M., Mihatovic, I., Schwarz, F., Becker, J., andIglhaut, G. Use of a self-curing resorbable polymer in vertical ridge augmentations - a pilot study in dogs. Clin Oral Implants Res **25**, 435, 2014.
23. dal Polo, M.R., Poli, P.P., Rancitelli, D., Beretta, M., andMaiorana, C. Alveolar ridge reconstruction with titanium meshes: A systematic review of the literature. Medicina oral, patologia oral y cirugia bucal **19**, e639, 2014.
24. Guelcher, S., Srinivasan, A., Hafeman, A., Gallagher, K., Doctor, J., Khetan, S., McBride, S., andHollinger, J. Synthesis, in vitro degradation, and mechanical properties of two-component poly(ester urethane)urea scaffolds: effects of water and polyol composition. Tissue Eng **13**, 2321, 2007.
25. Guelcher, S.A., Patel, V., Gallagher, K.M., Connolly, S., Didier, J.E., Doctor, J.S., andHollinger, J.O. Synthesis and in vitro biocompatibility of injectable polyurethane foam scaffolds. Tissue engineering **12**, 1247, 2006.
26. Jiang, G., Evans, M., Jones, I., Rudd, C., Scotchford, C., andWalker, G. Preparation of poly (ε-caprolactone)/continuous bioglass fibre composite using monomer transfer moulding for bone implant. Biomaterials **26**, 2281, 2005.
27. Jiang, G., Walker, G., Jones, I., andRudd, C. XPS identification of surface-initiated polymerisation during monomer transfer moulding of poly (ε-caprolactone)/Bioglass® fibre composite. Applied surface science **252**, 1854, 2005.
28. Verné, E., Vitale-Brovarone, C., Bui, E., Bianchi, C., andBoccaccini, A. Surface functionalization of bioactive glasses. Journal of biomedical materials research Part A **90**, 981, 2009.
29. Bouxsein, M.L., Boyd, S.K., Christiansen, B.A., Guldberg, R.E., Jepsen, K.J., andMuller, R. Guidelines for assessment of bone microstructure in rodents using micro-computed tomography. J Bone Miner Res **25**, 1468, 2010.
30. Hoshi, S., Akizuki, T., Matsuura, T., Ikawa, T., Kinoshita, A., Oda, S., Tabata, Y., Matsui, M., andIzumi, Y. Ridge augmentation using recombinant human fibroblast growth factor-2 with

biodegradable gelatin sponges incorporating β-tricalcium phosphate: a preclinical study in dogs. Journal of Periodontal Research, n/a, 2015.
31. Prieto, E.M., Talley, A.D., Gould, N.R., Zienkiewicz, K.J., Drapeau, S.J., Kalpakci, K.N., andGuelcher, S.A. Effects of particle size and porosity on in vivo remodeling of settable allograft bone/polymer composites. Journal of Biomedical Materials Research Part B: Applied Biomaterials, n/a, 2015.
32. Dumas, J.E., Zienkiewicz, K., Tanner, S.A., Prieto, E.M., Bhattacharyya, S., andGuelcher, S.A. Synthesis and characterization of an injectable allograft bone/polymer composite bone void filler with tunable mechanical properties. Tissue Engineering Part A **16**, 2505, 2010.
33. Talley, A.D., Funk, S.S., Zienkiewicz, K.J., Dasgupta, J., Wenke, J.C., Davidson, J.M., Holt, G.E., andGuelcher, S.A. *In vivo* rhBMP-2 Release from Degradable Polyurethane Composites. Artif Organs **Submitted**.
34. Verardi, S., andSimion, M. Management of the exposure of e-PTFE membranes in guided bone regeneration. Practical procedures & aesthetic dentistry: PPAD **19**, 111, 2007.
35. Hyder, P., Dowell, P., Singh, G., andDolby, A. Freeze-Dried, Cross-Linked Bovine Type I Collagen: Analysis of Properties*. Journal of periodontology **63**, 182, 1992.
36. Goktas, S., Dmytryk, J.J., andMcFetridge, P.S. Biomechanical behavior of oral soft tissues. Journal of periodontology **82**, 1178, 2011.
37. Kawakatsu, N., Oda, S., Kinoshita, A., Kikuchi, S., Tsuchioka, H., Akizuki, T., Hayashi, C., Kokubo, S., Ishikawa, I., andIzumi, Y. Effect of rhBMP-2 with PLGA/gelatin sponge type (PGS) carrier on alveolar ridge augmentation in dogs. Journal of oral rehabilitation **35**, 647, 2008.
38. Lacoste-Ferré, M.-H., Demont, P., Dandurand, J., Dantras, E., Duran, D., andLacabanne, C. Dynamic mechanical properties of oral mucosa: comparison with polymeric soft denture liners. Journal of the mechanical behavior of biomedical materials **4**, 269, 2011.
39. Xu, C., Lei, C., Meng, L., Wang, C., andSong, Y. Chitosan as a barrier membrane material in periodontal tissue regeneration. Journal of Biomedical Materials Research Part B: Applied Biomaterials **100B**, 1435, 2012.
40. van Leeuwen, A.C., Huddleston Slater, J.J.R., Gielkens, P.F.M., de Jong, J.R., Grijpma, D.W., andBos, R.R.M. Guided bone regeneration in rat mandibular defects using resorbable poly(trimethylene carbonate) barrier membranes. Acta Biomaterialia **8**, 1422, 2012.
41. Orellana, B.R., Thomas, M.V., Dziubla, T.D., Shah, N.M., Hilt, J.Z., andPuleo, D.A. Bioerodible calcium sulfate/poly(β-amino ester) hydrogel composites. Journal of the Mechanical Behavior of Biomedical Materials **26**, 43, 2013.
42. Requicha, J.F., Viegas, C.A., Hede, S., Leonor, I.B., Reis, R.L., andGomes, M.E. Design and characterization of a biodegradable double-layer scaffold aimed at periodontal tissue-engineering applications. Journal of Tissue Engineering and Regenerative Medicine, n/a, 2013.
43. Kane, R.J., Weiss-Bilka, H.E., Meagher, M.J., Liu, Y., Gargac, J.A., Niebur, G.L., Wagner, D.R., andRoeder, R.K. Hydroxyapatite reinforced collagen scaffolds with improved architecture and mechanical properties. Acta biomaterialia **17**, 16, 2015.
44. Herford, A.S., Lu, M., Buxton, A.N., Kim, J., Henkin, J., Boyne, P.J., Caruso, J.M., Rungcharassaeng, K., andHong, J. Recombinant human bone morphogenetic protein 2 combined with an osteoconductive bulking agent for mandibular continuity defects in nonhuman primates. Journal of Oral and Maxillofacial Surgery **70**, 703, 2012.
45. Akamaru, T., Suh, D., Boden, S.D., Kim, H.S., Minamide, A., andLouis-Ugbo, J. Simple carrier matrix modifications can enhance delivery of recombinant human bone morphogenetic protein-2 for posterolateral spine fusion. Spine (Phila Pa 1976) **28**, 429, 2003.

46. Dawson, E., Bae, H.W., Burkus, J.K., Stambough, J.L., andGlassman, S.D. Recombinant human bone morphogenetic protein-2 on an absorbable collagen sponge with an osteoconductive bulking agent in posterolateral arthrodesis with instrumentation. The Journal of Bone & Joint Surgery **91**, 1604, 2009.
47. Midha, S., van den Bergh, W., Kim, T.B., Lee, P.D., Jones, J.R., andMitchell, C.A. Bioactive Glass Foam Scaffolds are Remodelled by Osteoclasts and Support the Formation of Mineralized Matrix and Vascular Networks In Vitro. Advanced Healthcare Materials **2**, 490, 2013.
48. McKay, W.F., Peckham, S.M., andMarotta, J.S. The science of rhBMP-2: Quality Medical Pub.; 2006.
49. Brown, K.V., Li, B., Guda, T., Perrien, D.S., Guelcher, S.A., andWenke, J.C. Improving bone formation in a rat femur segmental defect by controlling bone morphogenetic protein-2 release. Tissue Eng Part A **17**, 1735, 2011.
50. Boerckel, J.D., Kolambkar, Y.M., Dupont, K.M., Uhrig, B.A., Phelps, E.A., Stevens, H.Y., Garcia, A.J., andGuldberg, R.E. Effects of protein dose and delivery system on BMP-mediated bone regeneration. Biomaterials **32**, 5241, 2011.
51. Barnes, B., Boden, S.D., Louis-Ugbo, J., Tomak, P.R., Park, J.S., Park, M.S., andMinamide, A. Lower dose of rhBMP-2 achieves spine fusion when combined with an osteoconductive bulking agent in non-human primates. Spine (Phila Pa 1976) **30**, 1127, 2005.
52. Hafeman, A.E., Zienkiewicz, K.J., Zachman, A.L., Sung, H.J., Nanney, L.B., Davidson, J.M., andGuelcher, S.A. Characterization of the degradation mechanisms of lysine-derived aliphatic poly(ester urethane) scaffolds. Biomaterials **32**, 419, 2011.
53. Bennett, S., Connolly, K., Lee, D.R., Jiang, Y., Buck, D., Hollinger, J.O., andGruskin, E.A. Initial biocompatibility studies of a novel degradable polymeric bone substitute that hardens in situ. Bone **19**, S101, 1996.
54. Dumas, J.E., Prieto, E.M., Zienkiewicz, K.J., Guda, T., Wenke, J.C., Bible, J., Holt, G.E., andGuelcher, S.A. Balancing the rates of new bone formation and polymer degradation enhances healing of weight-bearing allograft/polyurethane composites in rabbit femoral defects. Tissue Eng Part A **20**, 115, 2014.
55. Sigurdsson, T.J., Nygaard, L., Tatakis, D.N., Fu, E., Turek, T.J., Jin, L., Wozney, J.M., andWikesjö, U. Periodontal repair in dogs: evaluation of rhBMP-2 carriers. The International journal of periodontics & restorative dentistry **16**, 524, 1996.
56. Barboza, E.P., Caúla, A.L., Caúla, F.d.O., de Souza, R.O., Neto, L.G., Sorensen, R.G., Li, X.J., andWikesjö, U.M. Effect of recombinant human bone morphogenetic protein-2 in an absorbable collagen sponge with space-providing biomaterials on the augmentation of chronic alveolar ridge defects. Journal of periodontology **75**, 702, 2004.
57. Barboza, E.P., Duarte, M.E.L., Geolás, L., Sorensen, R.G., Riedel, G.E., andWikesjö, U.M. Ridge augmentation following implantation of recombinant human bone morphogenetic protein-2 in the dog. Journal of periodontology **71**, 488, 2000.
58. Von Arx, T., Schenk, R.K., Buser, D., Cochran, D.L., andHermann, J.S. Lateral ridge augmentation using different bone fillers and barrier membrane application. Clinical Oral Implants Research **12**, 260, 2001.

CHAPTER VI

RELATIVE OSTEOCLASTIC RESORPTION RATES OF CERAMICS AND BIOACTIVE GLASS

Introduction

The term bone graft encompasses a wide variety of materials used in bone regeneration applications. Autogenic bone, often considered the clinical gold standard for bone grafting, and allogenic bone, from cadaver tissue, remodel by a process of creeping substitution where the old bone is remodeled by osteoclasts while new bone is deposited by osteoblasts. However, restrictions arise due to limited availability and donor site morbidity with autologous bone and the risk for disease transmission associated with allograft bone (1). Due to these constraints, significant research has been conducted on synthetic, biodegradable bone graft alternatives. The remodeling characteristics of the grafts contribute to cellular infiltration, cellular differentiation, osseous deposition, and mechanical integrity (2-4), but the degradation rates are not known for many materials. Voids and inconsistent healing can occur if the *in vivo* graft remodeling does not match the rate of new bone deposition (5). One main mechanism of *in vivo* degradation is resorption by osteoclasts. However, the resorption potential of biomaterials is not well understood and there is considerable interest in developing an inexpensive, reproducible *in vitro* assay to test osteoclast resorption on matrices of interest.

Ceramics and bioactive glasses are two classes of biomaterials used widely in bone reconstruction (6, 7). β-tricalcium phosphate (β-TCP) and hydroxyapatite (HA) are clinically relevant, osteogenic ceramics with mineral content similar to that of natural bone. When implanted *in vivo* 45S5 bioactive glass (BG) bonds with host bone and stimulates new bone growth and has been used clinically in over a million patients (6). Remodeling of these bone grafts proceeds through two processes: active cellular resorption and bulk or surface chemical degradation (3). Graft porosity, surface topography, biological signals, chemical structure, physiochemical properties (crystallinity, density), implantation site, and other factors all influence remodeling (8-11), contributing to the difficulty of studying these materials *in vivo* and *in vitro*. Previous studies suggest that calcium phosphate remodeling is a predominately cellular process initiated by a number of cell types including macrophages, osteoclasts, and monocytes (10, 12). Bioactive glasses, on the other hand, are chemically active after surface contact with body fluids, releasing numerous ionic species that contribute to both material dissolution and cellular response (6, 13). The dissolution rates are specific to the chemical composition of the particular silicate or phosphate based system of interest. In general, it has been shown that bioactive glasses remodel more quickly than ceramics *in vivo* (14, 15).

A number of *in vitro* osteoclast assays have been previously studied since the first assays were developed in the 1980s. One of the initial techniques involved the use of 1α,25-dihydroxyvitamin D_3 (VD3) to stimulate mouse osteoblastic cells, isolated from calvaria, to induce osteoclast differentiation in mouse spleen cells (16) or osteoclast precursor cells from mouse long bones (17). Additionally, some groups employed tumor necrosis factors (TNF) –α and –β (18) or interleukin 1 (IL-1) (19) to induce osteoclast resorption *in vitro*. Later work revealed that the signaling molecule receptor activator of nuclear factor-κβ ligand (RANKL) is responsible for osteoblast driven osteoclastogenesis, while macrophage-colony stimulating factor (M-CSF) aids in osteoclast survival but not active resorption (20). More recently, groups have used M-CSF and RANKL in *in vitro* osteoclast cultures with primary cells (21) or cell lines (22), but the high cost of these factors can be prohibitive.

Commonly accepted markers for osteoclasts include multinucleated, tartrate resistant acid phosphatase (TRAP) positive cells with actin rings (23). Previously, active resorption has been measured by scanning electron microscopy (SEM) (21, 24), podosome belt formation (25), transmission electron microscopy (TEM) (26), light microscopy (27), three-dimensional (3D) laser color microscopy (24), and optical 3D profilometry (28, 29). But there is no widely accepted, standardized procedure for quantifying osteoclast resorption rates on substrates of interest.

Previous assays using MCSF and RANKL to differentiate osteoclastic precursor cells produce viable, active osteoclasts. However, these methods are limited by the cost of the growth factors and variability due to animal age and health when harvesting primary cells. It is desirable to develop a co-culture technique based on established cell lines that uses a small concentration of VD3 to reproducibly drive differentiation and to develop a standardized, quantifiable method to analyze relative osteoclast resorption rates. In this study, we investigated a co-culture of pre-osteoblastic MC3T3 cells and a monocyte cell line RAW 264.7 cells and tested resorption on β-TCP, HA, BG, and dentin chips (D) using optical profilometry to quantify the relative rates of 3D resorption.

Experimental

Materials. The murine osteoblast precursor cell line, MC3T3, and the murine macrophage cell line, RAW 264.7, were purchased from ATCC (Manassas, VA). Hydroxyapatite (HA) and β-tricalcium phosphate (TCP) discs, sized to fit a 48 well plate, were purchased from 3D Biotek (Hillborough, NJ). 45S5 bioactive glass (BG) rods were obtained from Mo-Sci Corporation (Rolla, MO) and cut to ~0.5mm thickness using a IsoMet low speed saw (Buehler). Dentin (D) was acquired from the donation of a surrendered elephant tusk from the National Eagle and Wildlife Property Repository of the United States Department of the Interior, U.S. Fishes and Wildlife

Service. Cells were cultured in αMEM (minimum essential media) from GIBCO (Grand Island, NY) supplemented with 10% FBS (Hyclone, Logan, UT) and 1% Penicillin-Streptomycin (GIBCO) and the osteogenic factors 10nM dexamethasone, 50 µg/mL ascorbic acid, and 0.1 mM β-glycerophosphate. 1α,25 dihydroxyvitamin D_3 (VD3) was purchased from Sigma (St. Louis, MO).

Assay Development. MC3T3 cells were plated on a 24 well plate at $1 * 10^4$ cells/well in 1 mL osteogenic (OG) media supplemented with 10nM VD3. Cells were grown at 37°C for 48hr. Media was aspirated and RAW cells were plated at $1 * 10^4$ cells/well in 1 mL OG media supplemented with 10nM. Every 1-2 days 0.5mL of OG media was removed and replaced with new 0.5mL OG media supplemented with 10nM VD3. Cells were imaged over the course of the study to analyze cell morphological changes and growth.

Sample sterilization and conditioning. BG discs were initially cleaned by sonication for 5 min in acetone:DI water (5:95 volume ratio). All samples for cell culture were then sonicated for 7.5 min in DI water (3x). To sterilize, samples were immersed in 70% ethanol for 5 min (2x). After which time samples were washed in sterile DI water for 5 min (2x) before being transferred to tissue culture plastic plates. Samples were conditioned overnight in complete αMEM prior to cell seeding.

Resorption Testing. Incubation media was removed from wells and materials were allowed to dry in a sterile hood for 30min. MC3T3 cells were then plated on matrices of interest at $1 * 10^4$ cells/100 µL osteogenic (OG) media in each well, following a protocol for osteoblast seeding from 3D Biotek. Well plates were incubated at 37°C for 30min to allow for cellular attachment. An additional 900 µL OG media with 10nM VD3 (for the whole 1 mL) was added to each well and cells were grown at 37°C for 48hr. Media was aspirated and RAW cells were plated at $1 *10^4$

cells/100 µL OG media. Well plates were incubated at 37°C for 30min to aid in cellular attachment. An additional 900 µL OG media with 10nM VD3 was added to each well and cells were grown at 37°C. After 48 hrs matrix discs were moved to new well plates. Every 1-2 days 0.5mL of OG media was removed and replaced with new 0.5mL OG media supplemented with 10nM VD3.

TRAP staining. At desired time points, samples were removed from cell culture and fixed in 10% formalin for 15 min at room temperature. Samples were washed 3x with cold PBS and incubated in a 0.2 mg/mL Naphthol AS-BI substrate solution for 30 min at 37°C, after which time the substrate solution was removed. Samples were immediately incubated with a color reaction solution of pararosaniline dye (25mg/mL) for 10 min at room temperature. Samples were rinsed in DI water, counterstained with Harris's acid hematoxylin stain for 20s, and rinsed in running water for 1 min.

Actin staining. At desired time points, samples were removed from cell culture and fixed in 10% formalin for 10 min at room temperature. Samples were washed 2x with PBS and incubated with 0.1 % Triton-X in PBS for 5 min to permeabilize cells. Samples were incubated with rhodamine phalloidin (5 µL methanol solution in 200 µL PBS) for 45 min at 37°C to stain actin. Samples were washed 2x with PBS, counterstained with DAPI (2 µg/mL) for 5 min, and washed 2x with PBS.

Profilometry. At desired time points, media was removed and sterile DI water was added to wells for 24 hrs to loosen cells. Any remaining cells were removed by washing the surface with DI water. Samples were dried overnight on a benchtop. Resorption pits were analyzed using a Zeta Instruments Zeta-20 True Color 3D Optical Profiler (San Jose, CA). Images were collected using a Z-rage of 15-20 µm at 200 steps, resulting in a Z-step size of 0.075 – 0.1 µm. A 20x magnification was used to image at least 3 different areas per sample (field of view: 474 x 356 µm^2). Zeta feature detection software was used to quantify pits, specified as areas with a specified depth from a reference surface on non-resorbed areas. The minimum thresholds for pit detection were established as 3 µm for BG, 2 µm for D, and 1.5 µm for TCP and HA. The % of the surface area that was resorbed was reported as well as total resorbed volume per image normalized to the analyzed field of view. Roughness of each sample (R_a) was analyzed from feature detection software.

Scanning Electron Microscopy. To further visualize resorption pits on substrates, scanning electron microscopy (SEM) images were taken of both initial, unresorbed samples and co-culture samples after 25 days. Samples were mounted onto a scanning electron microscopy (SEM) pin stub mount and sputter-coated for 40 s using a Cressington Q108 sputter coater, which deposits gold at a 30 mA current. A Hitachi S-4200 SEM was used to acquire images at a voltage of 1kV.

Statistical analysis. Differences in resorption volumes, resorption area, and roughness among samples was analyzed by two-way ANOVA. Statistical significance was considered for $p < 0.05$.

Results

Assay Development. The MC3T3 and RAW264.7 cell co-culture was tested on tissue culture plastic to study the progression of osteoclast development. Bright field image of cells at 5 and 10 days (Figure 6.1 A,B), TRAP stained cells at 17 days (Figure 6.1 C) and Actin stained cells at 17 days (Figure 6.1D) show progression of differentiation. The formation of some large egg shaped cells, which is indicative of osteoclastic differentiation, are present at 10 days. By 17 days larger, TRAP+ cells with visible actin ring structure are present, which indicates osteoclast formation. A large number of non-differentiated RAW cells (small circular cells) remain at 17 days in the co-culture, which are also TRAP+.

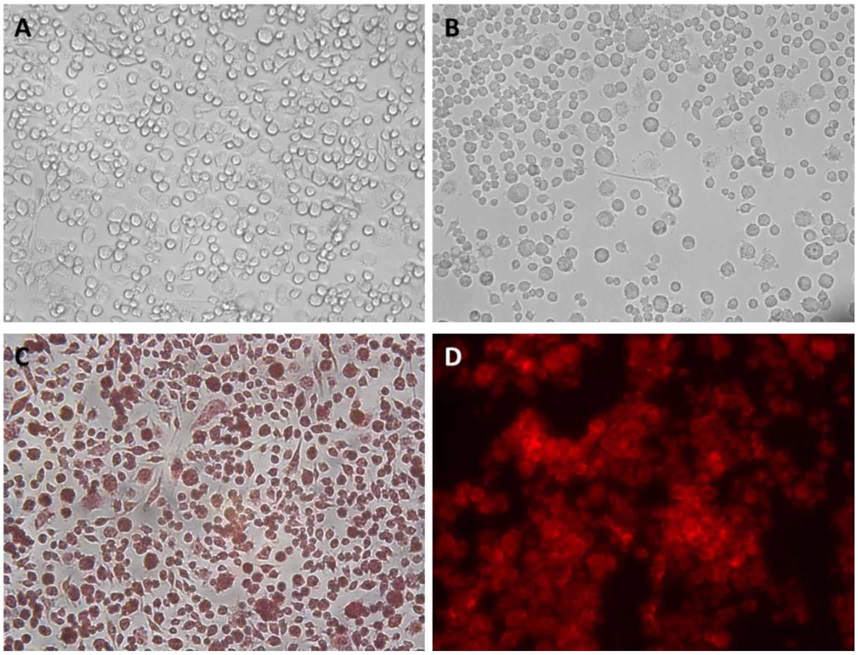

Figure 6.1. Bright field images of cells in co-culture on tissue culture plastic at (A) 5 days and (B) 10 days after the start of the assay. Cells at 17 days were (A) TRAP stained and (B) actin stained to show larger, TRAP+ cells and cells with a visible actin ring structure. Images A-C were taken at 20x. Image D was taken at 10x.

Co-culture. TRAP positive, multinucleated cells were visible on BG and D samples at 21 and 25 days in co-culture indicating the presence of osteoclasts on these materials (Figure 6.2). Some areas of the D appear to be brighter (black arrows), which may be indicative of resorption pits. Due to the thickness of TCP and HA discs, bright field images could not be taken of these samples as not enough light could penetrate through the discs for TRAP visualization. This precluded the use of TRAP staining on TCP and HA to verify osteoclast presence. Cells on matrices of interest were stained after 21 days in co-culture for actin ring presence with counterstaining to display the nuclei (Figure 6.3). Multinucleated (3+) cells with visible, thick actin rings were present on all materials indicating the existence of osteoclasts, using an Inverted Microscope; however, images could not be acquired due to the high background of the DAPI stain and difficulty in focusing on the cells. Osteoclasts were detected with 3-5 nuclei. Confocal microscopy was used to get clear, 3D images of all samples, but the lasers available for use with confocal could not excite the DAPI stain (Figure 6.3). Large cells with clear actin rings were visible on substrates indicating the presence of osteoclasts (white arrows). Fewer osteoclasts were present on HA than the other matrices of interest. Multiple cells with 2 nuclei were present and many cells looked to be in the process of fusing with conjoining actin rings.

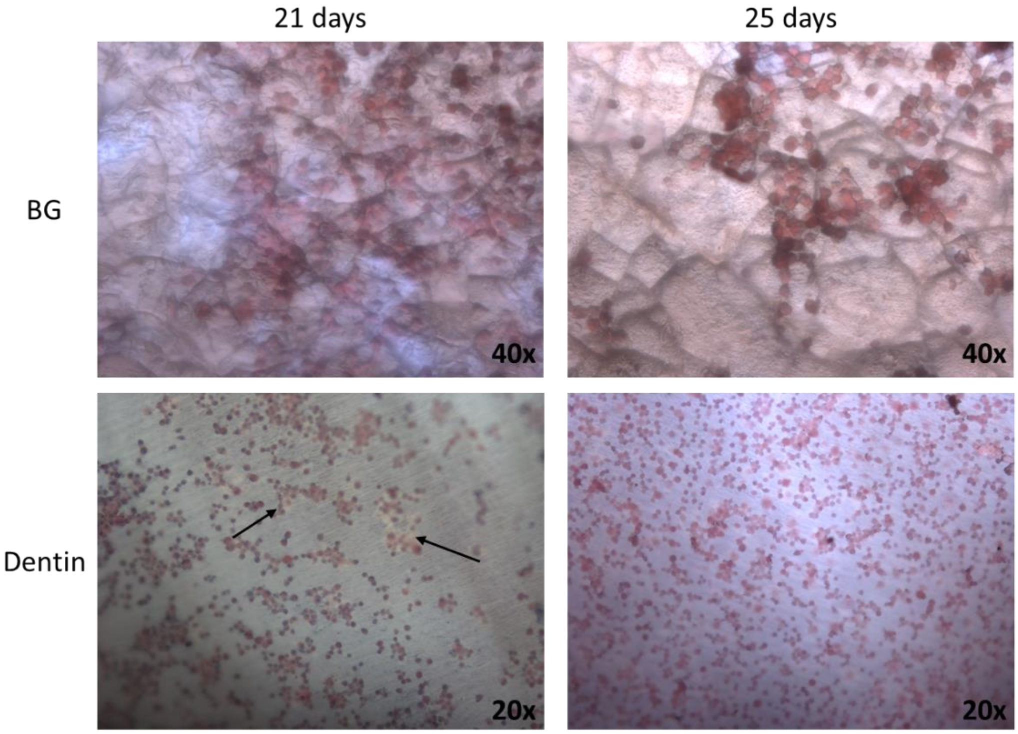

Figure 6.2. Bright field images of TRAP stained cells on BG and D. Larger TRAP+ cells are present on both substrates by 21 days. Some areas of D (black arrows) appear to be brighter (less opaque) which may indicate the presence of resorption pits.

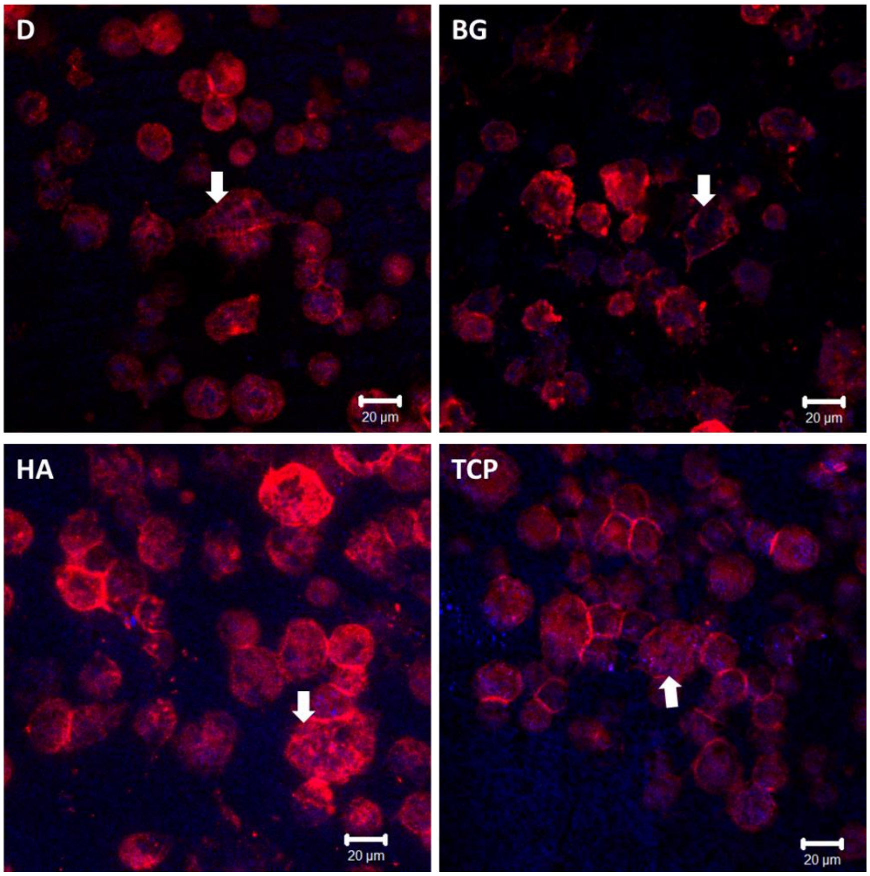

Figure 6.3. Confocal images of actin stained cells on substrates after 21 days. White arrows point to osteoclasts. The scale bar represents 20 µm.

Profilometry. Matrices of interest were analyzed for resorption pits using optical profilometry. Representative images of resorption pits are show in Figure 6.4, where the arrows point toward the pitted areas. The surface of BG discs was more rough than that of D, HA, or TCP, most likely due to the surface change and dissolution of the material. Resorption pits were visible on all materials at all of the time points, though pits on Dentin were the largest. Pits on HA were scarce and not homogenously distributed over the surface.

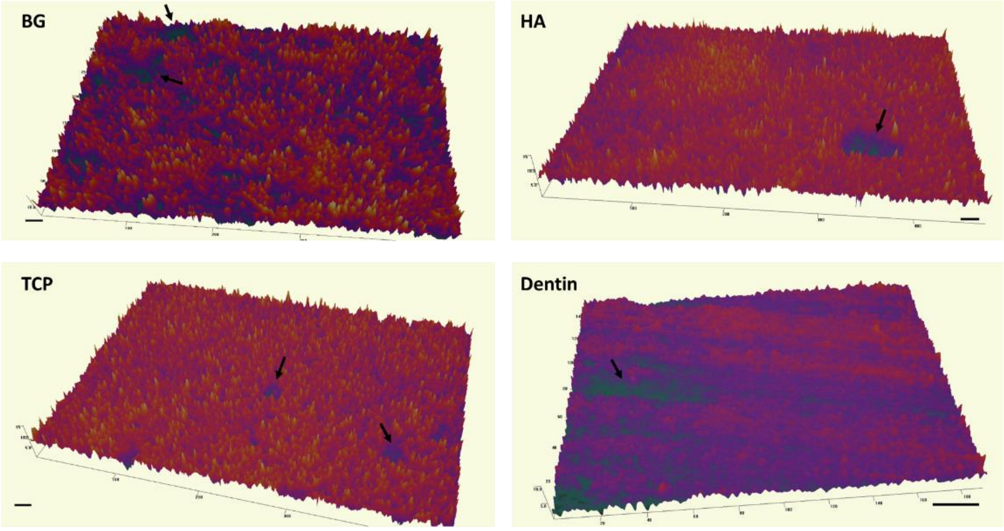

Figure 6.4. 3D profilometry images of substrates are 25 days in the osteoclast co-culture assay. Black arrows point to resorption pits on the surface. The scale bars represent 20µm.

Quantification of surface pitting was completed using Zeta feature detection software. The percent area resorbed on each surface and the resorption volume normalized to surface area were calculated (Figure 6.5A). The BG showed the highest resorption percent, however some of this may be attributed to the overall roughness of the surface which made it more difficult to selectively determine pitted areas. HA experienced the lowest surface resorption at both 21 and 25 days.

A straight line (Eqn 6.1) was fit to percent resorption data to determine resorption rates of each material over time.

$$P_r = k_r t + b \qquad (6.1)$$

The fitting parameters are shown in Figure 6.5B, where the slope (k_r) represents the resorption rate in units of percent surface area per day (% day^{-1}). Dentin had the highest rate of resorption at 0.419 % day^{-1}. BG and TCP showed similar values, of 0.260% day^{-1} and 0.241 % day^{-1} respectively, however the goodness of fit to TCP data was the lowest of any group. HA had the lowest resorption rate, at 0.062 % day$^{-1,}$. The resorption volume normalized to surface area (µm^3/ µm^2) was also calculated with D displaying the highest resorption volume at 25 days (Figure

6.5C). The surface of the BG discs was significantly more rough than D, TCP, or HA at all time points (Figure 6.5D). BG roughness increased slightly over time, though this was not significant. Roughness of D, TCP, and HA did not change over time.

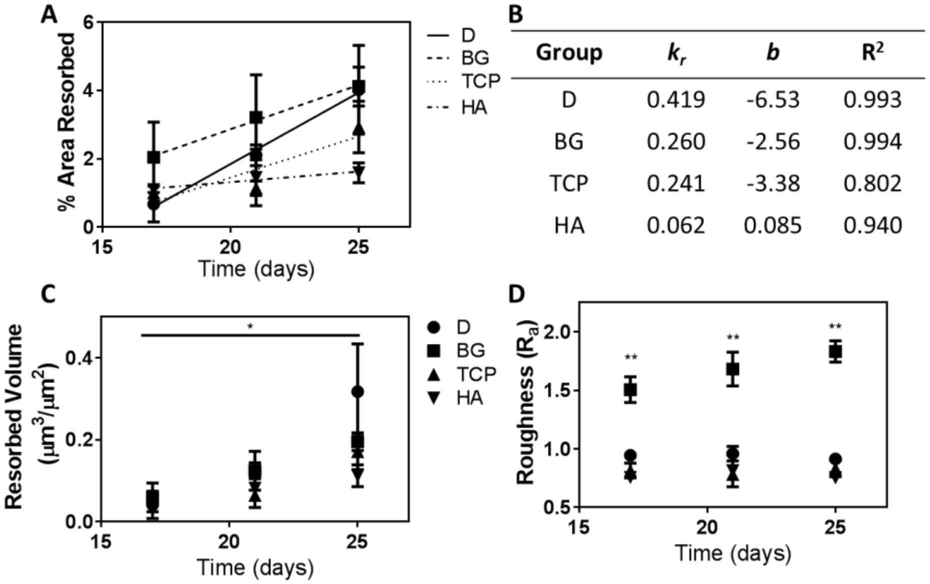

Group	k_r	b	R^2
D	0.419	-6.53	0.993
BG	0.260	-2.56	0.994
TCP	0.241	-3.38	0.802
HA	0.062	0.085	0.940

Figure 6.5. Quantitative analysis of profilometry scans to determine (A) percent of total surface area resorption, (B) fitting parameters for Eqn 6.1 fit to percent resorption data, (C) normalized resorption volume, and (D) roughness of the surface.

Scanning Electron Microscopy. SEM images of BG were taken of samples 1) after polishing, 2) after 25 days in media, and 3) after 25 days in co-culture (Figure 6.6). Following polishing the surface was flat with some minor blemishes. After 25 days in media without cells, the BG surface was significantly more rough with some cracks visible at higher magnification. After 25 days in co-culture, significant cracking was visible with a large increase in surface roughness.

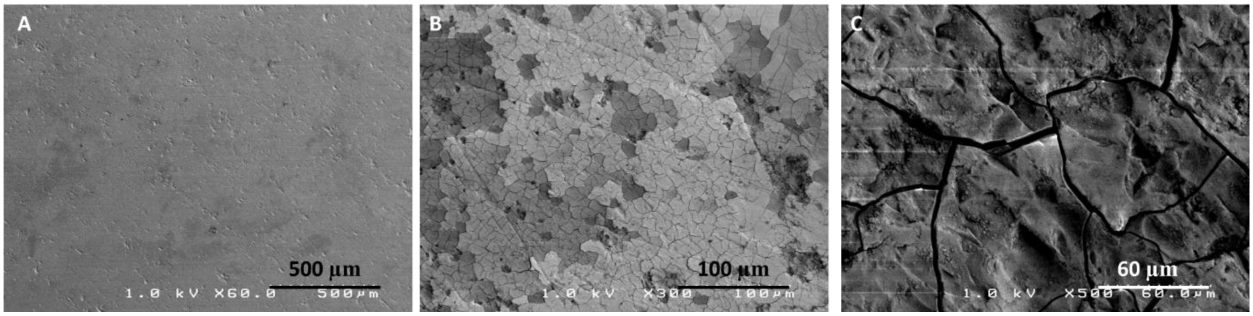

Figure 6.6. SEM images of BG (A) polished, before the start of culture (B) immersed in α-MEM for 25 days without cells and (C) after 25 days in co-culture.

Resorption pits were evident on the BG test disc when compared to the control sample. SEM images for TCP, HA, and D were taken after cleaning samples and following 25 days in co-culture (Figure 6.7). Ridges were evident on clean dentin samples while no recurrent topographical structures were present on the surface of HA or TCP discs. By 25 days, resorption pits were visible on all substrates surfaces. The pits on HA ware smaller, shallower, and less frequent than on TCP and D.

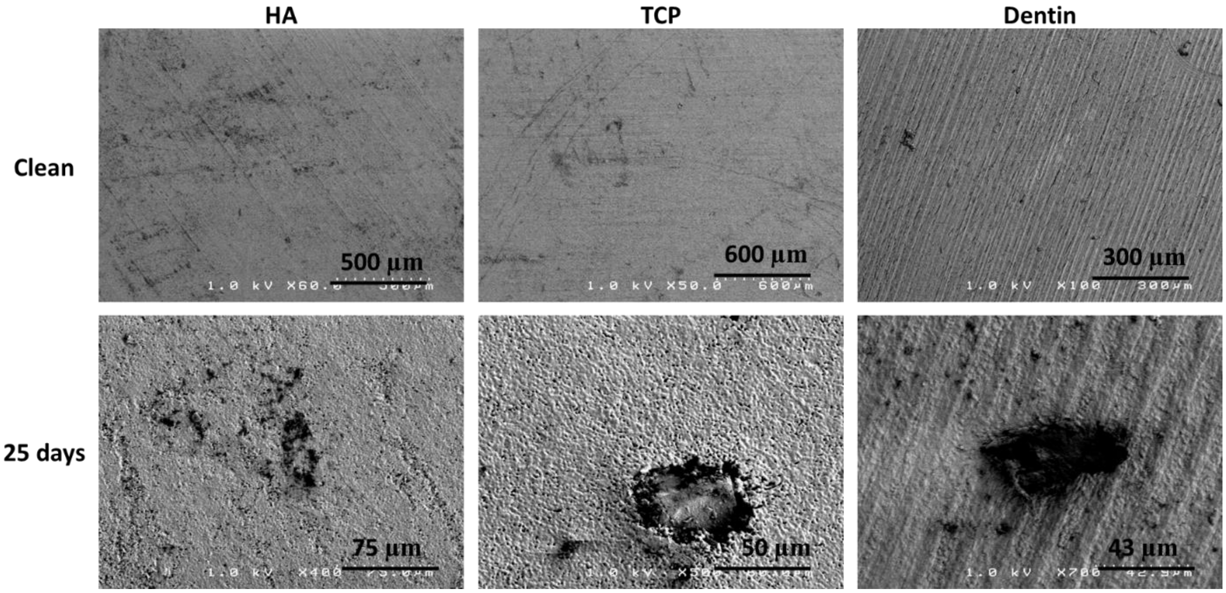

Figure 6.7. SEM images of clean substrates and samples after 25 days in co-culture for HA, TCP, and D.

Discussion

In order to design an effective bone graft, it is important to understand the biodegradation of the materials. A recent study has suggested that defects heal more reproducibly when bone graft degradation rates are similar to that of osseous integration and new bone deposition (5). However, there is conflicting information pertaining to the degradation rates, in particular that of osteoclast driven resorption, of ceramics and bioactive glasses. Previous studies have used numerous cell populations and differentiation methods to study *in vitro* osteoclast activity on substrates of interest, but there is no widely accepted, standardized assay for osteoclast differentiation or resorption measurements. In the present study, we developed a quantitative technique to determine relative resorption rates on a variety of synthetic materials using optical profilometry to measure pitting on substrates exposed to an osteoclast – osteoblast co-culture. As compared to dentin, resorption rates were approximately half for TCP and BG while HA resorption was 7 fold lower.

Osteoclast assays vary widely based on the initial cell source and differentiation methods. Some groups use M-CSF and RANKL to drive differentiation of primary monocyte populations, with osteoclast presence verified within 5-7 days (25, 30). However, there is often variability in these studies due to the source of the animals and the health and age of the mouse at cell harvest. Additionally, the cost of the growth factors can be prohibitive. Techniques dating back to the 1980s have successfully used 1α,25-dihydroxyvitamin D_3 (VD3) to drive differentiation of primary monocytes (17). More recently VD3 has been shown to drive differentiation of cells of the monocyte lineage (31). In the present study, VD3 is used to drive osteoclast differentiation in a co-culture of MC3T3 and RAW264.7 cells. Larger, egg-like cells, suspected to be osteoclast precursors, are visible within 2 weeks while osteoclasts are evident within 18 days as determined by TRAP staining.

While osteoclast formation was established on tissue culture plastic, osteoclastogenesis on synthetic substrates was also investigated. It is universally understood that formation of an F-actin ring and multinucleation are necessary for active osteoclast resorption. Previous groups have differentiated monocytes on ceramics and bioactive glasses with a variety of results. One group cultured human leukoma monocytes on HA and TCP discs and found more multinucleated TRAP+ cells on HA, with F-actin rings visible after 21 days, and some resorption pits (5 -65 μm in diameter) present on both materials (32). Studies of osteoclast activity on BG are scare in the literature, but one group has shown that osteoclasts can pit the surface of strontium-substituted bioactive glass with ion dissolution occurring over the same time frame, as measured by inductively coupled plasma – optical emission spectrometry (22). In the present study, two ceramics, β-tricalcium phosphate (TCP) and hydroxyapatite (HA), as well as 45S5 bioactive glass (BG) were tested in an osteoclast co-culture assay using dentin (D) chips as a reference material. These substrates were chosen based on their significant presence, both clinically and in research, in the field of bone engineering. TRAP staining on D and BG at 17 and 21 days revealed the presence of osteoclasts (TRAP+, multinucleated cells) on these substrates. However, TRAP staining could not be conducted on TCP or HA due to the thickness of the discs. Fluorescence labeling of actin along with a nuclear marker indicated the formation of osteoclasts on all substrates at by 21 days. Cells were visible with 3-5 nuclei, which is similar to previous studies (33).

Bone grafts delivered *in vivo* experience a number of cell types and fluid phases which can contribute to graft biodegradation. A main source of degradation is resorption which correlates to cellular activity. Once osteoclasts attach to a material substrate, a resorption lacuna is formed on the surface into which hydrogen ions are secreted thereby bringing the local pH down to approximately 4.5 (34). The acidity of the resorption lacuna creates an environment in which the ceramic is locally degraded. One previous study suggested that macrophages and giant cells are responsible for the majority of the degradation in brushite cements (9); however, other studies have shown significant osteoclast resorption of ceramics. A study investigating *in vitro* osteoclast resorption on calcium phosphates found osteoclast pitting on some calcium phosphates, but this was dependent on chemical composition and crystallinity of the substrates (35). In the present study resorption pits were evident on all tested substrates, when viewed by optical profilometry and SEM. Surface area and normalized volumetric resorption were measured by profilometry, with D experiencing the fastest rate of resorption, as determined by the slope of Eqn 6.1. The volumetric resorption of D was also the highest of any group at 25 days, and this was significantly higher than day 17 data. This suggests that the pits on D were deeper than on other groups. BG discs had the highest percent surface area resorption, but the rates of resorption were similar to that of TCP. With the BG discs, it was difficult to separate the effects of surface dissolution from that of osteoclast resorption, as both of these mechanisms likely contribute to degradation of the material. The BG discs also had the highest surface roughness of any group and this increased slightly over time. This also points to surface activity or dissolution playing a role in the remodeling of the substrate. Resorption on HA was the lowest of any group, with an approximately 7 fold lower rate than on D. The resorption measurements are similar to another study that found osteoclasts will resorb TCP but not HA (36). These data corroborate *in vivo* findings reporting that porous TCP ceramics remodel at a similar rate to osseous deposition, whereas HA based ceramics remain for a significantly longer timeframe (3). Additionally, *in vivo* investigation in a canine dental socket revealed more resorption and cellular activity in defects treated with BG as compared to HA (37). Finally, LV composites with allograft bone were fully degraded by a year while residual ceramic was visible in defects treated with Mastergraft (85% TCP, 15% HA) at 2 years in a sheep femoral plug model (Chapter 3).

The degradation products of calcium phosphates are used for *de novo* bone formation, unlike other bone graft substitutes (38). Phosphate ions have been shown to affect osteoblast apoptosis, osteopontin production, and new bone mineralization (26). Calcium ions aid in the regulation of osteoblast proliferation and osteoclast differentiation. However, the release of large numbers of calcium ions may interfere with resorption, which is of importance on matrices with higher rates of dissolution (36). Osteoclasts are able to sense Ca^{2+} levels, and high ionic concentration of calcium ions leads to decreased TRAP expression and morphological changes in osteoclasts due to negative feedback control mechanisms (39). While the increased Ca^{2+} concentration may inactivate osteoclasts, the increased presence of Ca, P, and Si ions may enhance osteoblast differentiation and activity (40). Most calcium phosphates exhibit little to no solubility in water while all dissolve in acids (11), which is of particular interest in osteoclast resorption where the resorption lacunae is an area of locally high acidity. The dissolution and degradation of ceramics and bioactive glasses may contribution to the balance of osteoclast and osteoblast activity and graft remodeling. The effect of dissolution products of bioactive glasses and ceramics on cell signaling pathways related to osteoblast/osteoclast growth and differentiation is an area for potential future studies.

One limitation of this study is the difficulty in seeding the cells directly onto the substrates of interest. It has previously been shown that cells do not attach directly onto inorganic substrates, rather they bind to the extracellular matrix (ECM) components, such as fibronectin and vitronectin, that are absorbed to the surface of biomaterials (25). The cellular attachment and differentiation of osteoclasts may be influenced by the binding of proteins, present in high concentrations in the growth media, to the inorganic matrices and the ECM produced by the differentiated MC3T3s. Another limitation of this study is the difficulty in separating the effects of BG dissolution and osteoclast resorption.

The aim of this study was to develop an inexpensive, standardized osteoclast differentiation assay to measure relative resorption rates on substrates of interest and test clinically relevant ceramics and bioactive glass. This *in vitro* assay will help to test bone grafts and aid in the development of biomaterials that experience balanced remodeling when implanted *in vivo*. Osteoclasts were evident in the MC3T3 and RAW 264.7 co-culture by 3 weeks, with the addition of VD3 stimulating the MC3T3s to drive osteoclast differentiation of the monocyte cell line (20). Resorption was quantified by optical profilometry on D, TCP, HA, and BG. The rate of resorption on D, the control for native bone, was twice as high as that on TCP and BG and 7 fold higher than resorption on HA. In ongoing studies, osteoclast resorption of RAW cells stimulated with (1) conditioned media from tumor cell culture or (2) supernatant from bacterial culture is being investigated.

Conclusion

Resorption by osteoclasts grown from a co-culture of MC3T3 and RAW 264.7 cells was evaluated on D, TCP, HA, and BG substrates. The co-culture assay produced multinucleated cells with a visible actin ring within 3 weeks on all substrates. Resorption was measured by optical profilometry with relative resorption rates determined on ceramics and bioactive glass. When compared to D, a control for host bone, rates on TCP and BG were approximately half while HA resorption was 7 fold lower. This study presents a new method to differentiate osteoclasts directly on matrices of interest and quantify relative resorption rates. The findings suggest osteoclasts are able to pit ceramic and bioactive glass substrates while ceramic composition significantly affects resorption rates.

References

1. Zimmermann, G., andMoghaddam, A. Allograft bone matrix versus synthetic bone graft substitutes. Injury **42, Supplement 2**, S16, 2011.
2. Yaszemski, M.J., Payne, R.G., Hayes, W.C., Langer, R., andMikos, A.G. Evolution of bone transplantation: molecular, cellular and tissue strategies to engineer human bone. Biomaterials **17**, 175, 1996.
3. Lichte, P., Pape, H.C., Pufe, T., Kobbe, P., andFischer, H. Scaffolds for bone healing: Concepts, materials and evidence. Injury **42**, 569, 2011.
4. Bose, S., Roy, M., andBandyopadhyay, A. Recent advances in bone tissue engineering scaffolds. Trends Biotechnol **30**, 546, 2012.
5. Dumas, J.E., Prieto, E.M., Zienkiewicz, K.J., Guda, T., Wenke, J.C., Bible, J., Holt, G.E., andGuelcher, S.A. Balancing the rates of new bone formation and polymer degradation enhances healing of weight-bearing allograft/polyurethane composites in rabbit femoral defects. Tissue Eng Part A **20**, 115, 2014.
6. Jones, J.R. Review of bioactive glass: from Hench to hybrids. Acta Biomater **9**, 4457, 2013.
7. Hing, K.A., Wilson, L.F., andBuckland, T. Comparative performance of three ceramic bone graft substitutes. The Spine Journal **7**, 475, 2007.
8. Fröhlich, M., Grayson, W.L., Wan, L.Q., Marolt, D., Drobnic, M., andVunjak-Novakovic, G. Tissue Engineered Bone Grafts: Biological Requirements, Tissue Culture and Clinical Relevance. Current stem cell research & therapy **3**, 254, 2008.
9. Larsson, S., andHannink, G. Injectable bone-graft substitutes: Current products, their characteristics and indications, and new developments. Injury **42, Supplement 2**, S30, 2011.
10. Lu, J., Descamps, M., Dejou, J., Koubi, G., Hardouin, P., Lemaitre, J., andProust, J.P. The biodegradation mechanism of calcium phosphate biomaterials in bone. Journal of biomedical materials research **63**, 408, 2002.
11. Barrère, F., van Blitterswijk, C.A., andde Groot, K. Bone regeneration: molecular and cellular interactions with calcium phosphate ceramics. International Journal of Nanomedicine **1**, 317, 2006.
12. Detsch, R., Hagmeyer, D., Neumann, M., Schaefer, S., Vortkamp, A., Wuelling, M., Ziegler, G., andEpple, M. The resorption of nanocrystalline calcium phosphates by osteoclast-like cells. Acta Biomaterialia **6**, 3223, 2010.
13. Hoppe, A., Güldal, N.S., andBoccaccini, A.R. A review of the biological response to ionic dissolution products from bioactive glasses and glass-ceramics. Biomaterials **32**, 2757, 2011.
14. Oonishi, H., Hench, L.L., Wilson, J., Sugihara, F., Tsuji, E., Matsuura, M., Kin, S., Yamamoto, T., andMizokawa, S. Quantitative comparison of bone growth behavior in granules of Bioglass®, A-W glass-ceramic, and hydroxyapatite. Journal of Biomedical Materials Research **51**, 37, 2000.
15. Talley, A.D., Kalpakci, K.N., Shimko, D.A., Zienkiewicz, K., Cochran, D., andGuelcher, S. Effects of rhBMP-2 Dose and Ceramic Composition on New Bone Formation and Space Maintenance in a Canine Mandibular Ridge Saddle Defect Model. Tissue Engineering 2016.
16. Takahashi, N., Akatsu, T., Udagawa, N., Sasaki, T., Yamaguchi, A., Moseley, J.M., Martin, T.J., andSuda, T. OSTEOBLASTIC CELLS ARE INVOLVED IN OSTEOCLAST FORMATION. Endocrinology **123**, 2600, 1988.

17. McSheehy, P.M., andChambers, T.J. 1,25-Dihydroxyvitamin D3 stimulates rat osteoblastic cells to release a soluble factor that increases osteoclastic bone resorption. Journal of Clinical Investigation **80**, 425, 1987.
18. Thomson, B.M., Mundy, G.R., andChambers, T.J. Tumor necrosis factors alpha and beta induce osteoblastic cells to stimulate osteoclastic bone resorption. The Journal of Immunology **138**, 775, 1987.
19. Thomson, B.M., Saklatvala, J., andChambers, T.J. Osteoblasts mediate interleukin 1 stimulation of bone resorption by rat osteoclasts. The Journal of Experimental Medicine **164**, 104, 1986.
20. Udagawa, N., Takahashi, N., Jimi, E., Matsuzaki, K., Tsurukai, T., Itoh, K., Nakagawa, N., Yasuda, H., Goto, M., Tsuda, E., Higashio, K., Gillespie, M.T., Martin, T.J., andSuda, T. Osteoblasts/stromal cells stimulate osteoclast activation through expression of osteoclast differentiation factor/RANKL but not macrophage colony-stimulating factor. Bone **25**, 517, 1999.
21. Kirstein, B., Chambers, T.J., andFuller, K. Secretion of tartrate-resistant acid phosphatase by osteoclasts correlates with resorptive behavior. J Cell Biochem **98**, 1085, 2006.
22. Gentleman, E., Fredholm, Y.C., Jell, G., Lotfibakhshaiesh, N., O'Donnell, M.D., Hill, R.G., andStevens, M.M. The effects of strontium-substituted bioactive glasses on osteoblasts and osteoclasts in vitro. Biomaterials **31**, 3949, 2010.
23. Botelho, C., Brooks, R., Spence, G., McFarlane, I., Lopes, M., Best, S., Santos, J., Rushton, N., andBonfield, W. Differentiation of mononuclear precursors into osteoclasts on the surface of Si-substituted hydroxyapatite. Journal of biomedical Materials research part A **78**, 709, 2006.
24. Friederichs, R.J., Brooks, R.A., Ueda, M., andBest, S.M. In vitro osteoclast formation and resorption of silicon-substituted hydroxyapatite ceramics. J Biomed Mater Res A 2015.
25. Fuller, K., Ross, J.L., Szewczyk, K.A., Moss, R., andChambers, T.J. Bone is not essential for osteoclast activation. PLoS One **5**, e12837, 2010.
26. Jensen, S.S., Gruber, R., Buser, D., andBosshardt, D.D. Osteoclast-like cells on deproteinized bovine bone mineral and biphasic calcium phosphate: light and transmission electron microscopical observations. Clinical Oral Implants Research **26**, 859, 2015.
27. Wilson, S.R., Peters, C., Saftig, P., andBromme, D. Cathepsin K activity-dependent regulation of osteoclast actin ring formation and bone resorption. J Biol Chem **284**, 2584, 2009.
28. Pascaretti-Grizon, F., Mabilleau, G., Basle, M.F., andChappard, D. Measurement by vertical scanning profilometry of resorption volume and lacunae depth caused by osteoclasts on dentine slices. Journal of Microscopy **241**, 147, 2011.
29. Pavlos, N.J., Cheng, T.S., Qin, A., Ng, P.Y., Feng, H.-T., Ang, E.S., Carrello, A., Sung, C.-H., Jahn, R., andZheng, M.-H. Tctex-1, a novel interaction partner of Rab3D, is required for osteoclastic bone resorption. Molecular and cellular biology **31**, 1551, 2011.
30. Jensen, E.D., Pham, L., Billington, C.J., Jr., Espe, K., Carlson, A.E., Westendorf, J.J., Petryk, A., Gopalakrishnan, R., andMansky, K. Bone morphogenic protein 2 directly enhances differentiation of murine osteoclast precursors. J Cell Biochem **109**, 672, 2010.
31. Kogawa, M., Anderson, P.H., Findlay, D.M., Morris, H.A., andAtkins, G.J. The metabolism of 25-(OH)vitamin D3 by osteoclasts and their precursors regulates the differentiation of osteoclasts. The Journal of Steroid Biochemistry and Molecular Biology **121**, 277, 2010.
32. Detsch, R., Mayr, H., andZiegler, G. Formation of osteoclast-like cells on HA and TCP ceramics. Acta Biomaterialia **4**, 139, 2008.

33. Pham, L., Kaiser, B., Romsa, A., Schwarz, T., Gopalakrishnan, R., Jensen, E.D., andMansky, K.C. HDAC3 and HDAC7 have opposite effects on osteoclast differentiation. Journal of Biological Chemistry **286**, 12056, 2011.
34. Bohner, M., Galea, L., andDoebelin, N. Calcium phosphate bone graft substitutes: Failures and hopes. Journal of the European Ceramic Society **32**, 2663, 2012.
35. Winkler, T., Hoenig, E., Gildenhaar, R., Berger, G., Fritsch, D., Janssen, R., Morlock, M.M., andSchilling, A.F. Volumetric analysis of osteoclastic bioresorption of calcium phosphate ceramics with different solubilities. Acta Biomaterialia **6**, 4127, 2010.
36. Yamada, S., Heymann, D., Bouler, J.M., andDaculsi, G. Osteoclastic resorption of calcium phosphate ceramics with different hydroxyapatite/β-tricalcium phosphate ratios. Biomaterials **18**, 1037, 1997.
37. Santos, F.A., Pochapski, M.T., Martins, M.C., Zenóbio, E.G., Spolidoro, L.C., andMarcantonio Jr, E. Comparison of Biomaterial Implants in the Dental Socket: Histological Analysis in Dogs. Clinical Implant Dentistry and Related Research **12**, 18, 2010.
38. Bohner, M. Resorbable biomaterials as bone graft substitutes. Materials Today **13**, 24, 2010.
39. Zaidi, M., Adebanjo, O.A., Moonga, B.S., Sun, L., andHuang, C.L.H. Emerging Insights into the Role of Calcium Ions in Osteoclast Regulation. Journal of Bone and Mineral Research **14**, 669, 1999.
40. Chen, Q.Z., Efthymiou, A., Salih, V., andBoccaccini, A.R. Bioglass®-derived glass–ceramic scaffolds: Study of cell proliferation and scaffold degradation in vitro. Journal of Biomedical Materials Research Part A **84A**, 1049, 2008.

CHAPTER VII

INJECTABLE, SETTABLE POLYURETHANE BIOCOMPOSITES DELIVERING rhBMP-2 FOR POSTEROLATERAL SPINAL FUSION IN RABBITS.

Introduction

From 1998 to 2008 the number of spinal fusion hospital discharges in the United States jumped from 64.5 per 100,000 adults to 135.5 (1). Spinal fusion surgeries are most often performed to treat degenerative conditions like disc degeneration, spinal stenosis, and degenerative spondylolisthesis, with complications reported in approximately 4% of cases (2). The gold standard treatment consists of autograft bone that is osteoconductive, osteogenic, and osteoinductive, but autograft requires a secondary for harvest and it cannot be delivered using minimally invasive surgical (MIS) techniques. While MIS posterolateral fusion (PLF) surgeries could potentially decrease muscle destruction and length of hospital stays, there are no studies comparing the outcomes of MIS and conventional approaches (3). Thus, there is considerable interest in the development of new materials that can be delivered by MIS techniques while also withstanding the compressive forces of the posterior musculature and contributing to fusion (4).

Previously studied tissue engineering approaches for spinal fusion include ceramics, polymers, demineralized bone, osteoinductive growth factors, stem cells, and gene therapy, but persuasive evidence for clinical use has not provided for many of these treatment options (5). Ceramics such as hydroxyapatite (HA) and β-tricalcium phosphate (β-TCP) are often studied for bone grafting applications, including spinal fusions, as they are osteogenic, strong, and resorbable (4, 6, 7). Polyurethanes (PUR) are a biodegradable, biocompatible class of polymers frequently studied for bone grafting applications (8, 9). PUR biocomposites are injectable and can fill a variety of defect sizes and shapes within clinically relevant working times of 5-10 min (10). PUR biocomposites with allograft, ceramic, or bioglass filler have been successfully tested in a number of animal models including rabbit femoral plug defects (11, 12), canine mandibular defects (13), and sheep femoral condyle defects (14).

The osteoinductive growth factor recombinant human bone morphogenetic protein-2 (rhBMP-2) has previously been shown to enhance fusion in the lumbar spine while reducing surgery time, blood loss, and hospital stays (15, 16). Clinical use of rhBMP-2 in spinal fusions began in 2002, with almost one third of spinal fusion procedures involving rhBMP-2 by 2006 (17). A non-human primate spinal fusion study indicated that the acelluar collagen sponge (ACS) carrier of rhBMP-2 leads to insufficient fusion due to the compressive forces of the musculature (4). RhBMP-2 is FDA approved for delivery via an ACS delivered within a metallic tapered spinal fusion cage (LT-CAGE™, Medtronic). RhBMP-2 delivered via a LV graft decreases bolus growth factor release when compared to a clinical control, an acellular collagen sponge (Chapter 4) which may enhance healing and reduce side effects associated with rhBMP-2 delivery. Additionally, LV grafts augmented with a clinically relevant dose of rhBMP-2 maintain the height and width of the host ridge and promote healing without the need for external fixation in canine ridge defects (18).

Due to the limited treatment options available for MIS techniques for spinal fusion procedures, there is a clinical need for new bone graft substitutes. In this study, we investigated injectable LV/ceramic (CM) and LV/BG composites augmented with 430 μg/ml rhBMP-2 as injectable, settable bone grafts for spinal fusion in a single level rabbit posterolateral lumbar spine model. The LV grafts set in approximately 10 minutes after injection into the fusion site and have mechanical integrity such that additional fusion cages are unnecessary. We hypothesized that LV grafts would support fusion and new bone formation, and the effect would be enhanced with the presence of the longer lasting ceramic.

Experimental

Materials. Lysine-triisocyanate prepolymer (LTI-PEG, 21.7% NCO) was purchased from Ricerca Biosciences LLC (Painesville, OH). Glycerol, stannous octoate, ε-caprolactone, and APTES were purchased from Sigma-Aldrich (St. Louis, MO). Glycolide and DL-lactide were supplied by Polysciences (Warrington, PA). Triethylene diamine (TEDA) and dipropylene glycol (DPG) were purchased from Sigma Aldrich and mixed to obtain a 10% (w/w) solution of TEDA in dry DPG. MASTERGRAFT® Mini Granules (ceramic, CM) were received from Medtronic Spinal and Biologics (Memphis, TN) and ground and sieved to 100 – 500 µm. 45S5 bioactive glass (BG) particles (150 – 212 µm) were purchased from Mo-Sci Corporation (Rolla, MO). Recombinant human bone morphogenetic protein-2 (rhBMP-2, INFUSE® kit) was received from Medtronic Spinal and Biologics (Memphis, TN).

Synthesis of polyester triol. The polyester triol was synthesized as described previously (19, 20). Briefly, glycerol was mixed with ε-caprolactone, glycolide, and DL-lactide monomers under argon at 140°C for 40 hrs. The subsequent polyester triol was cooled, washed 3x with hexane, and dried in a vacuum oven at 80°C for 48 hrs. The backbone of the polyester was comprised of 70% ε-caprolactone, 20% glycolide, and 10% DL-lactide, with a molecular weight of 450 g mol^{-1}.

Surface modification of bioactive glass. The surface of the bioactive glass particles was modified as described previously (21-23). Briefly, 45S5 BG particles were cleaned via sonication in a mixture of acetone in deionized (DI) water (95 vol%) and rinsed three times in DI water by sonication. Next, particles were silanized in a solution of APTES for 5 h at room temperature, rinsed with ethanol, and annealed at 100 °C for 1 h. For the surface-initiated ring-opening polymerization, a mixture of 1:1000 M Sn(Oct)2: dried ε-caprolactone and a 0.83:1 weight ratio of Sil-BG:ε-caprolactone was reacted while stirring at 110 °C. The polymerization time of 24 hrs corresponded to a final poly(ε-caprolactone) (PCL) molecular weight of 19,225 g mol^{-1}. Non-grafted, excess PCL was extracted with chloroform and particles were dried at 40 °C for 24 h.

Fabrication of low-viscosity (LV) bone grafts. The components of the LV grafts were mixed in a two-step method. In the first step, the polyester triol, matrix particles (either 45 wt% CM or 45 wt% BG), and TEDA (1.1 pphp) were added to a 10-mL cup and mixed by hand for 30 s. The LTI-PEG and lyophilized rhBMP-2 were added to the cup and mixed by hand for 60 s. The index (ratio of isocyanate:hydroxide equivalents x 100) was set at 115. For material characterization, the reactive mixture was mixed with 3 pphp of DI water (to simulate *in vivo* curing in the presence of moisture at the defect site), loaded into a straight bore syringe, and injected into a 6-mm vial. These samples were allowed to cure for 24 h prior to cutting.

Rheological analysis. To test the viscosity of the initial composites, triplicate samples were prepared without catalyst to prevent curing. The prepolymer, polyol, and solid filler were mixed by hand for 60 s and poured between 40-mm cross-hatched parallel plates on a TA Instruments AR2000ex rheometer (New Castle, DE). The plates were compressed to a gap of 1000 µm and subjected to a dynamic frequency sweep (0.5 to 100 rad sec^{-1}) at 25°C with controlled strain amplitude of 0.02%. A Cox-Merz transformation was applied to the collected dynamic data to obtain the steady state viscosity (η, Pa*s) as a function of shear rate (γ, s^{-1}).

The curing profile of the LV composites was also determined using a rheometer. For these composites the polyol, catalyst, and filler were mixed by hand initially for 30 s. The prepolymer was added and the samples were mixed by hand for 60 s. Reactive samples were loaded onto 25-

mm disposable aluminum plates and compressed to a gap of 1000 µm. An oscillatory time sweep was run on triplicate samples with a frequency of 1 Hz and a controlled amplitude of 1% strain. The storage (G') and loss (G'') moduli were collected over time. The working time was defined as the cross-over point of G' and G''. The tack-free time (TFT) of LV/BG and LV/CM composites was measured by hand. Reactive samples were mixed as described above, loaded into a straight bore syringe, and injected into 6mm vials for cure. The time after mixing at which the composite no longer adhered to an external object was defined as the TFT. Triplicate samples were run for each group and statistical difference was measured by a t-test.

Evaluation of LV bone grafts in a rabbit spinal fusion model. Six skeletally mature rabbits were used in this study. All surgical and care procedures were carried out under aseptic conditions according to the approved IACUC protocol. Treatment groups are listed in Table 7.1. The individual components of the LV grafts were gamma-irradiated at a dose of 25 kGY prior to surgery to ensure sterility. The bilateral, single level spinal fusion model in rabbits has been previously established (24). The soft tissue and longissimus muscle were retracted to expose the medial aspect of the transverse processes. The fusion site was decorticated with a motorized burr. The polyurethane components were mixed along with the lyophilized growth factor, packed into a syringe, and injected onto the site over the intertransverse ligament with the graft spanning the L5 and L6 transverse processes. The fusion sites were filled with LV/CM or LV/BG at a dose of 430 µg/ml rhBMP-2 (n=3 animals per group, bilateral sites). The injected composite foamed to a final volume of ~ 3 cc per fusion site after the reaction was complete. Computed tomography (CT) scans were run at 0, 4, and 8 weeks. The rabbits were euthanized after 8 weeks and evaluated with radiographs. Success of the spinal fusion was determined by manual palpation by experience surgeons. Motion of the L5-L6 segment was determined by gentle flexation of the fusion site. A successful union was specified as cases where no movement at the intervertebral disc was present. The spines were extracted, fixed in 10% formalin, and cut in half along a sagittal plane (along the spinal column) to separate the left and right side fusion bodies so that µCT scans could be run. The bones were fixed for 2 weeks prior to processing for histology.

Table 7.1. Rabbit spinal fusion *in vivo* study design and LV composite physical characteristics

Treatment Group	**Particles**	**Particle diameter (µm)**	**% Matrix**	**Viscosity at 5s^{-1} (Pa*s)**	**TFT (min)**	**Working time (min)**	**n 8 weeks**
LV/CM	Mastergraft	100-500	45	N/A	9.59 ± 0.47	N/A	3
LV/BG	Bioglass	150-212	45	65.73 ± 4.17	10.32 ± 0.78	11.52 ± 0.34	3

Micro-Computed Tomography (µCT) Analysis. A µCT50 (SCANO Medical, Basserdorf Switzerland) was used to acquire scans of the extracted spines in formalin at 70 kVp energy, 200 µA source current, 1000 projections per rotation, 800 ms integration time, and an isotropic voxel size of 24.2 µm. Axial images were reconstituted using manufacturer provided software. Attenuation values were converted to tissue mineral density (TMD) through calibration with hydroxyapatite (HA) phantoms with densities of 0 to 780 mg HA cm^{-3} (calibrations checked weekly).

Histology. After fixation in formalin, the explanted spines were dehydrated in a graded series of ethanol and embedded in poly(methylmethacrylate) (PMMA). Using an Exakt band saw, transverse sections were cut from each block in the midline of the fusion (halfway between L5 and L6) using the µCT images as reference. The sections were then ground and polished to <100 µm using an Exakt grinding system and stained with Sanderson's rapid bone stain. New bone stained red, residual CM stained black, and infiltrating cells stained blue. Remaining BG particles appeared white and did not absorb the stain. Histological sections were used to visualize the amount of new bone formed in the fusion body and the residual CM and BG particles in the graft site.

Results

Rheological analysis. LV/BG samples were testing with and without catalyst to examine cure profiles and initial flow characteristics of the composites. It was not possible to test LV/MG composites due to the large size of the particles (100-500 µm) and granularity of the mixture. Figure 7.1 shows representative curves for the initial viscosity and cure profile of the LV/BG graft. As expected, LV/BG composites exhibited shear thinning properties over the tested shear rates. The viscosity of the initial LV/BG composite was 65.73 ± 4.17 Pa*s (evaluated at 5 s^{-1}). The working time of the composites was determined as the cross-over point of the storage and loss moduli. The working times and TFT associated with the cure profile of LV/BG and LV/CM are listed in Table 7.1. The TFT for LV/CM was lower than that of LV/BG, but not significantly. The working time for the LV/BG composites was approximately a minute longer than the TFT due to the difference in the methods used to determine the two properties.

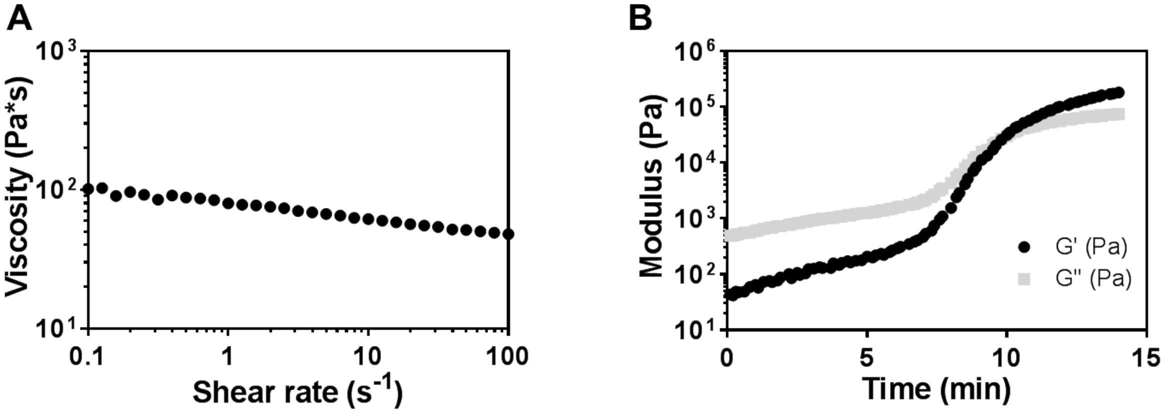

Figure 7.1. Rheological analysis of LV/BG composites. (A) Representative graph of initial flow characteristics and (B) cure profile of reactive composite (2.5 min after the start of mixing).

Assessment of Fusion. Success of the spinal fusion is shown in Figure 7.2. A complete union was apparent in all samples as determined by manual palpation of the fusion body after the samples were explanted.

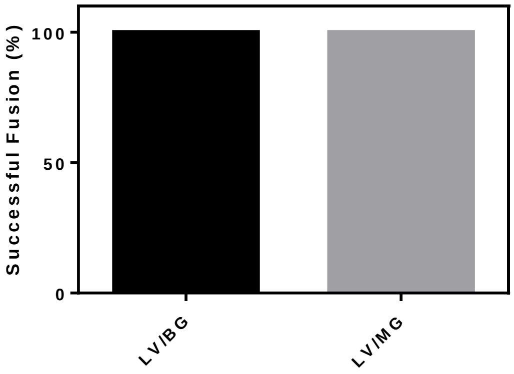

Figure 7.2. Success of fusion union as determined by manual palpation of explanted samples.

CT analysis. CT scans of all animals were run at 0, 4, and 8 weeks after the delivery of the bone graft (Figure 7.3). All samples showed a significant increase of bone over the 8 weeks of the study, although the 3D rendering of the fusion site is limited by the low resolution (500 µm) of the CT scans. Due to the foaming reaction of the material the grafts expanded outside of the fusion delivery site. The expansion is visible on the 3D CT renderings of the grafts at 4 and 8 weeks where the grafts appear to have expanded outward from the boundary of the transverse processes. By 8 weeks, some voids are visible in the CT scans. The new bone could not be differentiated from the CM or BG particles by CT analysis, since the scans recognized all radiopaque mineralized tissue or graft particles.

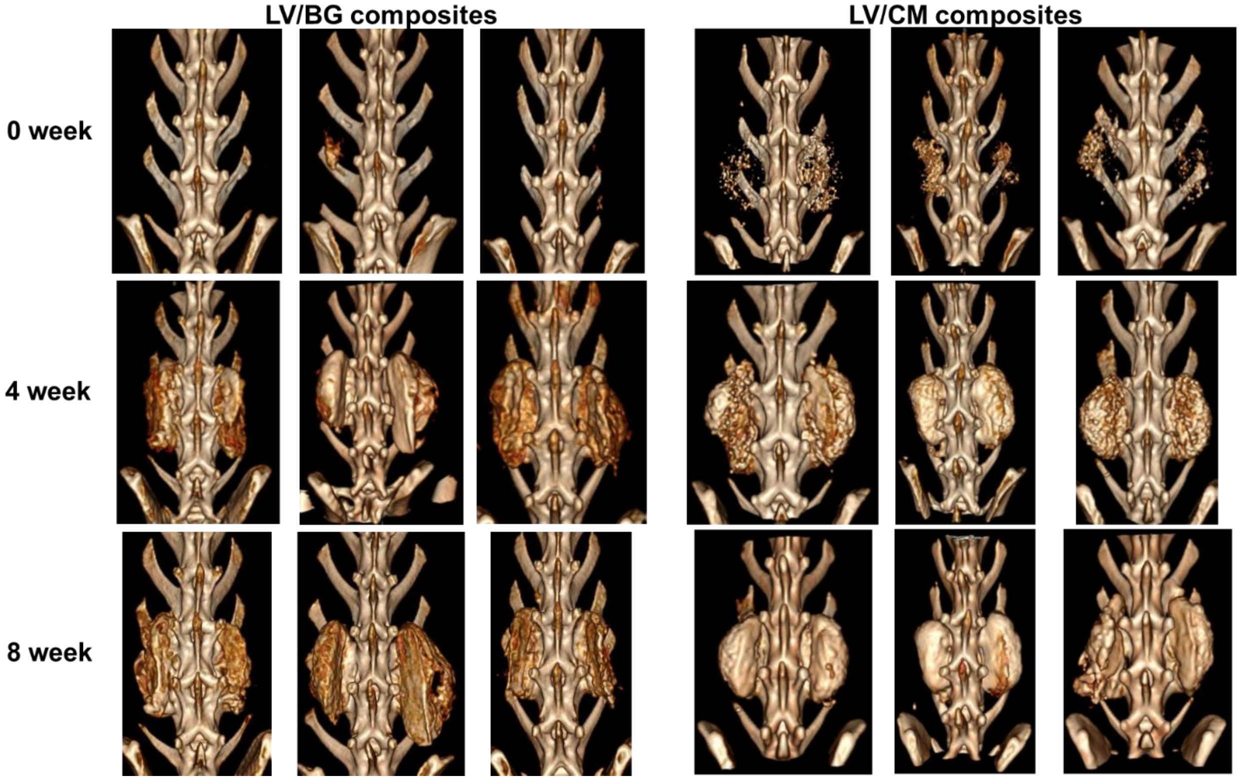

Figure 7.3. 3D Renderings of CT scans taken at 0, 4, and 8 weeks after the delivery of the bone graft to the fusion site for all LV/BG and LV/CM composites.

Radiographs. The Fusion sites were evaluated by radiography at 8 weeks (Figure 7.4). Bright white particles, residual CM, are visible within the animals treated with the LV/CM composites. The expansion of the graft outside the fusion site is also evident, particularly for the LV/CM composites. The new bone could not be differentiated from the BG or CM particles by radiography. There was large variability among samples for the size and position of the grafts within the fusion site.

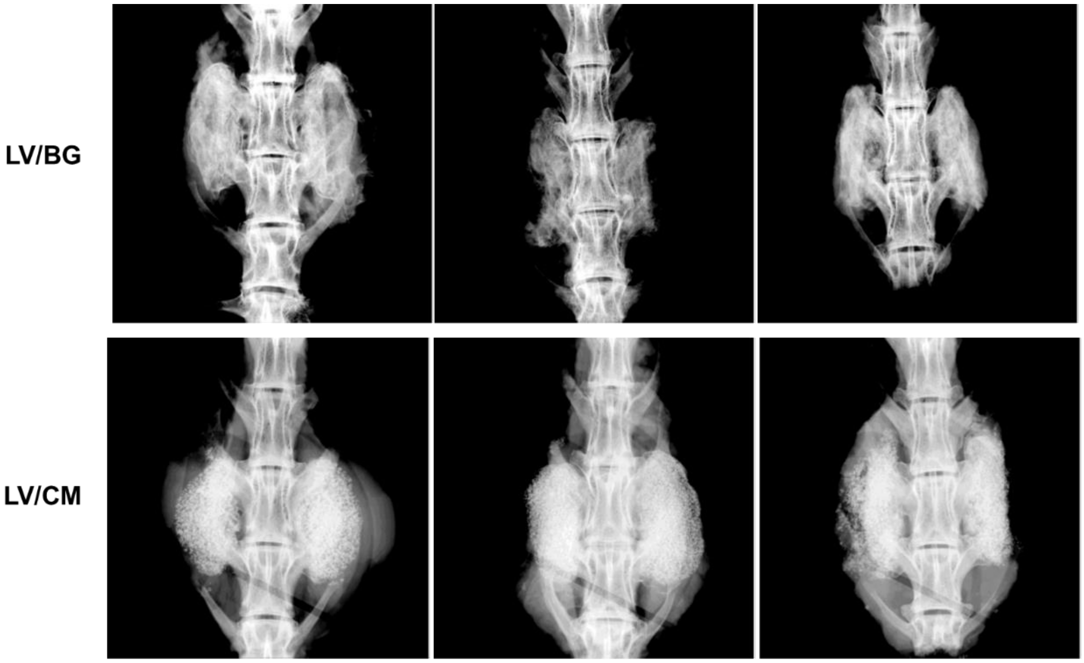

Figure 7.4. Radiographs of rabbit spinal fusion sites at 8 weeks for all LV./BG and LV/CM samples.

Micro-Computed Tomography (μCT) Analysis. Images of μCT scans all of the left fusion bodies are shown in Figure 7.5. Images of the sagittal (top row), coronal (middle row) and transverse (bottom row) show the presence of ossified tissue and residual solid matrix particles. A significant amount of residual CM is evident (bright white particles) within animals treated with LV/CM composites. Some new bone is visible, particularly around the boundary of the composites close to the spinal column. The interior of the grafts looks to be comprised mainly of islands of residual matrix particles without connectivity that would suggest new bone formation. The fusion bone is most easily seen in the coronal sections (white arrows), where the transverse spinal processes (SP) look to be connected by a bridge of new bone.

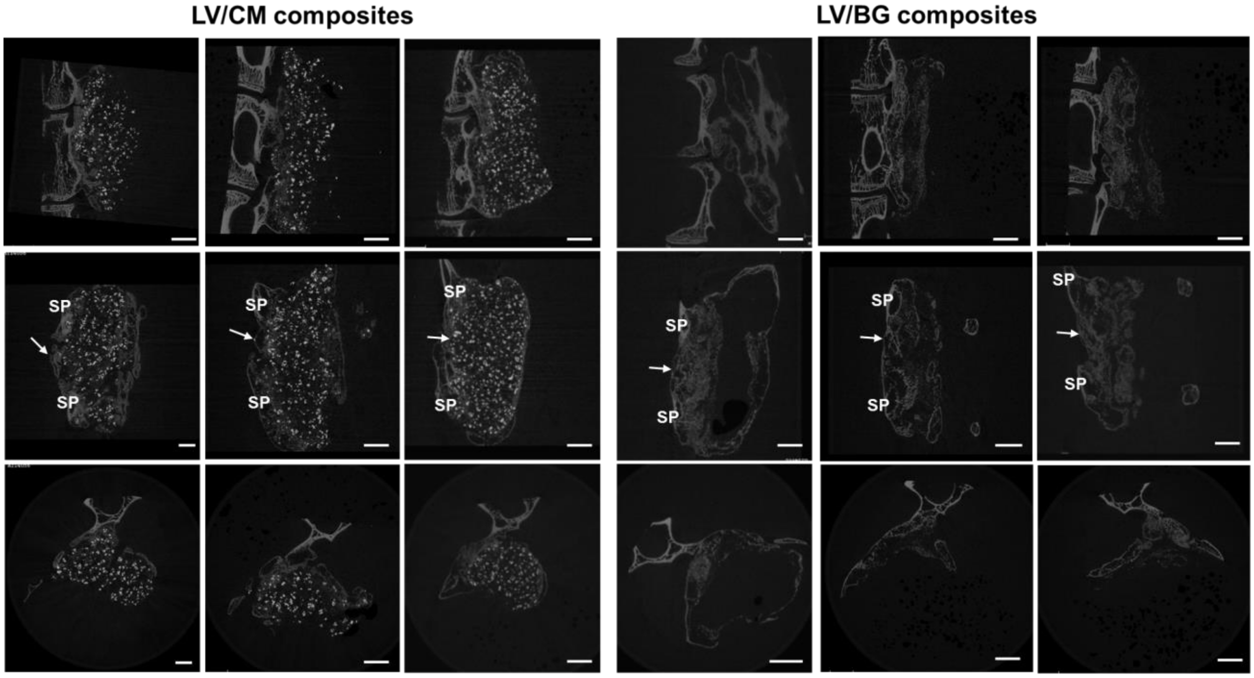

Figure 7.5. µCT images of all of the left fusion bodies for LV/CM and LV/BG composites in the sagittal (top), coronal (middle) and transverse (bottom) planes. Transverse spinal processes (SP) and the fusion bone between the processes (white arrows) are denoted in coronal sections. The scale bar represents 5 mm.

Histology. Representative low magnification histology images of sections cut in the transverse plane (Figure 7.6) show new bone formation (white arrows) which is part of the fusion volume between the two transverse processes. Cellular infiltration (blue) is visible throughout the graft. Large CM particles are still visible within the LV/CM groups while it is difficult to detect BG particles at the low magnification. The interior of the grafts is infiltrated by cells, but no new bone is present. Some fibrous tissue (green) is present in the interior of the defect in the LV/BG composites. No residual polymer was visible in any of the defects. The LV/CM samples appeared to have a defined border around the graft, with some new bone visible surrounding the injection volume. The LV/BG samples had less of a defined graft boundary and seemed to have a smaller graft volume that LV/CM samples.

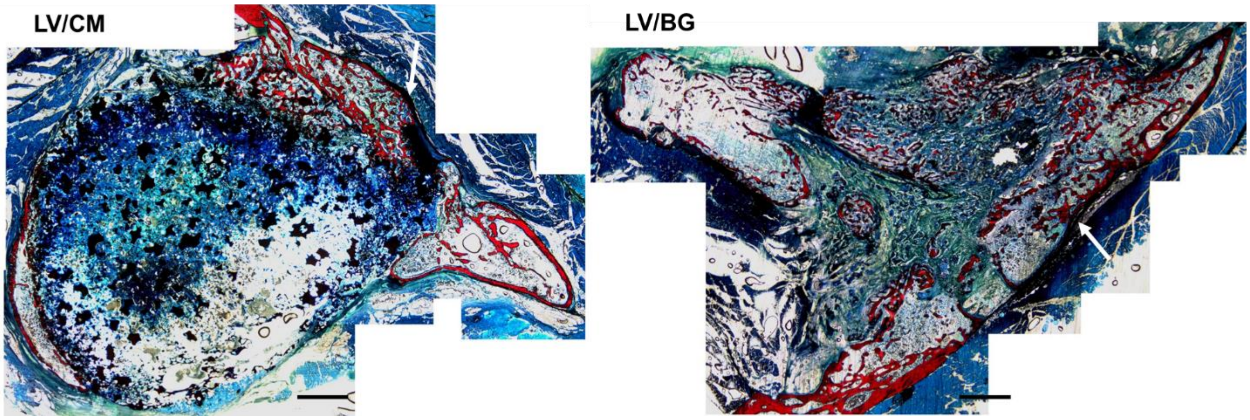

Figure 7.6. Low magnification images of transverse histology sections for LV/CM and LV/BG composites. The white arrows point to the new bone formed as part of the fusion body between the two transverse processes. Cells are stained blue, residual MG is black, bone is red, and BG is transparent/white. Fibrous tissue stains green.

High magnification images of histological sections are shown in Figure 7.7. Some CM particles are visibly incorporated into new bone at both 10x and 20x magnification. The new bone appears to be growing off of the ceramic surface. Some BG particles are adjacent to new deposition (10x), while some are surrounded by cells and soft tissue (20x) in the interior of the defect.

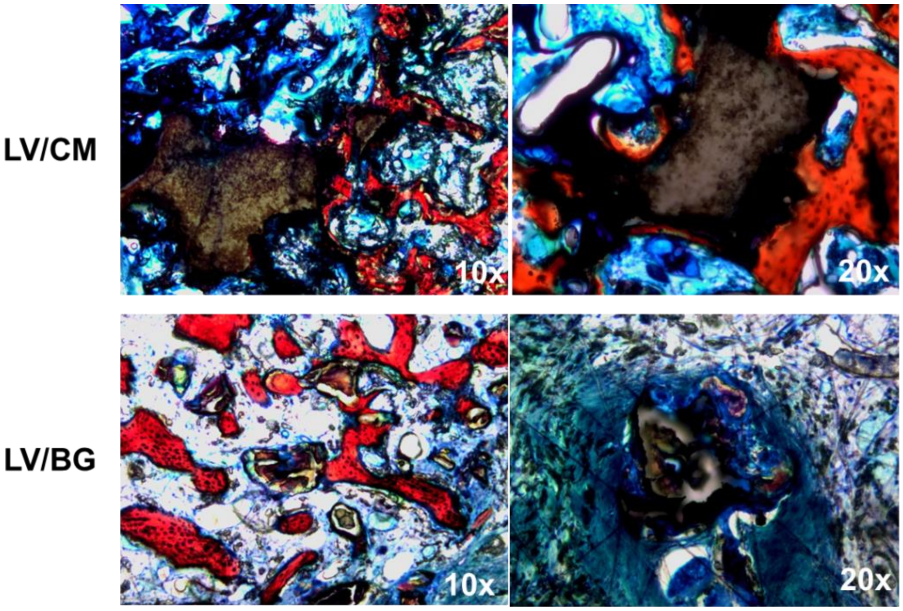

Figure 7.7. High magnification images of transverse histology sections for LV/CM and LV/BG composites at 10x and 20x. Cells are stained blue, residual MG is black, bone is red, and BG is transparent/white. Fibrous tissue stains green.

Discussion

Surgeons have been using autograft in posterolateral spinal fusions since 1911 due to the osteogenicity, osteoconductivity, and osteoinductivity of autologous bone (26). MIS posterolateral spinal fusions are postulated to decrease complications and length of hospital stays; however, autograft cannot be delivered using MIS techniques (3). We have previously described polyurethane biocomposites for bone regeneration in a variety of animal models (27-29). These composites can be injected in a defect and harden within 5- 10 minutes (12). Additionally, low viscosity (LV) grafts with a modulus of 1 MPa and higher supported space maintenance and prevented soft tissue prolapse in a canine mandibular ridge model (13). The aim of the present study was to investigate the effects of ceramic loading on union in a rabbit spinal fusion model using an injectable, settable LV graft.

The working time and TFT measured by rheometry and manual analysis of the setting composites showed that the biocomposite hardens within a clinically relevant working time of approximately 10 min, which corresponds with previous measurements of polyurethane reaction kinetics (10). The setting times of the LV grafts are within the ranges of clinically available bone cements that have mixing times of 2-3 minutes and setting times of 5-8 minutes (30). The viscosity of 65.7 Pa*s measured for the initial (non-cure) LV/BG is consistent with data obtained for LV/allograft composites (11). Poly(methyl methacrylate) is commonly used in the spine for vertebroplasty to alleviate pain and strengthen vertebrae, although the efficacy of this technique has been questioned (31). The initial viscosity of the polyurethane biocomposite is lower than that of PMMA cements, which have viscosities in the range of 100-150 Pa*s (32).

The commercially available acellular collagen sponge (ACS) rhBMP-2 delivery system is ineffective in promoting sufficient spinal fusion, even at clinically relevant rhBMP-2 doses, due to soft tissue compression of the collagen (33). A previous study using 430 µg/mL rhBMP-2 delivered via ACS with a ceramic bulking agent resulted in successful fusion in a rabbit arthrodesis model, as determined by manual palpation and radiography (34). Additionally, patients treated with ACS and a compression resistant matrix exhibit better fusion at 1 year as compared to patients treated with autograft (4). However, the ACS/ceramic grafts are not injectable and could not be combined with MIS techniques. In this study, LV biocomposites with 430 µg/mL rhBMP-2 supported spinal fusion in a rabbit posterolateral spinal fusion model at 8 weeks, as measured by palpation. Additionally, images of µCT scans shown new bone forming in the fusion site between the transverse processes. These grafts were injected into the fusion site and supported new bone formation while providing mechanical stability to resist compression by the musculature. This has been shown previously in a canine mandibular ridge defect where LV grafts delivering a clinically relevant dose of rhBMP-2 (400 μg/mL) supported new bone formation and preserved the height and width of the mandibular ridge (13). The mandibular ridge defects were surrounded on 3 sides by bony walls, while the posterolateral spine fusion model is a more challenging space to grow bone due to limited bony surface area.

By 8 weeks, some of the CT scans showed visible voids within the graft site. Additionally, the histology sections showed the interior of the graft area was devoid of cellular infiltration and new bone deposition. No significant differences were seen in grafts treated with CM as compared to those treated with BG. Residual polymer was not observed in any of the animals at 8 weeks. Previous studies have shown degradation of lysine-derived polyurethane is dependent in part on cell-mediated processes (35) and is completely degraded by 4 months in canine mandibular ridge defect (13). A study testing LV/allograft and LV/CM in a sheep femoral plug defect showed that healing was variable with LV grafts, likely due to the low volume percent of osteoconductive matrix within the defect space, and large voids were present in the graft space that did not experience significant new bone formation (Chapter 3). In the current study, residual CM particles (15% β-tricalcium phosphate (TCP) and 85% hydroxyapatite (HA)) were visible within the graft while BG particles were significantly degraded. This is in agreement with a previous study that showed faster remodeling of BG than hydroxyapatite (HA) *in vivo* (36). In a canine mandibular ridge defect, BG particles were primarily degraded by 4 months while MG particles remained (13). *In vitro* osteoclasts assays have shown that resorption rates are similar between TCP and BG while HA resorption is four-fold slower (Chapter 6).

This study was designed to answer the question of whether injectable low-viscosity (LV) PUR/ceramic and PUR/bioglass composites augmented with rhBMP-2 could promote fusion in a single level rabbit posterolateral spinal fusion model. Successful union was achieved with both

LV/CM and LV/BG composites. One limitation of this study was the small sample size (n=3 per group). While there was significant cellular infiltration into the graft, new bone growth was limited to a small volume in close proximity to the spinal column. Additionally, the graft expanded outside of the fusion site due to the high foaming reaction associated with the reactive polyurethane. In a current study, polyurethane biocomposites are being studied as autograft extenders for rabbit spinal fusion. Using a catalyst with a high gel to blow ratio, non-foaming polyurethanes are being tested with and without ceramic in combination with autograft bone. The low expansion of the autograft extender is anticipated to lead to graft containment within the desired fusion site. Decreasing the expansion associated with the polyurethane reaction is expected to enhance new bone growth and fusion. Another limitation of this study is that the LV grafts were not compared to a clinical control, such as autograft. However, to our knowledge, this is the first study to describe an injectable, compression-resistant graft for posterolateral spinal fusion.

Conclusion

In this study, we investigated LV composites with ceramic or bioglass incorporating 430 μg/mL rhBMP-2 as injectable bone grafts in a single level rabbit posterolateral spinal fusion model. Successful union was achieved in animals treated with both LV/CM and LV/BG composites, as evidenced by manual palpation and μCT and histology images. LV grafts had the necessary mechanical integrity to support fusion even in the presence of the mechanical forces of the skeletal musculature. This study highlights the potential of LV composites with rhBMP-2 as injectable bone grafts for MIS posterolateral spinal fusion surgeries.

References

1. Rajaee, S.S., Bae, H.W., Kanim, L.E.A., andDelamarter, R.B. Spinal Fusion in the United States: Analysis of Trends From 1998 to 2008. Spine **37**, 67, 2012.
2. Wang, M.C., Chan, L., Maiman, D.J., Kreuter, W., andDeyo, R.A. Complications and mortality associated with cervical spine surgery for degenerative disease in the United States. Spine **32**, 342, 2007.
3. Skovrlj, B., Gilligan, J., Cutler, H.S., andQureshi, S.A. Minimally invasive procedures on the lumbar spine. World Journal of Clinical Cases : WJCC **3**, 1, 2015.
4. Glassman, S.D., Dimar, J.R., Carreon, L.Y., Campbell, M.J., Puno, R.M., andJohnson, J.R. Initial fusion rates with recombinant human bone morphogenetic protein-2/compression resistant matrix and a hydroxyapatite and tricalcium phosphate/collagen carrier in posterolateral spinal fusion. Spine **30**, 1694, 2005.
5. Miyazaki, M., Tsumura, H., Wang, J., andAlanay, A. An update on bone substitutes for spinal fusion. European Spine Journal **18**, 783, 2009.
6. Liao, S., Guan, K., Cui, F., Shi, S., andSun, T. Lumbar spinal fusion with a mineralized collagen matrix and rhBMP-2 in a rabbit model. Spine **28**, 1954, 2003.
7. Yuan, H., Fernandes, H., Habibovic, P., de Boer, J., Barradas, A.M., de Ruiter, A., Walsh, W.R., van Blitterswijk, C.A., andde Bruijn, J.D. Osteoinductive ceramics as a synthetic alternative to autologous bone grafting. Proc Natl Acad Sci U S A **107**, 13614, 2010.
8. Dumas, J.E., Zienkiewicz, K., Tanner, S.A., Prieto, E.M., Bhattacharyya, S., andGuelcher, S.A. Synthesis and characterization of an injectable allograft bone/polymer composite bone void filler with tunable mechanical properties. Tissue Engineering Part A **16**, 2505, 2010.
9. Bonzani, I.C., Adhikari, R., Houshyar, S., Mayadunne, R., Gunatillake, P., andStevens, M.M. Synthesis of two-component injectable polyurethanes for bone tissue engineering. Biomaterials **28**, 423, 2007.
10. Page, J.M., Prieto, E.M., Dumas, J.E., Zienkiewicz, K.J., Wenke, J.C., Brown-Baer, P., andGuelcher, S.A. Biocompatibility and chemical reaction kinetics of injectable, settable polyurethane/allograft bone biocomposites. Acta Biomaterialia **8**, 4405, 2012.
11. Prieto, E.M., Talley, A.D., Gould, N.R., Zienkiewicz, K.J., Drapeau, S.J., Kalpakci, K.N., andGuelcher, S.A. Effects of particle size and porosity on in vivo remodeling of settable allograft bone/polymer composites. Journal of Biomedical Materials Research Part B: Applied Biomaterials, n/a, 2015.
12. Dumas, J.E., Prieto, E.M., Zienkiewicz, K.J., Guda, T., Wenke, J.C., Bible, J., Holt, G.E., andGuelcher, S.A. Balancing the rates of new bone formation and polymer degradation enhances healing of weight-bearing allograft/polyurethane composites in rabbit femoral defects. Tissue Eng Part A **20**, 115, 2014.
13. Talley, A.D., Kalpakci, K.N., Shimko, D.A., Zienkiewicz, K., Cochran, D., andGuelcher, S. Effects of rhBMP-2 Dose and Ceramic Composition on New Bone Formation and Space Maintenance in a Canine Mandibular Ridge Saddle Defect Model. Tissue Engineering 2016.
14. Harmata, A., Ma, Y., Sanchez, C., Zienkiewicz, K., Elefteriou, F., Wenke, J., andGuelcher, S. d-amino Acid Inhibits Biofilm but not New Bone Formation in an Ovine Model. Clinical Orthopaedics and Related Research®, 1, 2015.
15. Shields, L.B.E., Raque, G.H., Glassman, S.D., Campbell, M., Vitaz, T., Harpring, J., andShields, C.B. Adverse Effects Associated With High-Dose Recombinant Human Bone Morphogenetic Protein-2 Use in Anterior Cervical Spine Fusion. Spine **31**, 542, 2006.

16. Hsu, W.K., Polavarapu, M., Riaz, R., Larson, A.C., Diegmueller, J.J., Ghodasra, J.H., andHsu, E.L. Characterizing the host response to rhBMP-2 in a rat spinal arthrodesis model. Spine **38**, E691, 2013.
17. Lad, S.P., Nathan, J.K., andBoakye, M. Trends in the use of bone morphogenetic protein as a substitute to autologous iliac crest bone grafting for spinal fusion procedures in the United States. Spine (Phila Pa 1976) **36**, E274, 2011.
18. Talley, A.D., Kalpakci, K.N., Zienkiewicz, K.J., Cochran, D.L., andGuelcher, S.A. Space Maintenance and New Bone Formation with Low-Viscosity, Compression-Resistant Bone Grafts in a Canine Mandibular Ridge Saddle Defect. Tissue Eng **Submitted**.
19. Guelcher, S., Srinivasan, A., Hafeman, A., Gallagher, K., Doctor, J., Khetan, S., McBride, S., andHollinger, J. Synthesis, in vitro degradation, and mechanical properties of two-component poly(ester urethane)urea scaffolds: effects of water and polyol composition. Tissue Eng **13**, 2321, 2007.
20. Guelcher, S.A., Patel, V., Gallagher, K.M., Connolly, S., Didier, J.E., Doctor, J.S., andHollinger, J.O. Synthesis and in vitro biocompatibility of injectable polyurethane foam scaffolds. Tissue engineering **12**, 1247, 2006.
21. Harmata, A.J., Ward, C.L., Zienkiewicz, K.J., Wenke, J.C., andGuelcher, S.A. Investigating the effects of surface-initiated polymerization of ε-caprolactone to bioactive glass particles on the mechanical properties of settable polymer/ceramic composites. Journal of Materials Research **29**, 2398, 2014.
22. Jiang, G., Evans, M., Jones, I., Rudd, C., Scotchford, C., andWalker, G. Preparation of poly (ε-caprolactone)/continuous bioglass fibre composite using monomer transfer moulding for bone implant. Biomaterials **26**, 2281, 2005.
23. Verné, E., Vitale-Brovarone, C., Bui, E., Bianchi, C., andBoccaccini, A. Surface functionalization of bioactive glasses. Journal of biomedical materials research Part A **90**, 981, 2009.
24. Boden, S.D., Schimandle, J.H., andHutton, W.C. An Experimental Lumbar Intertransverse Process Spinal Fusion Model: Radiographic, Histologic, and Biomechanical Healing Characteristics. Spine **20**, 412, 1995.
25. Bouxsein, M.L., Boyd, S.K., Christiansen, B.A., Guldberg, R.E., Jepsen, K.J., andMuller, R. Guidelines for assessment of bone microstructure in rodents using micro-computed tomography. J Bone Miner Res **25**, 1468, 2010.
26. Grabowski, G., andCornett, C.A. Bone graft and bone graft substitutes in spine surgery: current concepts and controversies. Journal of the American Academy of Orthopaedic Surgeons **21**, 51, 2013.
27. Brown, K.V., Li, B., Guda, T., Perrien, D.S., Guelcher, S.A., andWenke, J.C. Improving bone formation in a rat femur segmental defect by controlling bone morphogenetic protein-2 release. Tissue Eng Part A **17**, 1735, 2011.
28. Dumas, J.E., BrownBaer, P.B., Prieto, E.M., Guda, T., Hale, R.G., Wenke, J.C., andGuelcher, S.A. Injectable reactive biocomposites for bone healing in critical-size rabbit calvarial defects. Biomed Mater **7**, 024112, 2012.
29. Dumas, J.E., Prieto, E.M., Zienkiewicz, K.J., Guda, T., Wenke, J.C., Bible, J., Holt, G.E., andGuelcher, S.A. Balancing the Rates of New Bone Formation and Polymer Degradation Enhances Healing of Weight-Bearing Allograft/Polyurethane Composites in Rabbit Femoral Defects. Tissue Eng Part A **Not available - ahead of print**2013.

30. Mousa, W.F., Kobayashi, M., Shinzato, S., Kamimura, M., Neo, M., Yoshihara, S., andNakamura, T. Biological and mechanical properties of PMMA-based bioactive bone cements. Biomaterials **21**, 2137, 2000.
31. Kallmes , D.F., Comstock , B.A., Heagerty , P.J., Turner , J.A., Wilson , D.J., Diamond , T.H., Edwards , R., Gray , L.A., Stout , L., Owen , S., Hollingworth , W., Ghdoke , B., Annesley-Williams , D.J., Ralston , S.H., andJarvik , J.G. A Randomized Trial of Vertebroplasty for Osteoporotic Spinal Fractures. New England Journal of Medicine **361**, 569, 2009.
32. Boger, A., Bohner, M., Heini, P., Verrier, S., andSchneider, E. Properties of an injectable low modulus PMMA bone cement for osteoporotic bone. Journal of Biomedical Materials Research Part B: Applied Biomaterials **86B**, 474, 2008.
33. Martin, G.J.J., Boden, S.D., Morone, M.A., andMoskovitz, P.A. Posterolateral Intertransverse Process Spinal Arthrodesis with rhBMP-2 in a Nonhuman Primate: Important Lessons Learned Regarding Dose, Carrier, and Safety. Clinical Spine Surgery **12**, 179, 1999.
34. Kraiwattanapong, C., Boden, S.D., Louis-Ugbo, J., Attallah, E., Barnes, B., andHutton, W.C. Comparison of Healos/bone marrow to INFUSE (rhBMP-2/ACS) with a collagen-ceramic sponge bulking agent as graft substitutes for lumbar spine fusion. Spine **30**, 1001, 2005.
35. Hafeman, A.E., Zienkiewicz, K.J., Zachman, A.L., Sung, H.J., Nanney, L.B., Davidson, J.M., andGuelcher, S.A. Characterization of the degradation mechanisms of lysine-derived aliphatic poly(ester urethane) scaffolds. Biomaterials **32**, 419, 2011.
36. Santos, F.A., Pochapski, M.T., Martins, M.C., Zenóbio, E.G., Spolidoro, L.C., andMarcantonio Jr, E. Comparison of Biomaterial Implants in the Dental Socket: Histological Analysis in Dogs. Clinical Implant Dentistry and Related Research **12**, 18, 2010.

CHAPTER VIII

SUMMARY AND FUTURE DIRECTIONS

The work presented in this dissertation describes the use of polyurethane (PUR) composites, in particular those that have low viscosity (LV) and are injectable, as bone void fillers and growth factor carriers and discusses the remodeling characteristics of the different phases of the composites both *in vitro* and *in vivo.* As a result of the tailorability of the platform, these LV grafts can be used in a wide variety of clinical applications ranging from craniomaxillofacial reconstruction to orthopaedic injuries and spinal fusions.

In **Chapter III** we tested ceramic particles and LV grafts, aimed as bone void fillers, in an *in vivo* model over 2 years. LV/Mastergraft (ceramic – CM), LV/Allograft (A), and a ceramic control group (C) were implanted into femoral plug defects in sheep. We were able to study long term healing and bone regeneration with the ceramic granules alone, group C, and as part of a composite, group LV/CM. From this study we learned that a larger volume fraction of ceramic filler leads to more new bone and better, more reproducible healing. With the LV composites, there was inconsistent healing and voids present in some samples. To our knowledge this is the first study to look at the long term fate of the ceramic Mastergraft *in vivo,* where the majority of the ceramic was degraded by 2 years. While the optimal degradation profile of bone grafts has been debated, many researchers agree that bone grafts should degrade at a similar rate to new bone formation (1, 2). In this study, we show that healing is not impaired with a longer lasting ceramic phase.

The release kinetics of rhBMP-2 from LV grafts is described in **Chapter IV**. While growth factor delivered from the FDA approved acellular collagen sponge (ACS) exhibits a bolus release, the release is significantly extended when delivered with the LV grafts. When incorporated into the PUR network, there is an initial burst release of growth factor within a few days followed by a slower, extended release over approximately a month. This corresponds well with previous research that has shown that this pattern of release, with a small bolus followed by extended delivery, is desirable in bone regeneration (3, 4). We also established that the *in vivo* release is controlled by a combined mechanism, most likely due to Fickian diffusion and polymer degradation, while *in vitro* release of the growth factor is singularly controlled by Fickian diffusion. This points to the faster polymer degradation *in vivo*, which is postulated to be due to oxidative degradation through the release of reactive oxygen species (ROS) by infiltrating cells (5), than what can be expected due to hydrolytic degradation alone.

Once the release of growth factor from the LV grafts had been established, LV grafts with rhBMP-2 were tested in a canine saddle defect model (**Chapter V**). The defect site was successfully healed with LV composites containing either bioactive glass (BG) or ceramic matrix particles (CM) at a dose of 400 µg/mL rhBMP-2, which is the recommended dose with the collagen sponge delivery system in the canine. These grafts had a bulk modulus over 1 MPa and were able to maintain the host ridge height and width throughout the healing process, while ridge maintenance was not achieved with LV/BG or LV/CM grafts at a low dose of 100 µg/mL. The success of the grafts in this model illustrates the use of the injectable, LV grafts as delivery systems for rhBMP-2 for craniomaxillofacial applications without the need for additional external fixation such as that which would be required for a graft unable to prevent soft tissue prolapse (6, 7).

Through *in vivo* studies, we were able to get a general idea of cellular infiltration, graft degradation, and new bone deposition by histology and histomorphometry. However, these methods do not provide details regarding the fundamental mechanisms of graft biodegradation.

Chapter VI covers an osteoblast- osteoclast co-culture assay that was developed to test *in vitro* resorption of ceramics and bioactive glasses. Osteoclasts developed on bioglass, ceramics, and dentin (positive control for host bone) within 21 days. Quantitative analysis of resorption rates demonstrated the highest resorption on dentin, approximately half the rate on bioglass and tricalcium phosphate, and an order of magnitude lower rate on hydroxyapatite. Previous literature related to bioactive glass and ceramic resorption is inconsistent in both methodology and results. This study provides a new approach to standardize the study of *in vivo* resorption and calculate relative resorption rates on substrates of interest.

As an additional *in vivo* experiment, we tested injectable LV/BG and LV/CM grafts with 430 µg/mL rhBMP-2 in a single level posterolateral spinal fusion model in rabbits, as explained in **Chapter VII.** Fusion after 8 weeks was evident for all samples, as determined by manual palpation. Qualitatively, new bone was apparent for all samples at 4 and 8 weeks. This study was limited by high graft expansion due to the foaming of the PUR reaction with the high blowing power of the triethylene diamine catalyst. The expansion caused (1) the dilution of the osteoconductive ceramic and glass particles and (2) the enlargement of the graft from the specified defect area. The results were very promising even with these complications. To our knowledge this is one of the first injectable, compression resistant grafts that has been shown to be successful in a spinal fusion model and could support minimally invasive surgical techniques.

Proposed Future Work

Canine lateral ridge study

Along with the *in vivo* experiments described in this dissertation, we also have preliminary data from a study testing the effects of rhBMP-2 dose delivered from LV/CM composites against a clinical control, an acellular collagen sponge (ACS) with titanium mesh, in a canine lateral ridge augmentation model. While the ACS carrier is FDA approved for rhBMP-2 delivery, it does not have the necessary mechanical stability to be used independently in a site that will experiences compressive forces from soft tissue or musculature. The study design for the lateral ridge study is shown in Table 8.1. The lateral ridge augmentation model is less stringent than the saddle defect, but it is a more widely accepted model in the literature for medical devices intended for craniomaxillofacial applications (8, 9).

Table 8.1. In vivo study design for rhBMP-2 dose response from LV/CM grafts in a canine lateral ridge augmentation model against an acellular collagen sponge (ACS) control

Treatment Group	**Particles**	**rhBMP-2 dose (μg/mL)**	**n 16 weeks**
ACS	N/A	400	6
LV/CM	Mastergraft	0	6
LV/CM-L	Mastergraft	200	6
LV/CM-H	Mastergraft	400	6

The lateral ridge defect is a rigid preclinical model that requires two surgeries. In the first surgery there was bilateral extraction of the four mandibular premolars and a portion of the buccal plate was removed to simulate dental loss in humans resulting from chronic disease. In the second surgery, the previously created bone defects were accessed and debrided at which point (1) the LV/CM grafts were injected into the defects with the appropriate dose of rhBMP-2 (Figure 8.1) or (2) the rhBMP-2 was resuspended in sterile water and injected onto the ACS while the ACS was placed in the defect and covered with the titanium mesh to maintain the space surrounding the graft (Figure 8.1). The bones were harvested after 16 weeks with analysis by μCT and histology.

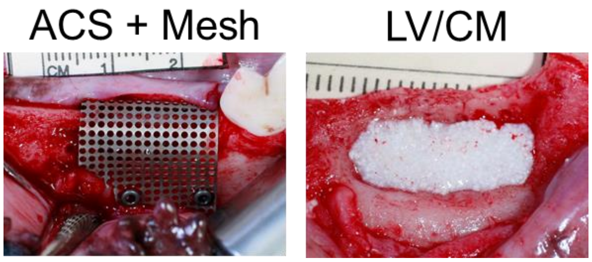

Figure 8.1**.** Surgical images of the exposed canine lateral ridge defects grafted with the acellular collagen sponge (ACS)/titanium mesh system and the LV/CM graft

Preliminary µCT images (Figure 8.2) of harvested bones show more new bone formation in defects treated with LV/CM grafts containing high doses of rhBMP-2 than those with a low dose. The ridge width was maintained with the ACS/titanium mesh system, although ectopic bone formation was seen in some samples (bone growing outside of the titanium mesh).

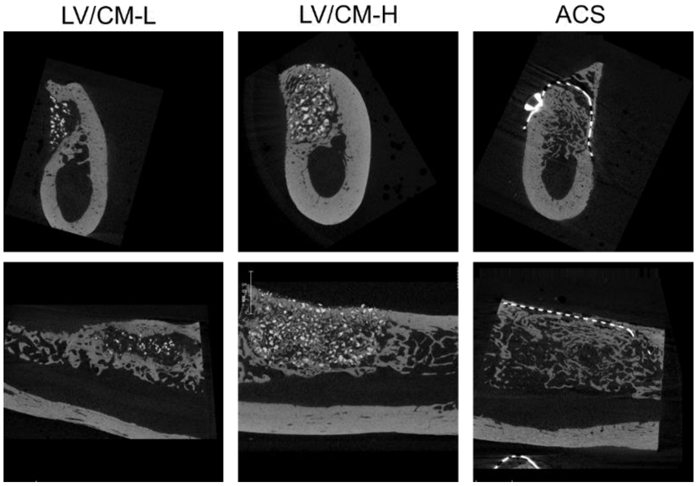

Figure 8.2**.** µCT images of harvested bones treated with LV grafts containing low or high doses of rhBMP-2 or the ACS/titanium mesh system.

Preliminary histology images (Figure 8.3) of harvested bones show new bone formation in defects treated with LV/CM-H and the ACS groups. New bone (red) was visible throughout the defect with residual CM (black) particles visible incorporated into the new bone. Fibrous tissue stained a greenish-brown color. The ridge width was seemingly maintained by both LV/CM-H and the ACS groups, with ectopic bone formation evident outside of the titanium mesh.

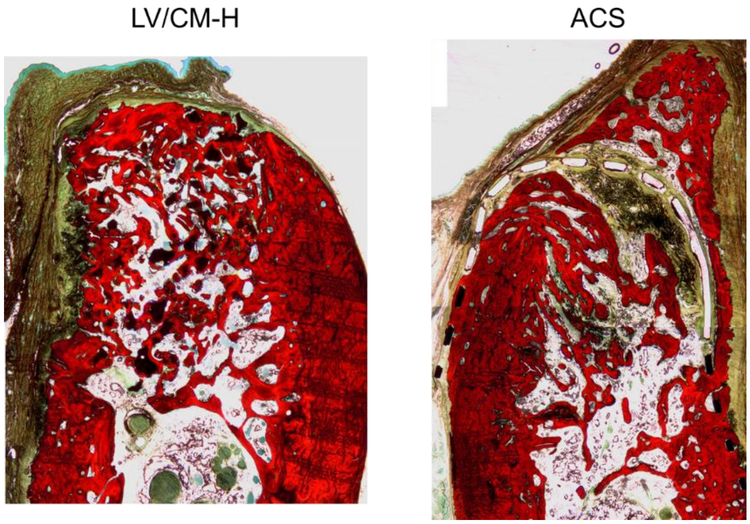

Figure 8.3**.** Low magnification histology images of harvested bones treated with LV/CM-H or ACS groups. Bone is stained in red, residual ceramic is black, and fibrous tissue is greenish brown.

Additional studies

Through numerous *in vivo* experiments, we revealed that LV grafts were potential candidates for both craniomaxillofacial and orthopaedic bone defects. With the current LV graft system there are difficulties in handling and delivering the composite due to the expansion of graft during the PUR reaction. It can be difficult to determine the appropriate graft volume to deliver to a defect site as the graft foams to nearly twice the initial volume. Additionally, it can be challenging to predict the degree of foaming due to variability in environmental conditions, such as humidity, and water present in the defect site. Currently, a new PUR platform is being tested that does not expand once delivered. The platform consists of a novel nanohydroxyapatite- lysine triisocyanate (nHA-LTI) hybrid prepolymer that is combined with polycaprolactone (PCL) (300 g/mol) in the presence of Iron (III) acetylacetonate, a catalyst with high gel:blow activity. The hybrid prepolymer/PCL scaffold can be further mixed with BG or CM particles to increase osteoconductivity of the graft. The nHA-LTI/PCL graft can be molded, like putty, or injected through a straight bore syringe with working times similar to those of the LV grafts. These handling properties are desirable for a number of applications, and the novel platform has implications in both orthopaedic and craniomaxillofacial grafting. Additionally, the inclusion of nanoparticles of HA better mimics the composition and morphology of host tissue. Bone is comprised of nanometer size inorganic components (mainly HA) within an organic matrix (mainly collagen), where the nanosized inorganic is believed to play a factor in the mechanical properties of bone as well as the bioactivity (10, 11).

The novel nHA-LTI platform is currently being tested in a rat calvarial defect as a rhBMP-2 delivery system. A previously study testing low-expansion LV/CM or LV/S grafts in a rat calvarial defect showed limited cell infiltration, graft degradation, and new bone formation at 4 weeks even with the addition of 40 (low) or 200 (high) µg/mL rhBMP-2 (Figure 8.4). In these images, residual MG shows up black, PUR is dark blue or purple, and new bone is red. Some bone grew around the outside of the scaffolds; however, the composites were primarily walled off. We believe the success of this study was limited in part due to low porosity of the LV/MG graft (~20%) and the lack of an osteoconductive scaffold within the LV/S graft. In the currently proposed study, the nHA-LTI prepolymer will be mixed with a fast degrading polyester triol comprised of 60% caprolactone, 30% glycolide, and 10% lactide (900 g/mol) containing an osteoconductive ceramic matrix and a porogen (either bioactive glass particles or sucrose). With the low porosity of the low-expansion system, the porogen phase will act as a pathway for cellular infiltration and prevent the graft from being walled off with limited cell and bone infiltration.

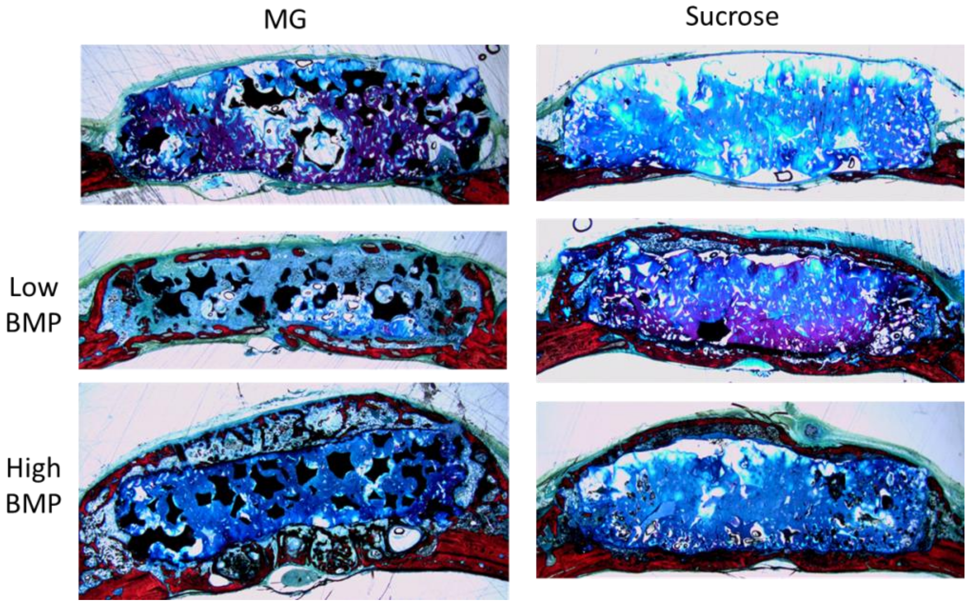

Figure 8.4**.** Low magnification histological analysis of a rat calvarial study testing LV/CM and LV/S composites with 40 µg/mL rhBMP-2 (low) or 200 µg/mL rhBMP-2 (high) grafts in a critical-size rat calvarial defect at 4 weeks. Residual ceramic is black, new bone is red, and residual PUR stains dark blue or purple.

Autografts are commonly used to obtain arthrodesis in spinal fusion procedures, but this is limited by autograph availability and cannot be combined with minimally invasive surgical (MIS) techniques (12). Autograft extenders have been used previously to dilute and conserve autograft while maintaining the osteoconductivity or osteoinductivity of the scaffold. Allogenic demineralized bone matrix (DBM) has osteoinductive properties and has been extensively studied in the spine as an autograft extender (13, 14); however, DBM has difficult handling properties and cannot be delivered with MIS techniques. The newly developed nHA-LTI/PCL technology is a potential candidate for use as a compression-resistant autograft extender. These are injectable, settable grafts with the necessary mechanical properties to resist the mechanical forces from the posterior musculature and can be delivered using MIS techniques while conserving autograft. A recent pilot study was conducted with nHA-LTI/PCL scaffolds containing autograft, Mastergraft, or a mix of the two in a rabbit posterolateral spinal fusion model. There was good contact of the graft with the host bone interface, limited expansion, and new bone formation evident after 8 weeks.

With the aforementioned reproducible, low cost osteoclast co-culture assay (Chapter VI) the applications of this technique and analysis method (3D profilometry) abound. While osteoclastogenesis is driven by stimulated osteoblasts in the developed co-culture assay, there are other conditions where osteoclast differentiation can occur. Currently our group is testing osteoclastogenesis from (1) bacterial supernatant and (2) conditioned media from tumor cell culture.

Previously, infection has been linked to osteoclast formation and bone loss in patients through proinflammatory cytokines released during chronic periodontal disease (15). Another group has shown that bacterial lipopolysaccharide, a component of the cell wall in Gram-negative bacteria, stimulates osteoclast formation from RAW 264.7 cells (16). These findings have implications with excessive bone resorption seen in patients with chronic inflammatory diseases like periodontitis, osteomyelitis, and arthritis (17). Currently our group is planning to study the effects of bacterial supernatant from cultured *Staphylocuccus aureus* bacteria on osteoclast differentiation of RAW 264.7 cells and osteoclast mediated resorption of dentin and synthetic substrates. This research will be conducted on cells cultured on both 2D substrates as well as 3D scaffolds in static culture. 3D *in vitro* systems better mimic the complexity of the host bone environment (porosity, pore size, mechanical properties) and aid in understanding cellular interactions with host tissue (18). Future tests will also be run in a bioreactor to mimic the fluid flow and cell diffusion present in natural bone.

Numerous studies have linked osteoclast formation and activity with tumor burden in patients suffering from bone metastatic cancer. Certain cancers are more likely than others to metastasize to bone, including breast and prostate. A number of signaling molecules have been implicated in osteoclastogenesis, including parathyroid-horome-related peptide (PTHrP) which is released by tumor cells in the bone microenvironment (19). PTHrP and other factors induce osteoclast formation and bone destruction which can significantly decrease quality of life in patients. One current focus of research in our group is testing conditioned media from tumor cells (breast cancer line) on osteoclast formation and resorption of substrates in 2D and 3D systems, both in static culture and in a bioreactor. This study will provide fundamental details regarding osteoclast activity under a variety of conditions, with the aim to replicate the true microenvironment of host tissue as closely as possible.

References

1. Hannink, G., andArts, J.J.C. Bioresorbability, porosity and mechanical strength of bone substitutes: What is optimal for bone regeneration? Injury **42, Supplement 2**, S22, 2011.
2. Calori, G.M., Mazza, E., Colombo, M., andRipamonti, C. The use of bone-graft substitutes in large bone defects: any specific needs? Injury **42 Suppl 2**, S56, 2011.
3. Brown, K.V., Li, B., Guda, T., Perrien, D.S., Guelcher, S.A., andWenke, J.C. Improving bone formation in a rat femur segmental defect by controlling bone morphogenetic protein-2 release. Tissue Eng Part A **17**, 1735, 2011.
4. Boerckel, J.D., Kolambkar, Y.M., Dupont, K.M., Uhrig, B.A., Phelps, E.A., Stevens, H.Y., Garcia, A.J., andGuldberg, R.E. Effects of protein dose and delivery system on BMP-mediated bone regeneration. Biomaterials **32**, 5241, 2011.
5. Hafeman, A.E., Zienkiewicz, K.J., Zachman, A.L., Sung, H.J., Nanney, L.B., Davidson, J.M., andGuelcher, S.A. Characterization of the degradation mechanisms of lysine-derived aliphatic poly(ester urethane) scaffolds. Biomaterials **32**, 419, 2011.
6. Iglhaut, G., Schwarz, F., Grundel, M., Mihatovic, I., Becker, J., andSchliephake, H. Shell technique using a rigid resorbable barrier system for localized alveolar ridge augmentation. Clin Oral Implants Res **25**, e149, 2014.
7. Jovanovic, S.A., Hunt, D.R., Bernard, G.W., Spiekermann, H., Wozney, J.M., andWikesjö, U.M. Bone reconstruction following implantation of rhBMP-2 and guided bone regeneration in canine alveolar ridge defects. Clinical oral implants research **18**, 224, 2007.
8. Von Arx, T., Schenk, R.K., Buser, D., Cochran, D.L., andHermann, J.S. Lateral ridge augmentation using different bone fillers and barrier membrane application. Clinical Oral Implants Research **12**, 260, 2001.
9. Araujo, M., Sonohara, M., Hayacibara, R., Cardaropoli, G., andLindhe, J. Lateral ridge augmentation by the use of grafts comprised of autologous bone or a biomaterial. An experiment in the dog. Journal of clinical periodontology **29**, 1122, 2002.
10. Wei, G., andMa, P.X. Structure and properties of nano-hydroxyapatite/polymer composite scaffolds for bone tissue engineering. Biomaterials **25**, 4749, 2004.
11. Wang, H., Li, Y., Zuo, Y., Li, J., Ma, S., andCheng, L. Biocompatibility and osteogenesis of biomimetic nano-hydroxyapatite/polyamide composite scaffolds for bone tissue engineering. Biomaterials **28**, 3338, 2007.
12. Skovrlj, B., Gilligan, J., Cutler, H.S., andQureshi, S.A. Minimally invasive procedures on the lumbar spine. World Journal of Clinical Cases : WJCC **3**, 1, 2015.
13. Cammisa Jr, F.P., Lowery, G., Garfin, S.R., Geisler, F.H., Klara, P.M., McGuire, R.A., Sassard, W.R., Stubbs, H., andBlock, J.E. Two-year fusion rate equivalency between Grafton® DBM gel and autograft in posterolateral spine fusion: a prospective controlled trial employing a side-by-side Comparison in the Same Patient. Spine **29**, 660, 2004.
14. Morone, M.A., andBoden, S.D. Experimental posterolateral lumbar spinal fusion with a demineralized bone matrix gel. Spine **23**, 159, 1998.
15. Ukai, T., Yumoto, H., Gibson, F.C., andGenco, C.A. Macrophage-elicited osteoclastogenesis in response to bacterial stimulation requires Toll-like receptor 2-dependent tumor necrosis factor-alpha production. Infection and immunity **76**, 812, 2008.
16. Islam, S., Hassan, F., Tumurkhuu, G., Dagvadorj, J., Koide, N., Naiki, Y., Mori, I., Yoshida, T., andYokochi, T. Bacterial lipopolysaccharide induces osteoclast formation in RAW 264.7 macrophage cells. Biochemical and Biophysical Research Communications **360**, 346, 2007.

17. Nair, S.P., Meghji, S., Wilson, M., Reddi, K., White, P., andHenderson, B. Bacterially induced bone destruction: mechanisms and misconceptions. Infection and immunity **64**, 2371, 1996.
18. Guo, R., Lu, S., Page, J.M., Merkel, A.R., Basu, S., Sterling, J.A., andGuelcher, S.A. Fabrication of 3D Scaffolds with Precisely Controlled Substrate Modulus and Pore Size by Templated-Fused Deposition Modeling to Direct Osteogenic Differentiation. Advanced Healthcare Materials **4**, 1826, 2015.
19. Mundy, G.R. Metastasis: Metastasis to bone: causes, consequences and therapeutic opportunities. Nat Rev Cancer **2**, 584, 2002.

APPENDIX A

EXPERIMENTAL PROTOCOLS

This method for washing polyol is adapted from the method used by Ricerca.

Before starting: Read and understand the MSDS of the reagents listed below
- Personal Protective and Safety Equipment required:
    - Disposable nitrile gloves
    - Heavy duty gloves
    - Hot gloves
    - Hood
    - Appropriate attire according to the Chemical Hygiene Plan (shoes, labcoat, goggles, etc.)

Equipment/Materials	**Reagents**
(2) 600mL beaker Stir plate/stir bar Syringes 100mL graduated cylinder Parafilm	N-heptane Ethyl acetate Dichloromethane (DCM) Base bath Acetone Celite 521- Acros Organics

WASH PROCEDURE

1. After making polyol, pour the polyol into a clean, dry 600mL beaker and allow polyol to cool to room temperature
2. Place a stir bar into the beaker and set on stir plate
3. Set the stir plate to stir at a media speed.
4. If the polyol is too viscous for stirring, introduce a few mL of DCM into the beaker. Continue until the polyol stirs easily.
5. Add 75mL of n-heptane to the beaker and cover with parafilm. Stir for 60min
6. Turn off the stir plate and allow the polyol and solvent to sit, covered, for 10min
7. Decant heptane
8. Repeat steps 4-7 3 more times, for a total of 4 n-heptane washes
9. Add 250mL of ethyl acetate to the polyol and turn on the stir plate. Cover the polyol and allow to stir for ≥16hrs
10. Measure out 16g of the celite and place into a Buchner funnel fitted with filter paper. Compress the celite with a ceramic pestle to create an even, thin layer of celite

11. Setup the filter flask with the Buchner funnel and vacuum pump
12. While the vacuum pump is on, pour the polyol/ethyl acetate mixture into the Buchner funnel, in batches, and allow it to filter through the celite
13. Once all the polyol has been filtered through the celite, wash the celite with an additional 50mL of ethyl acetate
14. Pour all of the polyol/ethyl acetate into a clean, dry 600mL beaker. Place in the vacuum oven for 48hrs at 80°C
15. Once dry, pour the polyol into an amber vial and degass with argon

Clean-up:

1. Collect all sharps and dispose in the sharps waste container (red box)
2. Collect all liquid waste and dispose in the appropriate liquid waste container (halogenated)
3. Collect all solid waste and dispose in the solid waste container
4. Clean glassware:
    a. Wash with soap and water
    b. If it is necessary, rinse with acetone and introduce into the base bath for 24 hrs. Rinse with a lot of cold running water after removing from the base bath.
    c. Rinse with acetone and dry in the oven

Equipment/Materials
ImageJ: Free software available online at http://rsbweb.nih.gov/ij/.

PROCEDURE

1. Open ImageJ software and open the SEM image (tiff) that you want to analyze by clicking *File->Open* finding desired image.
2. To Scale the Image: click on the straight line drawing tool in the drawing menu

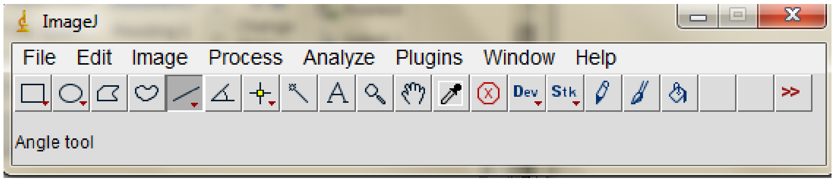

Draw a straight line over the scale bar in the image

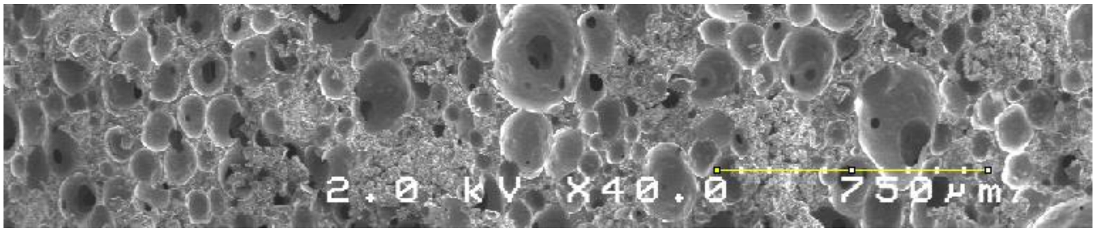

In the menu tabs, click *Analyze -> Set Scale.*

The 'distance in pixels' is the length of the line you drew. Set the 'known distance' to the length of your scale bar (in this case 750) and change 'unit of length' to the desired unit (in this case um). It should look like this:

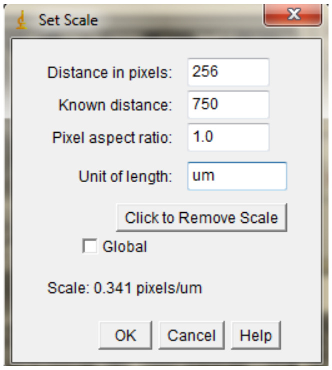
Set Scale

Distance in pixels: 256
Known distance: 750
Pixel aspect ratio: 1.0
Unit of length: um
☐ Global
Scale: 0.341 pixels/um

Click ‘OK’ and the scale will be saved. You can write down the distance and pixels for future images with the same scale bar.

3. To find image area: click *Analyze* -> *Tools* -> *ROI manager*. Check the ‘Show All’ box at the bottom and uncheck the ‘Edit Mode’ Box

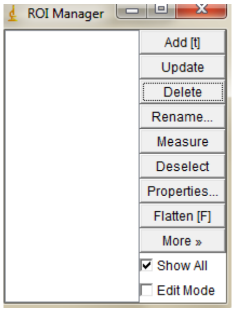

☑ Show All
☐ Edit Mode

Click on the rectangle drawing icon on the drawing toolbox

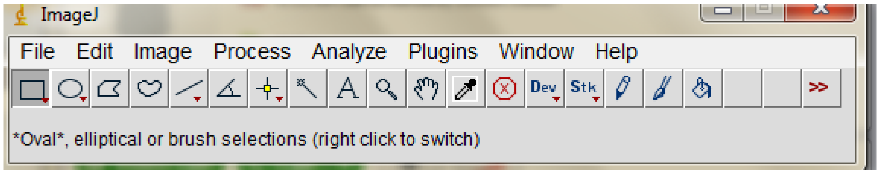

Oval, elliptical or brush selections (right click to switch)

Select the image and draw a rectangle that encompasses the entire region of interest. *Note: if the region of interest does not take up the entire image area, you can use the freehand drawing tool (to the left of the line tool) to select area.*

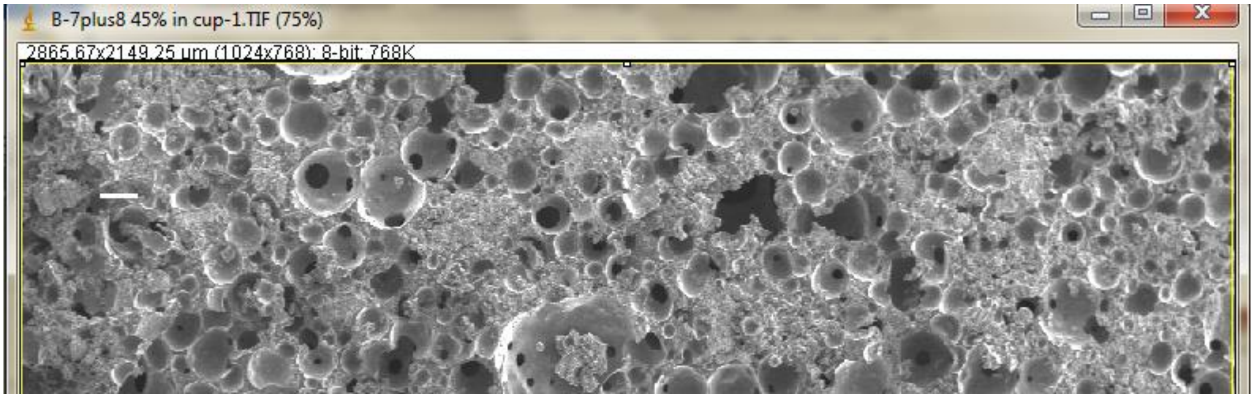

2865.67x2149.25 um (1024x768); 8-bit; 768K

This isn’t the entire image, but it gives an idea of what the rectangle should look like. To add this to the ROI manager, click the letter ‘t’ on your keyboard or the ‘Add [t]’ button on the right side of the ROI manager. It should then look like this:

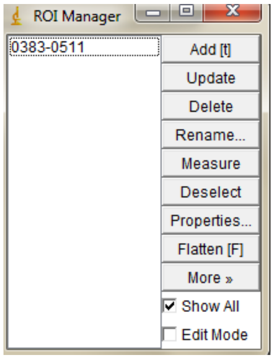

4. To select pores: click on the draw freehand tool (to the left of the straight line drawing tool). Select the image and draw around a pore of interest. If the pores are circular, you can use the oval drawing tool. Hit the letter ‘t’ on your keyboard to add each selection to the ROI manager. Each time you draw a new pore, the previous selection will turn teal. The current pore will show up yellow. *Note: if the software won’t let you draw any more shapes, check and uncheck the ‘Edit mode’ box on the ROI manager and continue drawing.*
5. To measure all areas: after all pores have been selected, click the ‘Measure’ tab on the right side of the ROI manager. This will give you a table of all the areas you selected.

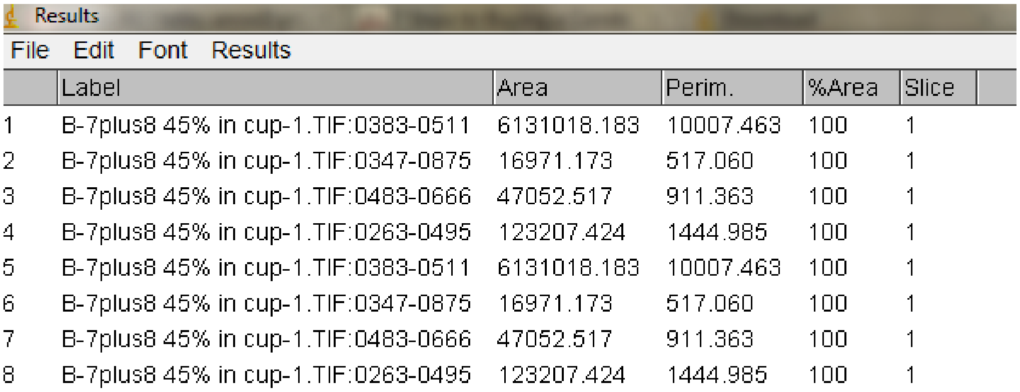

	Label	Area	Perim.	%Area	Slice
1	B-7plus8 45% in cup-1.TIF:0383-0511	6131018.183	10007.463	100	1
2	B-7plus8 45% in cup-1.TIF:0347-0875	16971.173	517.060	100	1
3	B-7plus8 45% in cup-1.TIF:0483-0666	47052.517	911.363	100	1
4	B-7plus8 45% in cup-1.TIF:0263-0495	123207.424	1444.985	100	1
5	B-7plus8 45% in cup-1.TIF:0383-0511	6131018.183	10007.463	100	1
6	B-7plus8 45% in cup-1.TIF:0347-0875	16971.173	517.060	100	1
7	B-7plus8 45% in cup-1.TIF:0483-0666	47052.517	911.363	100	1
8	B-7plus8 45% in cup-1.TIF:0263-0495	123207.424	1444.985	100	1

You can copy and paste this into an Excel document. You will most likely be using the area values (which will be in whatever units you scaled with). You can obtain porosity by summing the areas of each individual pore relative to the area of the region of interest (rectangle encompassing the whole area).

Equipment/Materials
Metamorph Software Adobe Photoshop Software

IMAGING SLIDES

1. Open Infinity Analyze and turn on the microscope
2. Check to make sure the microscope lens is the 2x lens (silver)
3. Place the slide of interest in the slide holder on the microscope.
4. Use the preset settings of ‘Anne BVF’
5. Adjust the coarse and fine focus to get a good image. Adjust the light as necessary
6. Use the ‘capture’ button to take the first image at the very edge of the defect
7. Continue taking overlapping images so that you can create a full replica of the defect site (and surrounding tissue)
8. Save all images as **JPEG** files in ‘Desktop -> Anne -> Lillian -> Sheep Histomorphometry -> ‘Sample ID’ in numerical order

COMBINING IMAGES

1. Open Adobe Photoshop and click ‘Create’
2. Go to File -> New -> Blank File
3. Fill in the opening screen with the following information. Use the sample ID in the ‘name’ section

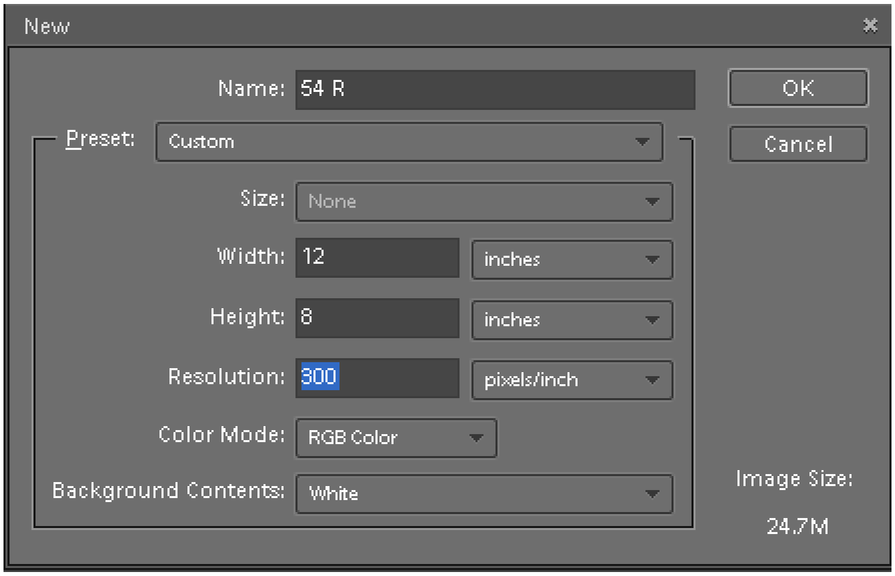

Name: 54 R
Preset: Custom
Size: None
Width: 12 inches
Height: 8 inches
Resolution: 300 pixels/inch
Color Mode: RGB Color
Background Contents: White
Image Size: 24.7M

4. Go to File -> Open and select all of the images you took in Step 1. These will show up in the bin at the bottom of the screen.
5. Double click on Image 1 to select it.
6. Select the image using Ctrl + A and copy with Ctrl + C
7. Return to blank file and paste the image. Decrease the size of the image to W: 50% and H: 50%. Click the green check to select this size
8. Repeat (5-7) for image 2. Once resized right click image and select ‘bring to front’.
9. Line up image 2 to overlap with image 1. (as shown below)

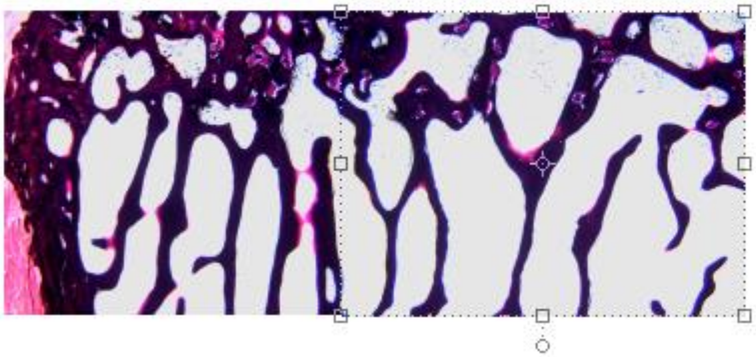

10. Repeat for all 12 images (4 across defect, 3 down)

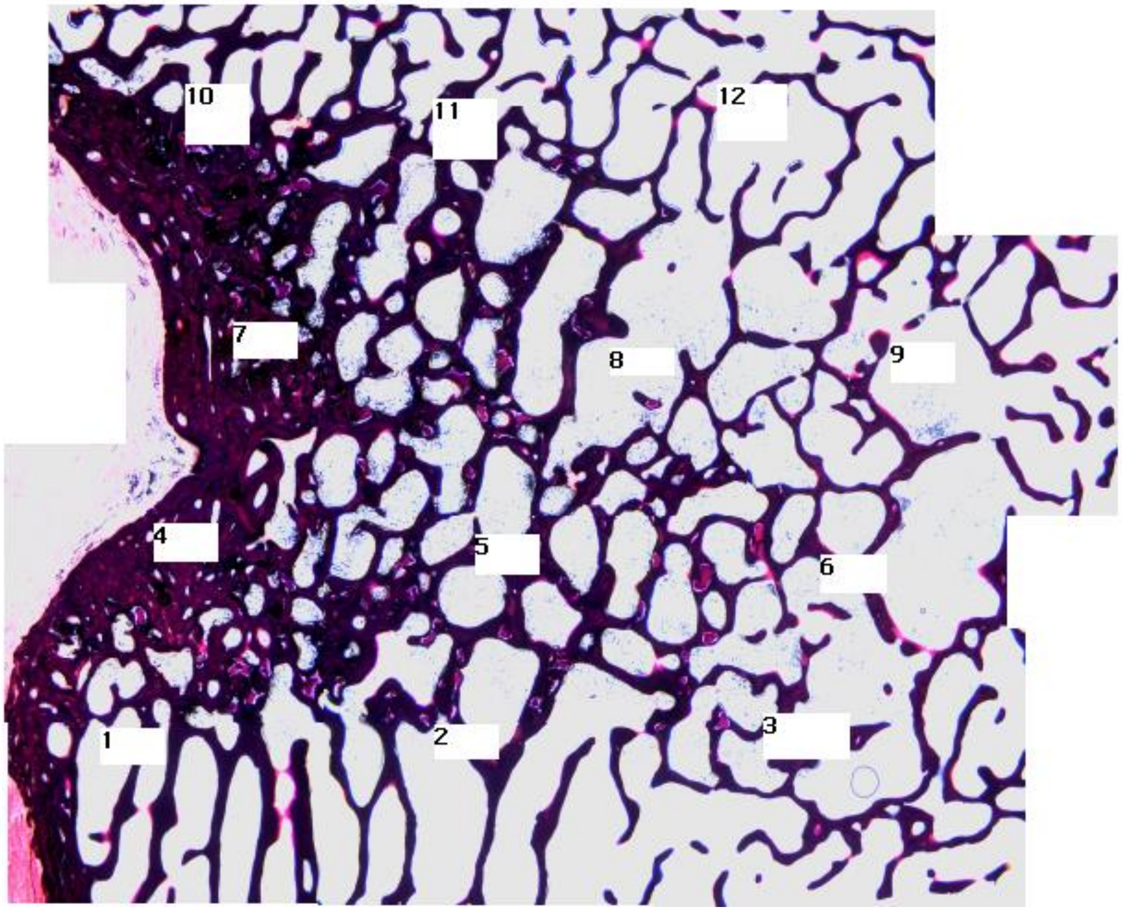

11. As a final step, open image ‘2x scale’ and copy, paste, and resize this into the main image. This will allow us to scale the image later.

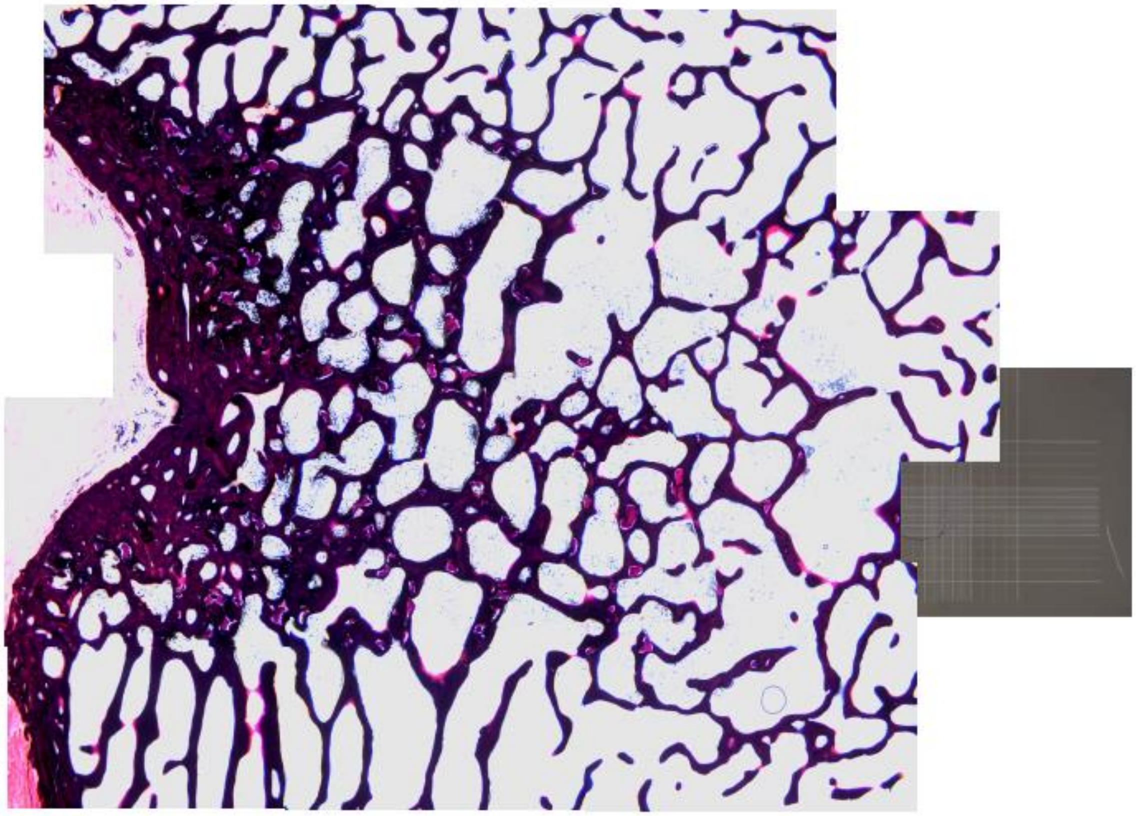

12. Save image with File -> Save As

    Save as a photoshop format 1st, so that we can go back and edit if necessary.

    Save as a JPEG file with the name ‘Sample Id compilation’

THRESHOLDING ALLOGRAFT

Step 1: Open slide of interest in Photoshop

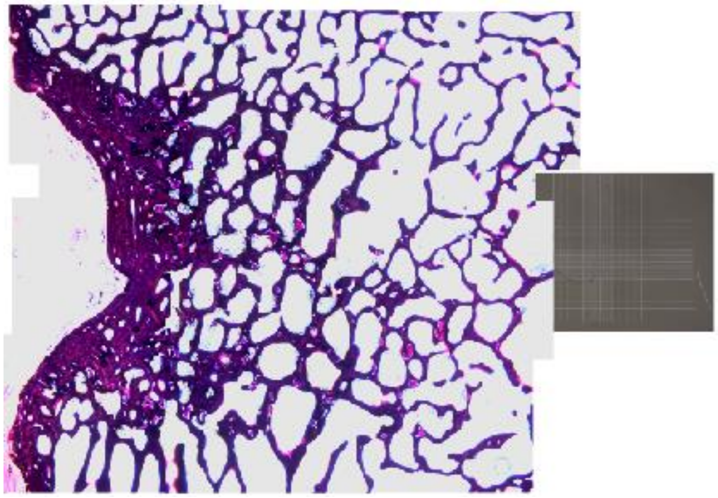

1. Go to File -> Save as, Save as a new file so that you still have the original

2. Go to View -> Zoom In, until you can easily see the defect.

3. Go to Select -> All Layers.

4. Go to Layer -> Merge Layers

5. Select the paint brush icon (green circle)

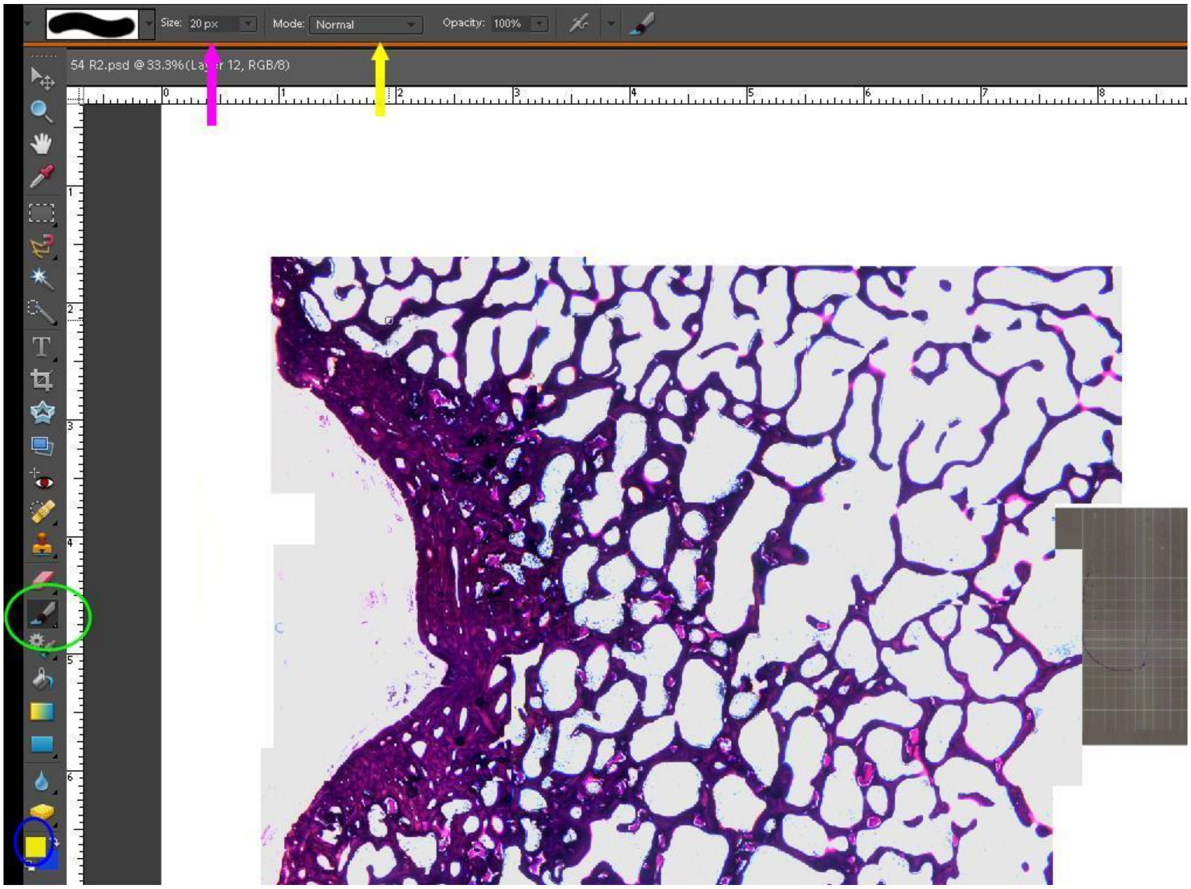

Size: 20 px

Mode: Normal

Opacity: 100%

54 R2.psd @ 33.3%(Layer 12, RGB/8)

a. Set the size (pink arrow) to no more than 20 pixels (or smaller, if needed, so that the allograft can be easily selected)
b. Make the sure the mode (yellow arrow) is set to normal
c. Select the color (blue circle) to one that is easily differentiated from the other colors in the image. This will make thresholding easier. I selected a bright yellow.

6. Color over the regions that are allograft. You can zoom in further if necessary. It is better to select as allograft if you are unsure. Here is a subsection of an image as an example. The allograft will most likely be a slightly lighter color and the edges will be more visible. If you need to, you can use the slides (on a higher magnification) to get a better look at the sample

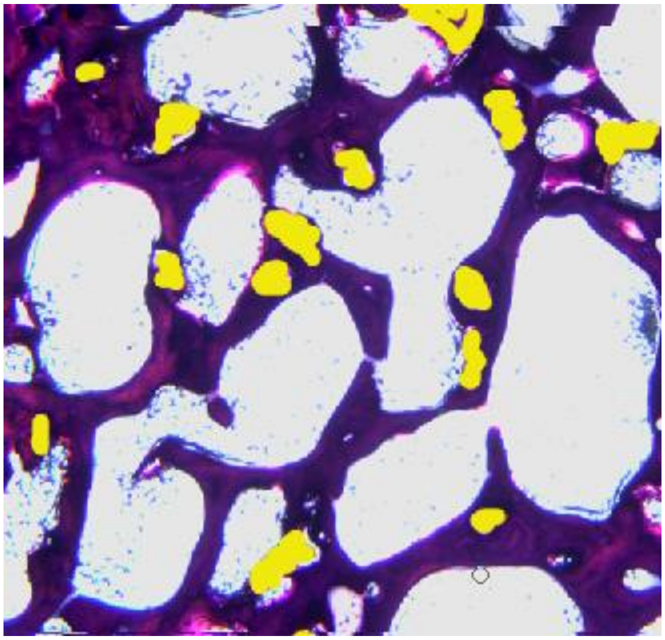

7. Once you have selected all of the allograft and saved the image, you can use the normal thresholding technique to determine the new bone/old bone in the image by thresholding for the yellow (allograft) or the pink/purple (new bone).

QUANTITATIVE ANALYSIS

Histomorphometry Protocol for Quantiative Analysis of femoral plug sections – AT

Step 1: Open Metamorph Software and the image of interest

1. Set zoom to 45% and calibrate image
    a. Measure -> Calibrate Distances

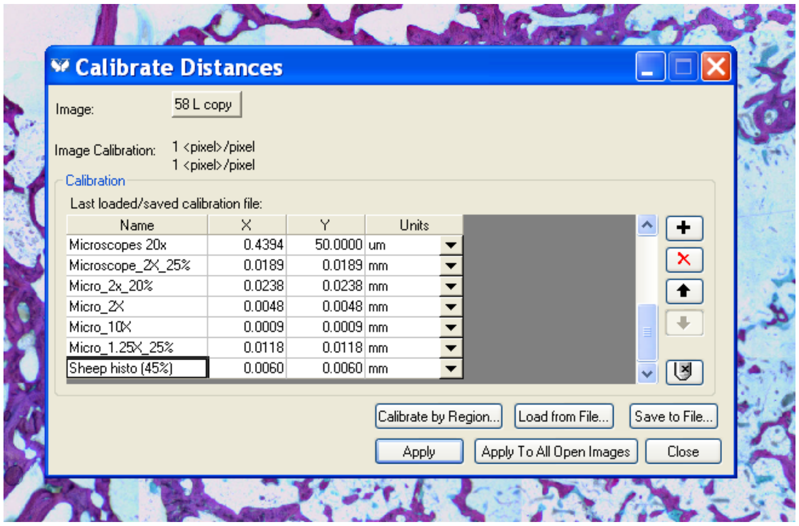

Image: 58 L copy

Image Calibration: 1 <pixel>/pixel
1 <pixel>/pixel

Calibration

Last loaded/saved calibration file:

Name	X	Y	Units
Microscopes 20x	0.4394	50.0000	um
Microscope_2X_25%	0.0189	0.0189	mm
Micro_2x_20%	0.0238	0.0238	mm
Micro_2X	0.0048	0.0048	mm
Micro_10X	0.0009	0.0009	mm
Micro_1.25X_25%	0.0118	0.0118	mm
Sheep histo (45%)	0.0060	0.0060	mm

    b. Click on sheep histo (45%) and hit apply. This calibrates the image.

2. Draw a line 3mm from the cortex. Draw a rectangular box 6mm wide by 10.66mm tall. This box will be at the edge of the line

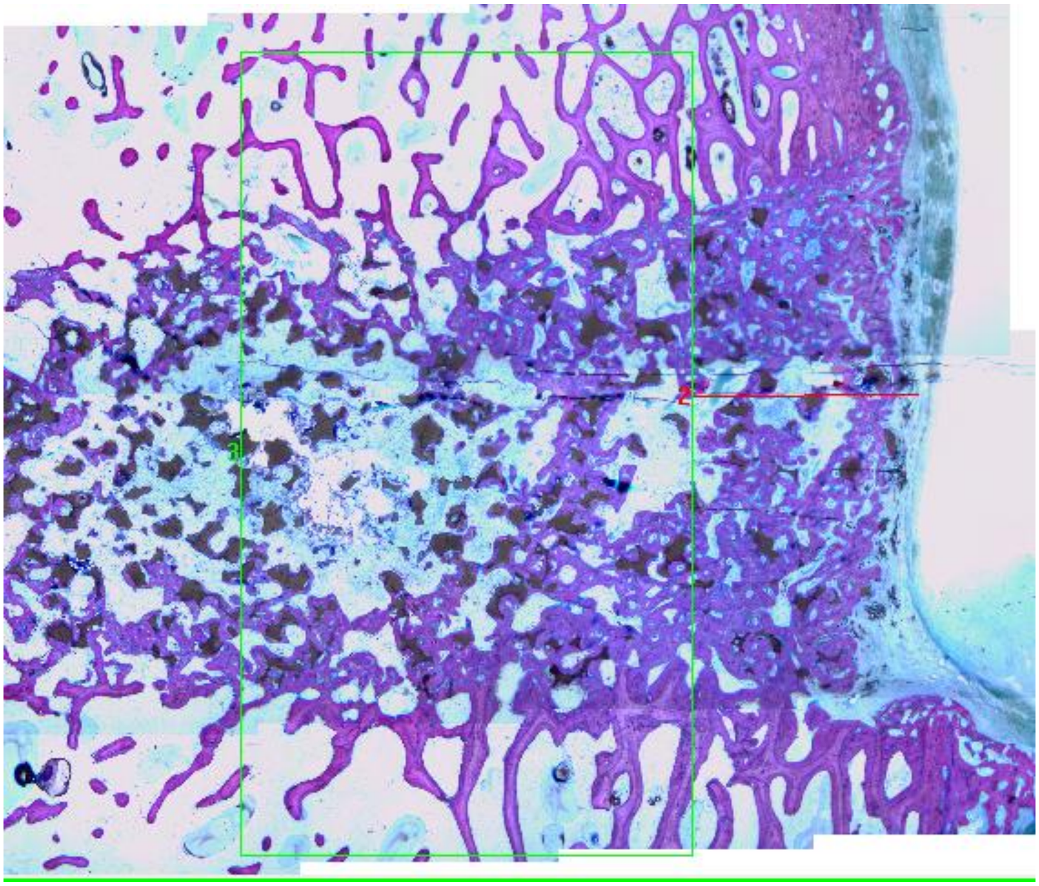

3. Within the main rectangle, draw 8 smaller rectangles measuring 6mm wide by 1.33 mm. These represent the concentric regions of interest

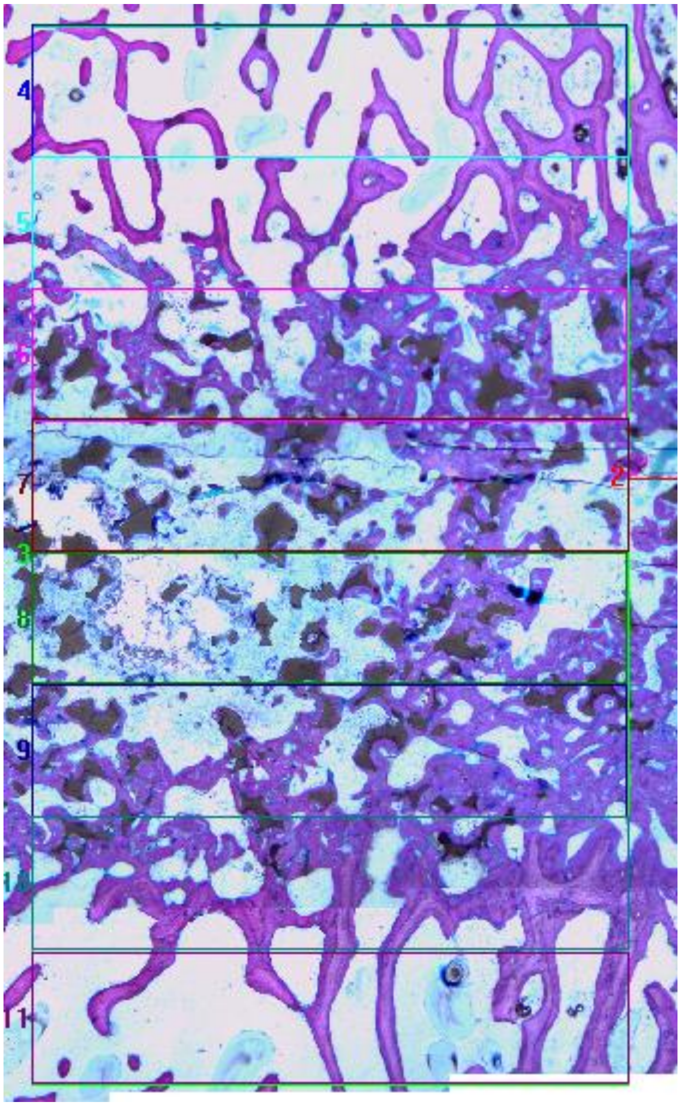

4. Measure -> Set Color Threshold to analyze regions of interest for MG, PUR, and new bone. Load Range ‘sheep histo_bone’ to start. Change hue, saturation, and intensity to select only bone (purple). The selected thresholds will show up yellow

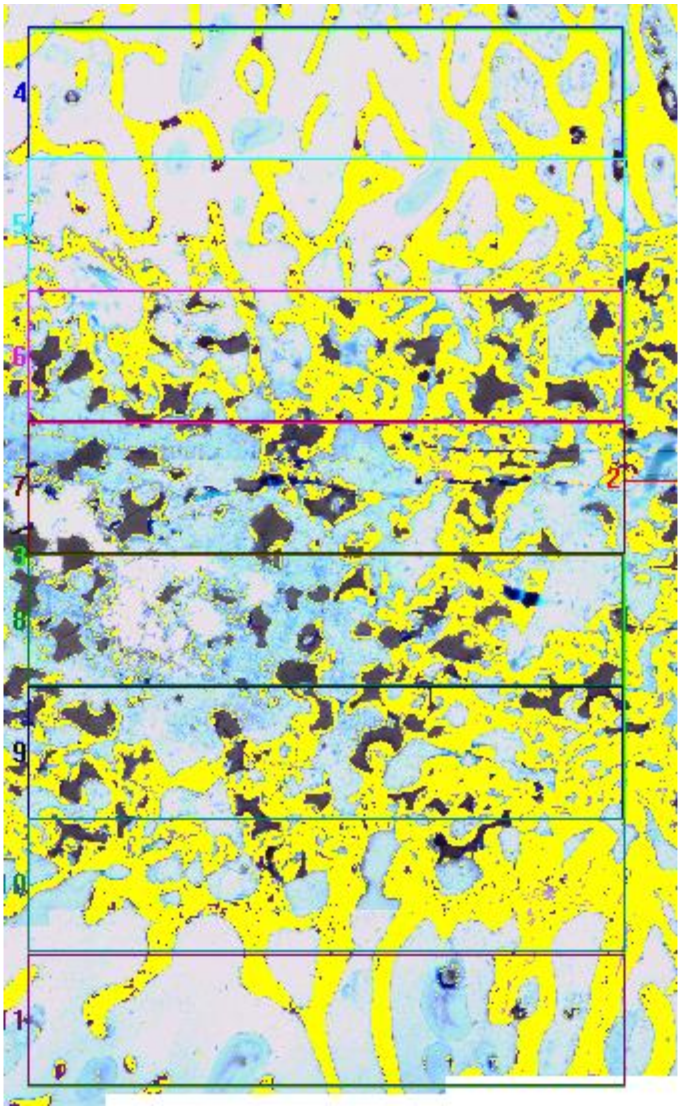

5. Go to Measure -> Region Measurements. Click ‘Open Log’, opens up a new Excel doc. Once open, click ‘Log Data’ to send thresholded data to Excel. Copy and paste this data into another Excel doc to collect it all in one place
6. Use the thresholds Sheep Histo MG and Sheep histo PUR to do the same analysis for those.

Adapted from Margarita Prieto-Ballangee dissertation and papers

Equipment/Materials
MC3T3 cells RAW 264.7 cells 24 well plates Osteogenic differentiation media (Complete α-MEM plus 10nM dexamethasone, 50µM ascorbic acid, 0.1mM β-glycerophosphate) (OB Diff Media) 1,25-Dihydroxyvitamin D (Vitamin D3) Matrices of interest (dentin chips, HA discs, TCP discs, BG discs)

MATERIAL PREPARATION

1. Sonicate matrices of interest for 7.5min in DI H_2O (x3)
2. Sterilize in 70% Ethanol for 5min (x2)
3. Wash in sterile H_2O for 5min (2x)
4. Wash in OB Diff media for 5min
5. Condition overnight in OB Diff Media

CELL SEEDING

6. Aspirate off media and allow matrices of interest to dry in hood for 30min
7. Plate MC3T3 cells on matrices of interest at 1×10^4 cells/well in 100µL OB Diff Media. Place well plates in the incubator for 30 min to allow cells to attach.
8. Add 900 µ OB Diff media with VD3 (10nM) slowly to avoid disrupting cells (total 1mL media per well).
9. After 48 hrs, aspirate media and plate RAW cells at 1×10^4 cells/well in 100µL OB Diff Media. Place well plates in the incubator for 30 min to allow cells to attach.
10. Add 900 µ OB Diff media with VD3 (10nM) slowly to avoid disrupting cells (total 1mL media per well).
11. After 48 hrs, move the matrices of interest to a new well plate.
12. Every 1-2 days remove half the media in the well and replace with fresh differentiation media plus 10nM VD3.

13. By 14 days, you should see larger, multinucleated cells.

14. If desired, test for TRAP and counterstain with a nuclear dye